UNIVERSITY OF CALIFORNIA
Los Angeles

Insert Tidal Here:
A Planetary Evolution Cookbook

A dissertation submitted in partial satisfaction
of the requirements for the degree
Doctor of Philosophy in Geophysics & Space Physics

by

Matthew Edward Walker

2017

ABSTRACT OF THE DISSERTATION

Insert Tidal Here:
A Planetary Evolution Cookbook

by

Matthew Edward Walker
Doctor of Philosophy in Geophysics & Space Physics
University of California, Los Angeles, 2017
Professor Jonathan Lloyd Mitchell, Chair

The observed activity at the surfaces of the Galilean satellites mask subsurface internal dynamics. Tides generated from their primary, the massive planet Jupiter, deform these moons and can generate significant heat. This heat must then escape to space. The heat moving through a satellite has the potential to modify the interior structure, melting regions and causing internal interface boundary migration. We track how tidally generated heat will flow out of Io and Europa, and how this heat will modify the planetary structures. To do this we determine specific forms for the k Love numbers which depend on internal structure and temperature profiles. The Love numbers are used as a linear factor in tidal heating models. Because the Love numbers are very frequency dependent, it is important to consider every frequency term in a tide, as some may be much more significant than others. While some tidal heating models consider the orbital frequency only, we present the full tidal heating spectrum and isolate which terms are significant in which cases. In addition to finding the simple tidal heat forms for use with Io and Europa, we demonstrate with extreme examples, the tidal heating scenarios at Mercury and Venus. In these cases we find systems where the tidal heat delivery comes at frequencies related to sums and differences of mean motion and spin rate. Finally we use the Love numbers for Io and Europa we generated, in the tidal heating models as a term in thermal evolution models. We balance a tidal heat input into the bodies with heat convected upward into an elastic lid. The lid then conducts the once tidal heat into space. We probe the planetary structural and temperature space which leads to

equilibrium conditions, where the tidal heat input is balanced by heat escape. For Io, we find no stable equilibrium scenarios for any structure we consider, and the body ultimately melts. This results because the dissipating volume is assumed to extend to the core. This generates much more heat than is able to conduct out through the lid and runaway melting occurs. Reducing the volume of the region, by adding a core or a subsurface fluid silicate layer, may reduce the volume enough for stable conditions to be found. In Europa, we do find stable equilibrium conditions at ice shells of roughly 50 km. For shells thicker than this, the tidal heating is too strong due to increased volume, and so the shell melts some in response until stable equilibrium is achieved. The Europa Clipper mission is slated to measure both shell thickness as well as the k Love number. With the relationships we draw between structural and orbital parameters, these measurements in the system can help constrain our models so that we can use Europa's current state as a probe for its thermal history and an indicator of its thermal future.

The dissertation of Matthew Edward Walker is approved.

Jean-Luc Margot

Smadar Naoz

David Jewett

Bruce G. Bills

Jonathan Lloyd Mitchell, Committee Chair

University of California, Los Angeles

2017

Table of Contents

List of Figures

Vita

2010	B.A., Physics/B.A., Mathematics (Double Major) Magna Cum Laude University of Southern Maine, Portland, Maine.
2014	M.S., Geophysics & Space Physics UCLA, Los Angeles, California.
2012-2016	Teaching Assistant, Earth, Planetary, and Space Sciences, UCLA. Multiple sections of Astrobiology, Dinosaurs, Solar System and Planets, Natural Hazards

Publications

Near-Infrared Spectroscopy of Primitive Asteroid Families
Icarus, Volume 213, Issue 2, p. 538-546 (June 2011)

Tidal Disruption of Phobos as the Cause of Surface Fractures
Journal of Geophysical Research , Volume 121, Issue 6, p. 1054-1065 (June 2016)

CHAPTER 1

Introduction

The Galilean Satellites are currently an ideal place to model solar system dynamics, because of its potential for measurement and observation. Adjacent satellites are found in pairs of mean motion resonances, which keep the eccentricities finite. These non-zero eccentricities are then responsible for the tidal deformation which keeps these bodies thermally active. Of these bodies, in particular Europa has the potential for habitability, and this makes this satellite of Jupiter an attractive target for future space exploration. Voyager images of a shattered Europan surface were the first to indicate a subsurface ocean [27]. Some time later, improved imaging (Fig. 1.1) and Galileo magnetometer data were used to support the hypothesis of a fluid layer under Europa's ice [15]. While these missions and analysis provided clues about Europa's structure and history, much is still unknown about how Europa's surface deforms and, more importantly, what lies beneath its ice.

The Europan ocean is an important target for habitability studies because life, as we know it, depends on water. In addition to water, the chemistry of the environment as well as available energy sources must be characterized in order to determine the plausibility of Europan life forms. To this aim a new mission, the Europa Clipper, is in the investigation process at NASA for Europa science. Objectives of this mission follow three tracks: Geology, Composition, and Ice Shell & Ocean. For Geologic science, detailed imaging will provide information concerning the activity and formation of the surface. Spectrometers on board Clipper can help to constrain the composition and chemistry of the surface and Europan atmosphere. Finally, radio and radar equipment will help characterize the ice shell and ocean, as well as their interaction. This interaction of ocean and ice is likely a critical component of an environment suitable for life [6], as the delivery of surface chemistry into

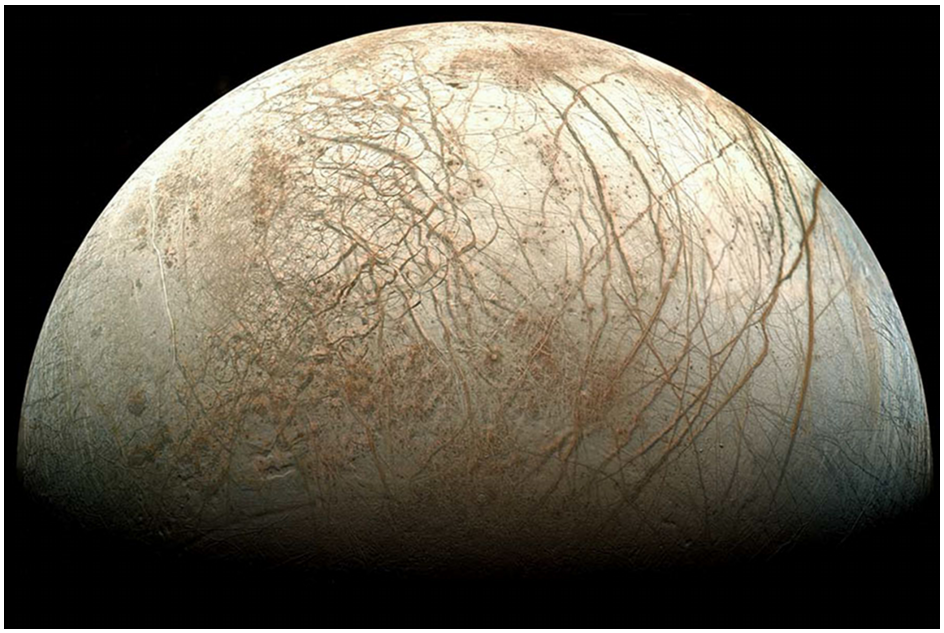

Figure 1.1: A Galileo image of Europa in global context, highlighting the abundance and diversity of surface features on Europa's icy shell. The surface activity masks internal dynamics and energy gradients which life could plausibly exploit.

the oceans below may be a source of organics.

I expect that tracking the heat flow though Europa, or any body for that matter, is critical for deeper insights into the system stability and evolution. Identifying the stable processes which move energy in the body, we can then hypothesize how any potential life form might exploit these energy gradients. On Earth, for example, it is not just a fortunate mix of water and carbon at an ideal distance from our star which supports life. In addition, the heat, naturally escaping from our planet, provides stable cycles which life has tapped. Heat from the core initiates mantle convection which drives the plate tectonics observed at the surface. These surface motions facilitate the carbon cycle's release and recycling of carbon (which life on this planet happens to be made of) in our atmosphere and lithosphere, stabilizing the environment. From core to atmosphere, fortuitous interactions of physical processes come together to make our planet habitable. Therefore, in considering the habitability of other worlds it is essential that we understand how these links operate in various environments.

In this project we aim to track the thermal energy and heat flow for the bodies in the

Galilean satellite system. In Chapter 1, we will generate functional forms for measurable parameters that link structure and deformation. The Love numbers tell us the radial density and rigidity distribution in a body, and give us a representation of how a body will deform and store (or dissipate) energy in response to an external forcing. Our Love number model is capable of coupling both viscoelastic and fluid layers, letting the user generate values for any multi-layered body with radially piece-wise constant material properties. In coupling fluid and elastic equations of motion we stumbled onto a slight discrepancy in the l Love number if a body is treated with explicit fluid equations of motion, rather than determined through the conventional "fluid limit" taken for elastic bodies. This is a result of classic descriptions neglecting the bulk relaxation of stresses in incompressible bodies. Additionally, we find a new relationship between the Love numbers linking the l and k values, in analogy to the tilt factor. Finally, we demonstrate a new superposition technique to analytically and intuitively construct Love numbers for complicated bodies. For this we use a two layer representation of Io, and a four layer representation for Europa.

Chapter 2 discusses tidal heating in great detail. We use a Fourier representation of the tide, and determine each frequency's specific contribution to the frictional heating of a body. In contrast to classic descriptions, which look at the orbital frequency only, we find a rich spectrum of tidal inputs which can deliver considerably more heat than the orbital tide alone. This is particularly the case for bodies with high obliquity or those that have rotation rates which are not synchronized to the orbit's mean motion. While for our Io and Europa cases, the classic tidal heating description is sufficient, we present dramatic cases where our model diverges. On Venus we see that the high obliquity produces terms in the tide at high frequency which can deliver around one thousand times more heat than the typical classic model would. Then on Mercury, we see how a spin orbit resonance causes the complete elimination of the most significant eccentricity tidal term. Almost ironically, on the planet in our Solar System with the largest eccentricity, the majority of the planet's tidal heat is generated from eccentricity independent terms.

Finally, in Chapter 3 we look at the heat balance in Io and Europa. We balance the tidal heating inputs to the bodies with the heat convected through and conducted out of

the bodies into space. As input to tidal heating we use the Love numbers generated in Chapter 1. In Io we find that there are equilibrium scenarios, at current orbital parameters, but that these conditions are unstable and would lead to a runaway interior heating and melt processes. Future work would need to consider a more detailed Io structure model to incorporate a high density elastic core, or even fluid melt regions within Io's silicate mantle. With the Europa heat balance, we find that thick ice shells generate much more heat than convection can carry away, and this heats and thins the ice shell. Once the shell thins to roughly 50 km we find a stable parameter space of thermal equlibrium, at current orbital conditions.

CHAPTER 2

Love Numbers

Introduction

Tidal deformation of elastic planetary bodies can be described by three dimensionless parameters. Two of them (h and k) were introduced by A.E.H. Love [16] and the other (l) by T. Shida [26]. When a planetary body deforms, in the presence of some forcing potential, k describes the perturbation to the potential which results from the mass deformation. h and l describe the radial and lateral displacements which result. These parameters are measurable using gravity and radar data from space based missions or by measuring tilt or strains terrestrially. Similar to mean moment of inertia, a planet's Love numbers depend on the internal structure of its body, in particular the radial density and rigidity structure. For infinitely rigid bodies, all three Love/Shida numbers are zero valued while for finite rigidity the elastic Love numbers become real and positive [1]. Ignoring mass inversions, these numbers all have theoretical maxima at the "fluid limit", which describes the scenario where the body behaves more like a fluid than elastic.

Specifically, we have found that an elastic body at the "fluid limit" predicts an l Love number which disagrees with that number predicted using fluid equations of motion, though h and k remain consistent. This occurs because standard treatments neglect the relaxation of bulk stresses in the body. We do not attempt to describe an appropriate treatment for dissipation of bulk stresses, only note the difference and present the true fluid Shida number. In considering fluid equations of motion, we have also found a theoretically observable parameter, directly analogous to the "tilt factor" [1], which relates l and k and can help constrain planetary interior structure models.

Our primary interest which drove this research was a desire to determine a how a body's Love numbers vary when specific structural parameters within the body are allowed to change as a planet structurally evolves over time. As might be expected, the analytic functional forms for Love numbers become increasingly complicated as more detailed structure models are considered. As a major contribution to this chapter, we present a recursive bookkeeping method for analytic generation of Love numbers for any body of interest. We will demonstrate the technique on increasingly complicated structures; first a two layer Io, and second a four layer Europa (which includes coupled fluid and elastic layers).

The remainder of this document is divided into sections. In Sec. 2.1 we define the Love numbers mathematically and qualitatively. In Sec. 2.2 we describe the equations of motion which describe deformation in both elastic and fluid bodies. The most general class of Love number models can determine the complex viscoelastic Love numbers for many layered complicated structures, exploiting the propagator matrix method [23]. These models tend to diverge when fluid limits are considered, and the rigidity of a layer vanishes. As an upgrade, developments have been made which hint at the appropriate boundary conditions to couple legitimate fluid layers to elastic layers [11]. We approach the problem using the explicit fluid equations of motion, to derive why these boundary conditions are valid. An important point here is recognizing the difference in a fluid's behavior, in the cases where it is free to flow versus cases where it is restricted from flow (for example a surface shell over an ocean). Using true fluid equations of motion we compute Love numbers in homogeneous bodies in Sec. 2.3 and show why the fluid Shida number, l, is slightly different from the classic result reported in the literature [12] [17]. In Sec. 2.4 we derive the classic relationships between the Love numbers (i.e. the "tilt factor" and "gravimetric factor") as well as new relationship which includes the l. We then present a new technique to calculate Love numbers in Sec. 2.5. This method exploits superposition of simple structures, to analytically build more and more complicated models for Io and Europa. Our results are analytically equivalent to the methods described by conventional techniques [23] [11], however our arrangement of factors isolates particular terms and factors to allow us to utilize the functions more intuitively. Finally, we close with a summary of our results and discussion.

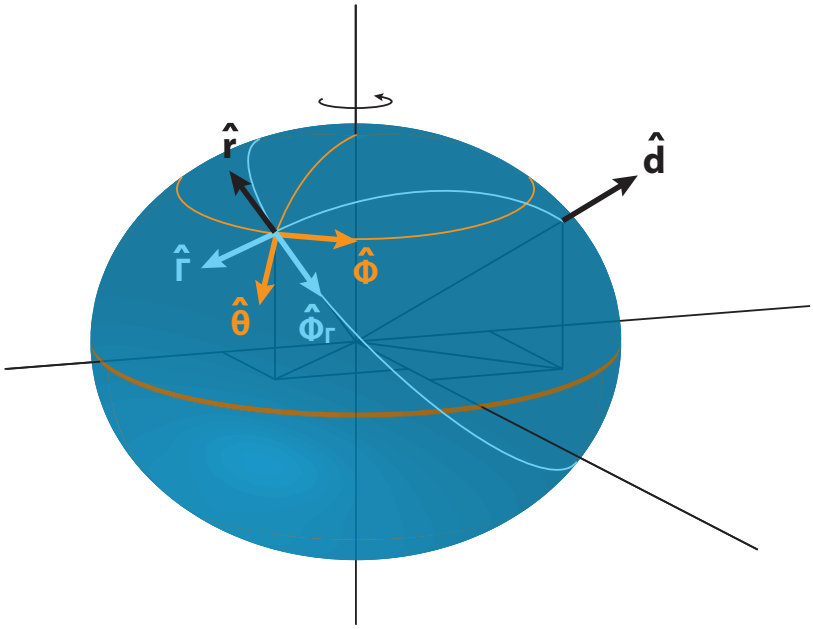

Figure 2.1: The axially symmetric coordinate system (light blue) and the body fixed system (gold) relative to each other and the standard Cartesian system. Here $\hat{r}$ describes a vector to any position of interest and $\hat{d}$ is a vector pointing toward the potential source.

2.1 Definitions of Love and Shida Numbers

A.E.H. Love introduced the dimensionless parameters h and k to describe the response of an elastic body to tidal forcing [16]. When a forcing potential, Ψ, is applied to an elastic body it will deform, and the reorientation of mass induces a change in the self-gravity of the body. At the surface ($r = R$), this additional potential is proportional to the applied potential. The total perturbation to the potential field, Φ, due to the applied potential plus reorientation can therefore be written,

$$\Phi(R) = -\left(1 + k\right)\Psi, \tag{2.1}$$

where k is that proportionality constant describing the ratio of induced and applied potentials. The negative sign ensures k remains positive (as the solution to the total potential will be negative by convention). The deformed body follows the potential and the surface will rise or fall to some degree, depending on the material properties. The Love number h

describes the ratio of radial displacement (u_r) to applied potential, such that

$$u_r(R) = \frac{h}{g_R}\Psi, \tag{2.2}$$

with the gravitational acceleration at the surface, g_R, divided out to make h a dimensionless quantity. T. Shida introduced a third parameter, l, [26] which characterizes the tangential displacement (u_Γ) as,

$$u_\Gamma(R) = \frac{l}{g_R}\partial_\Gamma\Psi. \tag{2.3}$$

Here Γ describes the co-latitudinal coordinate with respect to the potential's axis of symmetry (e.g. tidal or rotational axis). One could also write the angular displacements in spherical body fixed geographical coordinates with $u_\theta(R) = \frac{l}{g_R}\partial_\theta\Psi$ and $u_\phi(R) = \frac{l}{g_R}\frac{\partial_\phi\Psi}{\sin\theta}$. For the derivation of the equations of motion and their solutions, the axis-symmetric system is preferable. When applying the results to specific bodies, it makes more sense to use cartographic coordinates. Fig. 2.1 gives a visual representation of this, comparing the axis-symmetric coordinates with the standard cartographic spherical and Cartesian coordinates. With these definitions we see that in order to evaluate the Love numbers for a planetary body we need solutions for displacement (u_r, u_Γ) and potential (Φ) at the surface.

2.2 Elastic Deformation

Here we describe a technique for computing Love numbers largely based on the works of Sabadini and Vermeersen (2004)[23] and Jara-Orué and Vermeersen (2011)[11], but with deep roots going back to Saito (1974) [24] and farther to Alterman (1959) [2], which finds the spatially resolved solutions for potential and displacement that we need. In this chapter we will often make reference to this formulation, and refer to it as "the deformation model". We use three equations to determine the deformation of a planetary body: Poisson's (Laplace's) equation, conservation of mass, and an expression of force balance. These differential equations describe the behavior of a medium is constant rigidity and density, but with appropriate boundary conditions (Sec. 2.2.3) we can use multlayered structures having radially piece-wise constant material parameters. An important consideration in this section

is the difference between the fluid and elastic equations of motion. As we will see, in order to appropriately consider bodies with coupled elastic and fluid layers, a specific conversion must be made at these layers interfaces. In particular any fluid which is "restricted" above or below by an elastic layer can not fit the equipotential form, and so a modification must be made to treat this.

2.2.1 Equations of Motion

We require that the potential satisfy Poisson's Equation, $\nabla^2\Phi_T = 4\pi G\rho$, with G the gravitational constant and ρ representing the mass density. This potential is perturbed ($\Phi_T = \Phi_0 + \Phi$) where Φ_0 is the self gravity and Φ is the perturbation to the field due to an external forcing. In this study, we consider incompressible media so that density remains unperturbed. Under this assumption of incompressibility, the self gravity satisfies Poisson's equation, $\nabla^2\Phi_0 = 4\pi G\rho$, therefore the perturbation potential must satisfy Laplace's equation,

$$\nabla^2\Phi = 0. \tag{2.4}$$

The incompressible mass continuity equation can be expressed by,

$$\Delta \equiv \nabla \cdot \boldsymbol{u} = 0, \tag{2.5}$$

with $\boldsymbol{u} = (u_r, u_\Gamma, 0)$ the displacement vector. Notice, because of the axial symmetry in these coordinates, the azimuthal component to displacement is zero. The final equation we use is force balance. Using a standard force balance we assume that processes acting on long time scales will have vanishing inertial forces. This assumption is fine, so long that an elastic wave can propagate much faster than the source that created it can operate. Shear wave speed goes as $\sqrt{\frac{\mu}{\rho}}$, and for planetary bodies are typically on the order of kilometers per second. Even for bodies ten thousand kilometers across, it will only take hours for elastic waves to have propagated all throughout a body. The tidal forces which cause the planetary deformation we are interested in generally have periods longer than this, but it is a good idea to keep this in mind. Our force balance says that the body forces, $\boldsymbol{F}$, per unit mass acting on any element within the body must be balanced by stress, $\boldsymbol{\sigma_T}$. Thus, for an element of mass with

density ρ, its force balance expression is $\nabla \cdot \boldsymbol{\sigma_T} + \rho \boldsymbol{F} = 0$. We use the perturbed potential gradient as the body forces, $\boldsymbol{F} = -\nabla(\Phi_0 + \Phi)$, and write the stress with $\boldsymbol{\sigma_T} = \boldsymbol{\sigma} - p\boldsymbol{I}$ the sum of two terms describing the deviatoric stress and the hydro-static pressure. Here $p = p_0 - \boldsymbol{u} \cdot \nabla p_0$ is the hydro-static pressure field, made up of an unperturbed term and a term describing the change resultant from any deformation. Finally we note that in the unperturbed system the potential gradient can be written as the pressure gradient, which we know explicitly as $\rho \nabla \Phi_0 = -\nabla p_0 = \rho g \hat{\boldsymbol{r}}$. All of this combines to give us

$$\nabla \cdot \boldsymbol{\sigma} - \nabla(\rho g \; u_r) - \nabla \rho \Phi = 0. \tag{2.6}$$

The rightmost term in Φ describes the influence of the potential field, and the leftmost term in $\boldsymbol{\sigma}$ describes the resistance to the field. The center term represents the change in hydrostatic pressure that an element of mass will experience if it is displaced, which we do not want to consider as deviatoric stress. If the mass element is a fluid, and not an elastic, then it can not support deviatoric stress. As a result the force balance for a fluid element differs slightly and is written

$$-\nabla(\rho g \; u_r) - \nabla \rho \Phi = 0. \tag{2.7}$$

In Fig. 2.2 we give a visual on how a fluid would respond to a force field in comparison to an elastic. While a fluid would fit the equipotential generated by itself and the the force field, the additional "spring" force for the elastic body inhibits some of the deformation. This interpretation is helpful in applying appropriate boundary conditions for when elastic and fluid layers are coupled in multilayered bodies, which we will do later in this section.

The stress can be written in terms of strain with $\boldsymbol{\sigma} = \lambda \Delta \boldsymbol{I} + 2\mu\boldsymbol{\varepsilon}$ where $\boldsymbol{I}$ is the three dimensional identity matrix and $\Delta = Tr[\boldsymbol{\varepsilon}] = \nabla \cdot \boldsymbol{u}$ represents the trace of the strain tensor and is referred to as the "dilatation". The Lamé parameters, λ and μ, are related to the bulk and shear stress components respectively. The rigidity is given by μ and λ is related to the bulk modulus K, by $K = \lambda + \frac{2\mu}{3}$. Strain is expressed in terms of displacement by $\boldsymbol{\varepsilon} = \frac{1}{2}\left(\nabla \boldsymbol{u} + (\nabla \boldsymbol{u})^T\right)$ with superscript T referring to the transpose of the given tensor. In an incompressible medium the dilatation is technically zero, however λ becomes infinite and the product of $\lambda\Delta$ remains finite. This is considered the mean normal stress throughout the

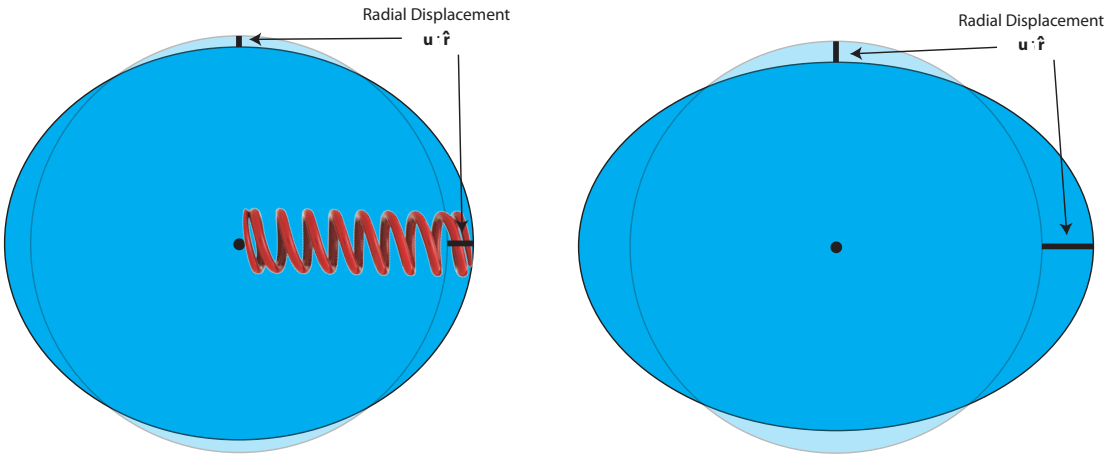

Figure 2.2: Schematic comparing the deformation in an elastic (left) and fluid (right) body due to the same potential forcing. The fluid's mass will redistribute so that the surface is an equipotential. The elastic body's deformation is prevented from becoming an equipotential by the material stored elastic energy (visualized here as a spring).

body and we must keep track of it. The elastic force balance expression becomes

$$\mu\left(\nabla^2\boldsymbol{u} + \nabla\cdot(\nabla\boldsymbol{u})^T\right) + \nabla\left(\lambda\Delta - \rho g\ u_r - \rho\Phi\right) = 0. \tag{2.8}$$

Notice that if the material is fluid, and μ and λ are both zero, we recover the fluid force balance in Eq. 2.7.

In order to determine Love numbers we are going to need solutions for the displacements $\boldsymbol{u} = (u_r, u_\Gamma, 0)$ and the potential Φ, which we find next.

2.2.2 General Solutions

We assume separability of the potential and the corresponding displacements and dilatation into a radial component and an angular component which will scale with the applied forcing potential, Ψ, like

$$\begin{aligned} u_r &= \sum_{\ell=0}^{\infty} U_\ell(r)\Psi(\Gamma) & \lambda\Delta &= \sum_{\ell=0}^{\infty} \lambda\chi_\ell(r)\Psi(\Gamma) \\ u_\Gamma &= \sum_{\ell=0}^{\infty} V_\ell(r)\partial_\Gamma\Psi(\Gamma) & \Phi &= \sum_{\ell=0}^{\infty} \varphi_\ell(r)\Psi(\Gamma). \end{aligned} \tag{2.9}$$

We are dealing with the deformation one degree at a time. In fact, we explicitly choose only $\ell = 2$ for all of our work, which is sufficient if the planetary Radius to semi-major axis is small. And so we drop the summation and the degree subscript to clean up the notation.

Because of the axis-symmetry of this problem, there is no azimuthal component to the force balance, but the spatial derivatives will still introduce higher derivatives of the potential into the expression. As the potential must satisfy Legendre's differential equation, we can use it to reduce these higher derivatives. After carrying out the appropriate derivatives on the separated potential, displacements, and dilation and performing much algebra, the radial and polar components of the momentum equation read respectively,

$$\Psi \Big(r \Big(\rho \left(U g' + g U' + \varphi' \right) - \lambda \chi' \Big) + \frac{\mu}{r} \Big(\left(4U - 4rU' - 2r^2 U'' \right) + \ell(\ell+1) \left(U - 3V + rV' \right) \Big) \Big) = 0 \tag{2.10}$$

$$\partial_{\mathrm{r}} \Psi \Big(\Big(\rho \left(U g + \varphi \right) - \lambda \chi \Big) + \frac{\mu}{r} \Big(\left(4U + rU' + 2rV' + r^2 V'' \right) - 2\ell(\ell+1) V \Big) \Big) = 0, \tag{2.11}$$

the Poisson (LaPlace) condition is written

$$\Psi \left(r\varphi'' + 2\varphi' - \frac{\ell(\ell+1)}{r} \varphi \right) = 0, \tag{2.12}$$

and the zero valued dilation (for the incompressible materials we consider)

$$\Psi \left(\frac{2}{r} U + U' - \frac{\ell(\ell+1)}{r} V \right) = 0. \tag{2.13}$$

2.2.2.1 Elastic Solutions

The solution to LaPlace's differential equation (Eq. 2.12) is

$$\varphi = c_3 \; r^{\ell} + c_6 \; r^{-(\ell+1)}, \tag{2.14}$$

with c_3 and c_6 (the labels chosen to conform to notation in references [23] [11]) constants of integration determined through boundary conditions, discussed in Sec. 2.2.3.

One might notice the similarity in the components of the momentum equations (Eqs. 2.10 and 2.11). In fact, the rigidity independent term of the radial component is just r times the derivative of rigidity independent piece of the angular component. Noticing this we take the derivative of Eq. 2.11, to solve for $\lambda\chi'_\ell$, and use this to eliminate it (as well as φ') from Eq. 2.10. Using Eq. 2.13 and its derivatives we eliminate all occurrences of V_ℓ. This results in a fourth order differential equation completely in U_ℓ which has the solutions

$$U = c_1\ r^{(\ell+1)} + c_2\ r^{(\ell-1)} + c_4\ r^{-\ell} + c_5\ r^{-(\ell+2)}, \tag{2.15}$$

with c_1, c_2, c_4, and c_5 more constants of integration for which we need boundary conditions. With this solution for U_ℓ and the incompressibility condition, Eq. 2.13, the solution for V_ℓ is just

$$V = c_1\frac{(\ell+3)}{\ell(\ell+1)}\ r^{(\ell+1)} + c_2\frac{1}{\ell}\ r^{(\ell-1)} - c_4\frac{(\ell-2)}{\ell(\ell+1)}\ r^{-\ell} - c_5\frac{1}{\ell+1}\ r^{-(\ell+2)}, \tag{2.16}$$

Solving for the mean normal stress is accomplished by substituting the solutions (Eqs. 2.14, 2.15, and 2.16) into the angular momentum expression, Eq. 2.11, to see

$$\begin{aligned}\lambda\chi = {} & c_1\frac{(\ell\rho g r - 2\mu(2\ell+3))}{\ell}\ r^{\ell} + c_2\rho g\ r^{(\ell-1)} + c_3\rho\ r^{\ell} \\ & + c_4\frac{((\ell+1)\rho g r - 2\mu(2\ell-1))}{(\ell+1)}\ r^{-(\ell+1)} + c_5\rho g\ r^{-(\ell+2)} + c_6\rho\ r^{-(\ell+1)}.\end{aligned} \tag{2.17}$$

2.2.2.2 Fluid Solutions

The solution for the potential is unchanged, but we relabel the constants from cs to fs to avoid confusion between the two media. The general solution for the potential in a fluid is

$$\varphi = f_1\ r^{\ell} + f_2\ r^{-(\ell+1)}. \tag{2.18}$$

The displacements are much easier to solve for in a fluid than they were in an elastic, because the stress term has vanished. The angular component of force balance (Eq. 2.11) in a fluid reads $\partial_\Gamma\Psi\left(\rho\left(Ug+\varphi\right)\right) = 0$, and shows that $U = -\varphi/g$

$$U = -f_1\frac{1}{g}\ r^{\ell} - f_2\frac{1}{g}\ r^{-(\ell+1)} \tag{2.19}$$

Which we use with incompressibility Eq. 2.13, and the solution for V_ℓ is just

$$V = f_1 \frac{(4\pi G\rho r - (\ell+4)g)}{\ell(\ell+1)g^2}\ r^\ell + f_2 \frac{(4\pi G\rho r + (\ell-3)g)}{\ell(\ell+1)g^2}\ r^{-(\ell+1)}, \tag{2.20}$$

2.2.3 Boundary Conditions

In order to ease in matching boundary conditions at the core, surface, or at any internal boundary it is convenient to define a set of six values, $(y_1, y_2, y_3, y_4, y_5, y_6)$ as,

$$\begin{aligned}
y_1 &= U & y_2 &= V \\
y_3 &= \sigma_{rr} = \lambda\chi + 2\mu U' & y_4 &= \sigma_{r\Gamma} = \mu\left(V' - \frac{V}{r} + \frac{U}{r}\right) \\
y_5 &= \varphi & y_6 &= \Upsilon = \varphi' + \frac{(\ell+1)}{r}\varphi + 4\pi G\rho U.
\end{aligned} \tag{2.21}$$

y_1 and y_2 describe the radial and tangential components of displacement, and y_5 is the perturbed potential. y_3 is the radial factor of the radial stress component (σ_{rr}) and y_4 is the radial factor of the shear stress component ($\sigma_{r\Gamma}$). $y_6 = \Upsilon$ is sometimes called "potential stress" but actually has units of acceleration. With the vector $\boldsymbol{y} = (y_1, y_2, y_3, y_4, y_5, y_6)$ written in terms of the general elastic solutions derived above (Eqs. 2.14, 2.15, 2.16, and 2.17), the system can be compacted into matrix form as $\boldsymbol{y} = \boldsymbol{E}\cdot\boldsymbol{c}$ with $\boldsymbol{c} = (c_1, c_2, c_3, c_4, c_5, c_6)$

the vector of boundary condition constants and

$$\boldsymbol{E} = \begin{pmatrix} r^{(\ell+1)} & r^{(\ell-1)} & 0 & \\ \frac{(\ell+3)r^{\ell+1}}{\ell(\ell+1)} & \frac{r^{\ell-1}}{\ell} & 0 & \\ \frac{r^{\ell}(2\mu((\ell-1)\ell-3)+g\ell r\rho)}{\ell} & r^{(\ell-2)}(2\mu(\ell-1)+gr\rho) & r^{\ell}\rho & \cdots \\ \frac{2\mu(\ell+2)r^{\ell}}{(\ell+1)} & \frac{2\mu(\ell-1)r^{(\ell-2)}}{\ell} & 0 & \\ 0 & 0 & r^{\ell} & \\ 4\pi G r^{(\ell+1)}\rho & 4\pi G r^{(\ell-1)}\rho & (2\ell+1)r^{\ell-1} & \end{pmatrix}$$

$$\begin{pmatrix} r^{-\ell} & r^{-(\ell+2)} & 0 \\ -\frac{(\ell-2)r^{-\ell}}{\ell(\ell+1)} & -\frac{r^{-(\ell+2)}}{\ell+1} & 0 \\ \cdots \quad \frac{r^{-(\ell+1)}(g(\ell+1)r\rho-2\mu(\ell(\ell+3)-1))}{\ell+1} & r^{-(\ell+3)}(gr\rho-2\mu(\ell+2)) & r^{-(\ell+1)}\rho \\ \frac{2\mu(\ell-1)r^{-(\ell+1)}}{\ell} & \frac{2\mu(\ell+2)r^{-(\ell+3)}}{\ell+1} & 0 \\ 0 & 0 & r^{-(\ell+1)} \\ 4\pi G r^{-\ell}\rho & 4\pi G r^{-(\ell+2)}\rho & 0 \end{pmatrix}. \tag{2.22}$$

A similar procedure on the fluid general solutions allows us to write those solutions in matrix form as well by $\boldsymbol{y} = \boldsymbol{F} \cdot \boldsymbol{f}$ with $\boldsymbol{f} = (f_1, f_2)$ the boundary condition constants and

$$\boldsymbol{F} = \begin{pmatrix} -\frac{r^{\ell}}{g} & -\frac{r^{-(\ell+1)}}{g} \\ \frac{r^{\ell}(4G\pi r\rho - g(\ell+4))}{g^2\ell(\ell+1)} & \frac{r^{-(\ell+1)}(4G\pi r\rho + g(\ell-3))}{g^2\ell(\ell+1)} \\ 0 & 0 \\ 0 & 0 \\ r^{\ell} & r^{-(\ell+1)} \\ -\frac{r^{(\ell-1)}(4G\pi r\rho - 2g(\ell+1))}{g} & -\frac{4G\pi r^{-(\ell+1)}\rho}{g} \end{pmatrix}. \tag{2.23}$$

2.2.3.1 Core Conditions

In the matrix representations for elastic (Eq. 2.22) and fluid (Eq. 2.23) one will notice that half of the solutions present (corresponding to c_4, c_5, c_6 or f_2) are irregular for $r = 0$. Therefore as our first set of boundary condition we require that for any core layer c_4, c_5, c_6 (or f_2 for a fluid core) must all equal zero.

2.2.3.2 Surface Conditions

At the surface, we require that any radial traction goes to zero and that the potential be continuous. This is the free surface condition. Explicitly, we use

$$y_3(R) = 0 \qquad y_4(R) = 0 \qquad y_6(R) = -\frac{2\ell + 1}{R}. \tag{2.24}$$

This surface value for y_6 is found by applying Gauss' law on the potential across that surface. For an elastic surface, this eliminates three of the constants of integration. If the surface is fluid the zero stress solutions are trivial, and we are left with one boundary condition which eliminates on constant of integration. In both cases, the surface eliminates half of the constants, similar to what was found from the core conditions.

2.2.3.3 Internal Boundary Conditions

If the body we are interested in is treated as homogeneous in density and rigidity, then we have all of the boundary conditions we need. One half of the constants of integration are discarded from the core condition, and the other half are determined from the surface

condition. We can also treat radially stratified bodies if we consider the planet as having some number of piece-wise continuous (in density and rigidity) layers. There are four possible types of internal interfaces, each with slightly different boundary conditions. They are 1) Elastic-Elastic, 2) Fluid-Fluid, 3) Elastic-Fluid, and 4) Fluid-Elastic. Here we will describe how in each of these cases, the constants of integration in one layer can be solved for the constants in an adjacent layer. In practice, what one does, is take the set of core constants (for which half we know are zero), and propagate those constants up to the surface. Then at the surface, the free stress condition is applied and we calculate the values of the constants in each layer. We will adopt the $-$ subscript notation on components which describe the material below some interface, and the $+$ subscript for the material above. In this section particular attention is paid for the interfaces where the media flips from fluid to elastic, or the opposite. Jara-Orue (2011) [11] accurately describes the boundary conditions at this interface, which we extend by relating these to the restricted fluid's equations of motion.

Elastic-Elastic

At an elastic-elastic boundary and also at fluid-fluid boundary all displacements, the stress, the potential, its derivative must be continuous, and therefore all six of the y-functions must as well. In matrix form we write

$$\begin{aligned} \boldsymbol{y}_- &= \boldsymbol{y}_+ \\ \boldsymbol{E}_- \cdot \boldsymbol{c}_- &= \boldsymbol{E}_+ \cdot \boldsymbol{c}_+ \end{aligned} \tag{2.25}$$

Because $\boldsymbol{E}$ is square and can be inverted, we use matrix multiplication to solve for a constant vector, for example $\boldsymbol{c}_+ = \boldsymbol{E}_+^{-1} \cdot \boldsymbol{E}_- \cdot \boldsymbol{c}_-$.

Fluid-Fluid

For the fluid-fluid surface all of the y-functions must be continuous too, but $\boldsymbol{F}$ is not square. We can make a square sub-matrix of this, though, by selecting the fifth and sixth rows, corresponding to y_5 and y_6, to say

$$\begin{aligned} \boldsymbol{y}_{56-} &= \boldsymbol{y}_{56+} \\ \boldsymbol{F}_{56-} \cdot \boldsymbol{f}_- &= \boldsymbol{F}_{56+} \cdot \boldsymbol{f}_+. \end{aligned} \tag{2.26}$$

And then, matrix multiplication gives $\boldsymbol{f}_+ = \boldsymbol{F}_{56+}^{-1} \cdot \boldsymbol{F}_{56-} \cdot \boldsymbol{f}_-$. One might notice that another appropriate sub-matrix choice could have been $\boldsymbol{F}_{12}$ or any other combination of two of the y-functions for which the sub-matrix is invertable. This is useful later, when we discuss the "tilt" parameters which relate the Love numbers, in Sec. 2.4.

Elastic-Fluid

The elastic-fluid interface also will physically need continuity of stress, potential, and radial displacement, however the chosen equations of motion for fluid media introduce a slight complication we need to recognize and take care of. The motion described for a fluid in Eq. 2.7 expects that the fluid is free to flow and will fit the shape of the equipotential. But any elastic layer most likely will not deform so much, so that when a fluid is coupled to an elastic layer from below, the fluid can not completely flow to its equipotential. It is this "restricted" fluid flow that we must track at this interface, and we describe here how to do so.

First we look at the continuity of the potential across the surface, which is,

$$\begin{aligned} y_{5-} &= y_{5+} \\ \boldsymbol{E}_{5-} \cdot \boldsymbol{c}_- &= \boldsymbol{F}_{5+} \cdot \boldsymbol{f}_+. \end{aligned} \tag{2.27}$$

Next, we track the radial displacement at the interface, which has a radius we label as $r = r$. From the elastic side the displacement here is given by $y_{1-} = \boldsymbol{E}_{1-} \cdot \boldsymbol{c}_-$. The fluid if it were unrestricted would flow to the equipotential, but bounded from below its displacement is restricted by some amount f_3, which we assume to be positive. The fluid's radial displacement can then be written

$$\begin{aligned} y_{1-} &= y_{1+} \\ \boldsymbol{E}_{1-} \cdot \boldsymbol{c}_- &= \boldsymbol{F}_{1+} \cdot \boldsymbol{f}_+ - f_3. \end{aligned} \tag{2.28}$$

For the tangential displacement we do not requite continuity. We use the incompressibility

condition of Eq. 2.5, however,to get

$$y_{2+} = \boldsymbol{F}_{2+} \cdot \boldsymbol{f}_{+} - \frac{2f_3}{\ell(\ell+1)}. \tag{2.29}$$

but this need not be continuous with the elastic y_{2-}. In effect this means we allow the fluid to flow freely to deformation laterally across the interface, without mechanical forcing from the material below.

Now consider the confined fluid's pressure state. While a fluid can not support mechanical stress, it can apply a pressure on an internal interface with a solid. Had this fluid been able to flow to its equipotential, it would have had a mean normal stress equal to zero. The confinement of the fluid causes some pressure at the interface, and though is not mechanical can be described with the mean normal stress imparted to the interface. Using the force balance from Eq. 2.11 again, we find that with shear stresses eliminated

$$\begin{aligned}
\lambda\chi_{+} &= \rho_{+}\left(U_{+}g + \varphi_{+}\right) \\
y_{3+} &= \rho_{+}y_{1+}g + \rho_{+}y_{5+} \\
y_{3+} &= \rho_{+}\left(\left(\boldsymbol{F}_{1+} \cdot \boldsymbol{f}_{+} - f_3\right)g + y_{5+}\right) \\
y_{3+} &= \rho_{+}g\left(\boldsymbol{F}_{1+} \cdot \boldsymbol{f}_{+}\right) + \rho_{+}y_{5+} - \rho_{+}gf_3.
\end{aligned} \tag{2.30}$$

For an unrestricted fluid we have $f_3 = 0$, and the fluid fits the equipotential. In this case, there is no confinement pressure and $y_{3+} = 0$ as well. It must then be, that $\rho_{+}g\left(\boldsymbol{F}_{1+} \cdot \boldsymbol{f}_{+}\right) + \rho_{+}y_{5+} = 0$ so that $y_{3+} = -\rho_{+}gf_3$ describes the fluid confinement pressure at the elastic fluid interface. At the interface the stress must be constant and so,

$$\begin{aligned}
y_{3-} &= y_{3+} \\
\boldsymbol{E}_{3-} \cdot \boldsymbol{c}_{-} &= -\rho_{+}gf_3 \\
\boldsymbol{E}_{3-} \cdot \boldsymbol{c}_{-} &= -\rho_{+}g(\boldsymbol{F}_{1+} \cdot \boldsymbol{f}_{+} - \boldsymbol{E}_{1-} \cdot \boldsymbol{c}_{-}) \\
\boldsymbol{E}_{3-} \cdot \boldsymbol{c}_{-} &= -\rho_{+}g(-\frac{\boldsymbol{F}_{5+} \cdot \boldsymbol{f}_{+}}{g} - \boldsymbol{E}_{1-} \cdot \boldsymbol{c}_{-}) \\
\boldsymbol{E}_{3-} \cdot \boldsymbol{c}_{-} &= +\rho_{+}g(\frac{\boldsymbol{E}_{5-} \cdot \boldsymbol{c}_{-}}{g} + \boldsymbol{E}_{1-} \cdot \boldsymbol{c}_{-}).
\end{aligned} \tag{2.31}$$

The normal stress condition here allows us to eliminate one of the elastic constants completely if we write $(\boldsymbol{E}_{3-} - \rho_{+}\boldsymbol{E}_{5-} - \rho_{+}g\boldsymbol{E}_{1-}) \cdot \boldsymbol{c}_{-} = 0$.

Similarly, in the tangential stress we have continuity with

$$\begin{aligned} y_{4-} &= y_{4+} \\ \boldsymbol{E}_{4-} \cdot \boldsymbol{c}_- &= 0, \end{aligned} \tag{2.32}$$

which also eliminates an elastic constant.

In similar fashion to all the other y-functions, we say y_6 is continuous across the interface, and we rewrite any displacements on the fluid side as being restricted by f_3. We have

$$\begin{aligned} y_{6-} &= y_{6+} \\ y_{6-} &= y'_{5+} + \frac{(\ell+1)}{r} y_{5+} + 4\pi G\rho_+(\boldsymbol{F}_{1+} \cdot \boldsymbol{f}_+ - f_3) \\ y_{6-} &= y_{6+} - 4\pi G\rho_+ f_3 \\ y_{6-} &= y_{6+} + \frac{4\pi G}{g} y_{3-}, \end{aligned} \tag{2.33}$$

for which we rearrange into $(\boldsymbol{E}_{6-} - \frac{4\pi G}{g}\boldsymbol{E}_{3-}) \cdot \boldsymbol{c}_- = \boldsymbol{F}_{6+} \cdot \boldsymbol{f}_+$.

Finally, we again take only the potential and potential stress rows of the fluid solution matrix so that it is invertable. At this boundary we can solve for the fluid constants in terms of the elastic constants with

$$\boldsymbol{f}_+ = \boldsymbol{F}^{-1}_{56+} \cdot \begin{pmatrix} \boldsymbol{E}_{5-} \\ \boldsymbol{E}_{6-} - \frac{4\pi G}{g}\boldsymbol{E}_{3-} \end{pmatrix} \cdot \boldsymbol{c}_-. \tag{2.34}$$

At this interface we also pick up two boundary conditions which can solve for two of the elastic constants below. They are

$$\begin{pmatrix} \boldsymbol{E}_{3-} - \rho_+\boldsymbol{E}_{5-} - \rho_+ g\boldsymbol{E}_{1-} \\ \boldsymbol{E}_{4-} \end{pmatrix} \cdot \boldsymbol{c}_- = \begin{pmatrix} 0 \\ 0 \end{pmatrix}. \tag{2.35}$$

These two boundary conditions balance out the two new constants in $\boldsymbol{f}$ that we have, for an even trade.

Fluid-Elastic

For this interface we see very similar boundary conditions as for with the elastic-fluid interface. Again the radial displacement of the fluid can not fit the fit the equipotential, because

this time it is restricted from above, and the fluid displacement is reduced by f_4. We write,

$$\begin{aligned} y_{1-} &= y_{1+} \\ \boldsymbol{F}_{1-} \cdot \boldsymbol{f}_- - f_4 &= \boldsymbol{E}_{1+} \cdot \boldsymbol{c}_+. \end{aligned} \tag{2.36}$$

The tangential displacement is not required to be continuous. We do know the value on the fluid side, as Eq. 2.5 tells us $y_{2-} = \boldsymbol{F}_{2-} \cdot \boldsymbol{f}_- - \frac{2f_4}{\ell(\ell+1)}$. The solution is unknown on the elastic side, though, and so we take it as an additional constant, f_5, we will need to solve for

$$\begin{aligned} f_5 &= y_{2+} \\ f_5 &= \boldsymbol{E}_{2+} \cdot \boldsymbol{c}_+. \end{aligned} \tag{2.37}$$

We perform the same continuity analysis as we did in the elastic-fluid case, to get

$$\begin{aligned} y_{3-} &= y_{3+} \\ -\rho_- g f_4 &= \boldsymbol{E}_{3+} \cdot \boldsymbol{c}_+, \end{aligned} \tag{2.38}$$

for σ_{rr} stress component. And for the $\sigma_{r\Gamma}$ stress have

$$\begin{aligned} y_{4-} &= y_{4+} \\ 0 &= \boldsymbol{E}_{4+} \cdot \boldsymbol{c}_+, \end{aligned} \tag{2.39}$$

The potential is continuous

$$\begin{aligned} y_{5-} &= y_{5+} \\ \boldsymbol{F}_{5-} \cdot \boldsymbol{f}_- &= \boldsymbol{E}_{5+} \cdot \boldsymbol{c}_+. \end{aligned} \tag{2.40}$$

as is the potential stress

$$\begin{aligned} y_{6-} &= y_{6+} \\ \boldsymbol{F}_{6-} \cdot \boldsymbol{f}_- - 4\pi G \rho_- f_4 &= \boldsymbol{E}_{6+} \cdot \boldsymbol{c}_+. \end{aligned} \tag{2.41}$$

As a result we are able to write the elastic constant vector in the layer above, in terms

of the fluid constants below, as

$$\boldsymbol{c}_+ = \boldsymbol{E}_+^{-1} \cdot \begin{pmatrix} \boldsymbol{F}_{1-} \cdot \boldsymbol{f}_- - f_4 \\ f_5 \\ -\rho_- g f_4 \\ 0 \\ \boldsymbol{F}_{5-} \cdot \boldsymbol{f}_- \\ \boldsymbol{F}_{6-} \cdot \boldsymbol{f}_- - 4\pi G \rho_- f_4 \end{pmatrix} \tag{2.42}$$

At this boundary we pick up two constants of integration to solve for. This makes sense, because if this next layer is also the surface then we also pick up the two free stress surface conditions, and the total balances out.

2.2.4 Viscoelastic Media

A planetary body can be treated as viscoelastic if the dissipative effects of deformation are of interest. Peltier (1974) [22] describes how the correspondence principle can be used to turn the elastic parameters into viscoelastic ones through a Fourier or Laplace transform. There are many plausible viscoelastic models for planetary bodies, however the Maxwell model is the simplest and most employed [29] [28]. In such Maxwell descriptions, the viscosity η enters in as a modification of the Lamé parameters λ and μ by,

$$\widetilde{\mu} = \mu \left(\frac{1}{1 - \mathrm{i}\Delta_\omega} \right) \qquad \widetilde{\lambda} = \lambda \left(\frac{1 - \mathrm{i}\left(\frac{K}{\lambda}\right)\Delta_\omega}{1 - \mathrm{i}\Delta_\omega} \right), \tag{2.43}$$

where the bulk modulus is $K = \lambda + \frac{2\mu}{3}$ and $\Delta_\omega = \frac{\tau_M}{\omega} = \frac{\mu}{\eta\omega}$ describes the ratio of the forcing frequency, ω, to the intrinsic response frequency of the material "The Maxwell Time", τ_M. Here, η gives the viscosity of the medium. A material with $\Delta_\omega \ll 1$ (for relatively "fast" forcing) will have Lamé parameters which are essentially real and it behave elastically, while when $\Delta_\omega \gg 1$ (for relatively "slow" forcing), the parameters are zero and the material is said to be "fluid". When $\Delta_\omega \approx 1$ the real and imaginary components are comparable and is called viscoelastic. These materials exhibit both dissipative (related to the imaginary components) and restorative qualities (related to real components). The complex Lamé parameters are

simply substituted into any deformation expression, as a last step once elastic solutions are found, to turn an elastic medium into viscoelastic.

2.3 The Homogeneous Example and Fluid Limits

The easiest example of specific solutions for this type of deformation is for a one layer body, completely homogeneous in density and rigidity. In this section, we will find the homogeneous Love numbers for both elastic and for fluid bodies. For the elastic body we can turn off the rigidity to find what is called the "fluid" Love number, but we will show how this does not recover the actual l Love number which results in a true fluid.

First, we look at the elastic Love numbers. Examining the solution matrix in Eq. 2.22, we see the solutions corresponding to the constants c_4, c_5, and c_6 all have inverse power in radius and go to infinity at $r = 0$. Thus these three constants must all be zero valued, so that the solutions remain regular at the core. We solve for the remaining three constants by requiring the free surface conditions (see Sec. 2.2.3.2).

These are sufficient boundary conditions to get the complete radial solutions for all 6 y-functions described in Eq. 2.21, and therefore the spatially resolved displacements, strain, stress, and potential. We take, $y_5(R) = -(1 + k)$, $y_1(R) = h/g_{_R}$, and $y_2(R) = l/g_{_R}$ to find the degree $\ell = 2$ Love numbers for an incompressible homogeneous elastic body are

$$k = \frac{12\pi GR^2\rho^2}{8\pi GR^2\rho^2 + 57\mu} \qquad h = \frac{20\pi GR^2\rho^2}{8\pi GR^2\rho^2 + 57\mu} \qquad l = \frac{6\pi GR^2\rho^2}{8\pi GR^2\rho^2 + 57\mu}. \tag{2.44}$$

We can normalize the rigidity ($\mu_N = \frac{\mu}{\mu_s}$) in these with a scale rigidity given by $\mu_s = \frac{8\pi GR^2\rho^2}{57}$. The Love numbers written in terms of the normalized rigidity are

$$(k, h, l) = \left(\frac{3}{2}, \frac{5}{2}, \frac{3}{4}\right) \frac{1}{1 + \mu_N}. \tag{2.45}$$

and are displayed in Fig. 2.3. If the rigidity is large, so large that the body can not deform, the body is said to be rigid. In this case all of the Love numbers are zero, as no material is displaced. Oppositely, as the rigidity approaches zero, the body is considered "fluid" and the Love numbers take on finite values. Specifically $k \to \frac{3}{2}$, $h \to \frac{5}{2}$, and $l \to \frac{3}{4}$. These are

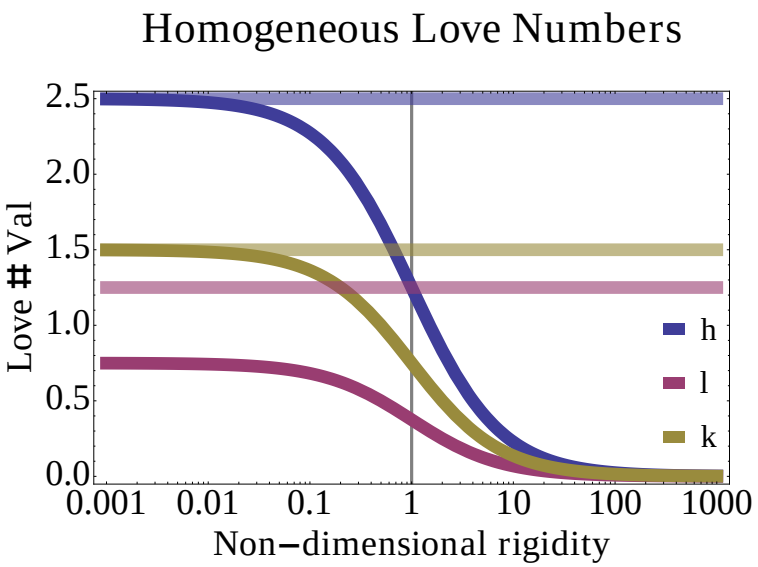

Figure 2.3: Love numbers as a function of normalized rigidity, for a homogeneous body. Solid curves give the elastic values, while transparent lines show the values predicted from fluid equations of motion.

the classic fluid Love numbers for a homogeneous body. The transparent lines represent the actual fluid Love numbers, calculated using the fluid equations of motion instead of simply letting the rigidity go to zero. Note the discrepancy in the l value, which we discuss in the next section.

Just like the elastic medium the solution must be regular at the core, and looking at Eq. 2.23 we can see that the f_2 column describes an irregular solution. Thus we set f_2 to zero. The same boundary conditions as in Eq. 2.24 hold, however, the two free stress boundary conditions are trivial because the fluid is without stress by definition. One boundary condition is sufficient and we apply $y_6(R) = -\frac{2\ell+1}{R}$ to solve for f_1. We evaluate the y-functions at the surface, to find that the degree $\ell = 2$ Love numbers for an incompressible fluid are

$$k = \frac{3}{2} \qquad h = \frac{5}{2} \qquad l = \frac{5}{4}. \tag{2.46}$$

The transparent lines in Fig. 2.3 represent these fluid Love number values. The k and h values match precisely with the "fluid limit" of their values determined by setting $\mu_N = 0$ in their elastic solutions in Eq. 2.45. The value of l, however, takes on different fluid values depending on the approach.

This results because, in the elastic formulation, the mean bulk stress $\lambda\chi$ is solved for in terms of the potential and displacements. Consequently, when the Love numbers are solved for, $\lambda\chi$ is not a parameter we can simply set to zero in taking the fluid limit (like we did with μ). What this is physically describing is that our elastic treatment of determining the Love numbers is incapable of tracking any bulk stresses which might relax, effectively ignoring any heating that dissipation might cause. It is important to point out that our tidal heating model (see Sec. 3) must then treat only the shear heating. It is reasonable to think that bulk stresses will deliver heat, however, we leave the treatment of bulk stress relaxation as a task for the future.

There is one final thing to point out is that while l has a different value, k and h take the same value in the fluid and relaxed elastic. Therefore the actual shape of the body, given by h, and the gravity field k which results from that figure are precisely the same in a true fluid and a relaxed body. Interestingly, the different l says that while the shape for a fluid and a relaxed elastic will be the same, the flow path to get from a sphere to each respective state will be different.

2.4 Love Number Relationships and "Tilt Factors"

In this section we find measurable relationships between the Love numbers, by evaluating the surface boundary conditions (see Sec. 2.2.3.2) and treating the Love numbers as additional boundary conditions. In doing so we find the familiar tilt factor, but we also find a new relationship among l and k. Because we considered the actual fluid equations of motion, and found their general solutions, we can start with a generic fluid body and say

$$\boldsymbol{F}(R)\cdot\boldsymbol{f}=\begin{pmatrix} -\frac{R^{\ell}}{g} & -\frac{R^{-(\ell+1)}}{g} \\ \frac{R^{L}(4G\pi R\rho-g(\ell+4))}{g^{2}\ell(\ell+1)} & \frac{R^{-(\ell+1)}(g(\ell-3)+4G\pi R\rho)}{g^{2}\ell(\ell+1)} \\ 0 & 0 \\ 0 & 0 \\ R^{\ell} & R^{-(\ell+1)} \\ \frac{R^{\ell-1}(2\ell g+g-4G\pi R\rho)}{g} & -\frac{4G\pi R^{-(\ell+1)}\rho}{g} \end{pmatrix}\cdot(f_1,f_2)=\begin{pmatrix} \frac{h}{g} \\ \frac{l}{g} \\ 0 \\ 0 \\ -(k+1) \\ -\frac{(2\ell+1)}{R} \end{pmatrix}. \quad (2.47)$$

Treating f_1 and f_2 as the only unknowns, we can eliminate them and reduce the four relevant equations to two. Essentially we use y_5 and y_6 to write f_1 and f_2 in terms of k, and then we use $\boldsymbol{f}$ to write y_1 and y_2 in terms of k. Specifically for any fluid surface we find

$$h = (1+k) \qquad l = \frac{4+\ell+3k-\ell k}{\ell(\ell+1)}. \tag{2.48}$$

The relationship between k and h on the left side of Eq. 2.48 hints at a well known parameter, sometimes called the "tilt factor" or "diminishing factor" [1]. This tilt factor is written,

$$\delta_1 = 1 + k - h. \tag{2.49}$$

The tilt factor is really just a measure of how off from an equipotential the body's surface sits. Looking back at Fig. 2.2, recall that a fluid body will have the surface lie on an equipotential. In both the elastic "fluid" and the true fluid we found that $k \to \frac{3}{2}$ and $h \to \frac{5}{2}$, so we see that the body assumes the fluid shape even at the fluid limit for the elastic. With these love number values the tilt factor is zero valued, and the relationship we found in Eq. 2.48 holds up. For a rigid body, if the Love numbers are zero, the tilt factor has a value of one.

The typical derivation for the tilt factor is as follows. Consider a change in the full potential at the surface of the earth. Recall from Sec. 2.2.1 that the potential is made up of two components, the self potential and perturbation due to some force. That is, ($\Phi_T = \Phi_0 + \Phi$). Our equations of motion allowed us to arrive at a solution for Φ. Specifically at the surface we know from Eq. 2.1 that $\Phi(R) = -(1+k)\,\Psi$. The self gravitational potential will also change, as the surface has vertically offset slightly. Because $\partial_r \Phi_0 = g$ and assuming that the change in surface $g_{_R}$ is negligible after deformation (as we have done so throughout this work) we can say $\Delta\Phi_0 = g_{_R} u_r(R) = h\Psi$ (where this Δ notation represents an instantaneous change from deformation for the rest of this section only). Finally we note that the change in the total potential is,

$$\begin{aligned} \Delta\Phi_T &= \Delta\Phi_0 + \Phi = h\Psi - (1+k)\,\Psi \\ &= -\Psi(1+k-h) \\ &= -\Psi\ \delta_1. \end{aligned} \tag{2.50}$$

We again have found the tilt factor δ_1. Notice that if the body is rigid and a forcing is applied, $\Delta\Phi_T = -\Psi$. This makes sense because the only change in potential is the forcing that happens to move no mass. If the body is fluid we see $\Delta\Phi_T = 0$. In this case, the forcing and reorientation potentials exactly match the change in self gravity potential. Physically, this factor is measurable using tiltmeters which note the slight difference between a plumb line and local vertical. Literally, in our equation of motion in Eq. 2.8, the $\lambda\Delta - \rho g\ u_r - \rho\Phi$, shows how the mean normal stress at the surface is proportional to the tilt factor.

We also find a new relationship between k and l in Eq. 2.48. Analogous to δ_1, this factor is,

$$\delta_2 = \frac{4 + \ell + 3k - \ell k}{\ell(\ell + 1)} - l. \tag{2.51}$$

Similarly to the classic tilt factor, δ_2 is zero valued for a fluid. This factor should, in theory, be measurable similarly how tilt is measured. Instead of deviations in plumb lines, one would measure deviations in horizontal deviations in what is "straight ahead". Like the tilt factor describes the deviation between the gravity field and local vertical relative to a fluid surface, this angular tilt factor should describe how a mass displaces in latitude from deformation relative to its fluid limit. Gravity and strain, or tilt, measurements can be combined to measure this parameter and then inverted structure models can be fit to its measurement. In practice, strain measurements can probably accomplish determination of l more easily, but δ_2 does provide one additional characterization of deformation.

A final relationship between Love numbers is realized through the boundary condition on y_6 in Eq. 2.24. Seeing y_6 again in Eq. 2.21, the term φ' represents a local change in radial component of the gravitational acceleration vector. The other terms involving φ and u_r can be rewritten in terms of Love numbers via Eqs. 2.1 and 2.2 because the boundary condition is applied at the surface. Once this is done we find $\varphi' = -\frac{\Psi\ell}{R}\delta_3$ where δ_3 is given by

$$\delta_3 = 1 - \frac{\ell + 1}{\ell}k + \frac{4\pi G\rho_{_R} R}{g_{_R}\ell}h. \tag{2.52}$$

This expression very closely resembles the "gravimetric factor" [1], however Eq. 2.52 is valid for a gravimeter at the surface where the "gravimetric factor" assumes that $\partial_r g_{_R} = \frac{2g_R}{R}$, which is useful for gravimeters off of the surface. It should be noted that for degree two

homogeneous fluid bodies the "gravimetric factor" and Eq. 2.52 predict values with a factor of two difference.

2.5 Simple Analytic Love Number Generator

Determining the Love numbers for any planetary object becomes increasingly difficult as more complicated internal structure models are considered. This section describes a unique technique to analytically determine the Love numbers of any layered planet. Our arrangement of the terms help build intuition for how the Love numbers respond to internal density and rigidity interfaces. We carry out the description in terms of the degree two k Love number here only, as that is what we will use for the global tidal heating model (see Sec. 3), however, we stress that the same technique is applicable at any degree and for the h and l Love numbers as well, except that the h, l, and k limits for the homogeneous fluid are different .

The general method is to start by asking "What would be the Love numbers, if the body was fluid?" (k_f) as well as "What would be the Love numbers, if the body was rigid?" (k_r). Here the subscript f refers to fluid and r refers to rigid. Starting with a fluid body, you then build more and more complicated structures, superposing the limits found from the less complicated structures. By calculating the two layer Love number for Io and the four layer Love number for Europa, we will demonstrate this technique. But first we re-examine the homogeneous structure

Using the deformation model described in Sec. 2.2 it is straightforward to show that for a homogeneous body, the k Love number is

$$k = \frac{12\pi G R^2 \rho^2}{8\pi G R^2 \rho^2 + 57\mu}. \tag{2.53}$$

If this body were fluid then the rigidity goes to zero and $k_f = \frac{3}{2}$, while a rigid body has infinite rigidity so $k_r = 0$. Now we write the Love number, in terms of these limits and body rigidity (μ) as,

$$k = \frac{k_f - k_r}{\left(1 + \frac{\mu}{\mu_s}\right)} + k_r = \frac{3/2}{(1 + \mu_N)}. \tag{2.54}$$

where $\mu_s = \frac{8\pi G R^2 \rho^2}{57}$ is the scale rigidity for the body. The left panel of Fig. 2.4 shows k_1 as a function of $\mu_N = \frac{\mu}{\mu_s}$. The vertical gridline shows where $\mu_N = 1$. Horizontal gridlines show the limits of the function at $k_f = \frac{3}{2}$ and $k_r = 0$ as well as the scale values at $\frac{k_f + k_r}{2}$ and $-\frac{k_f - k_r}{2}$. One purpose in wanting the Love numbers is so that we can get the imaginary part

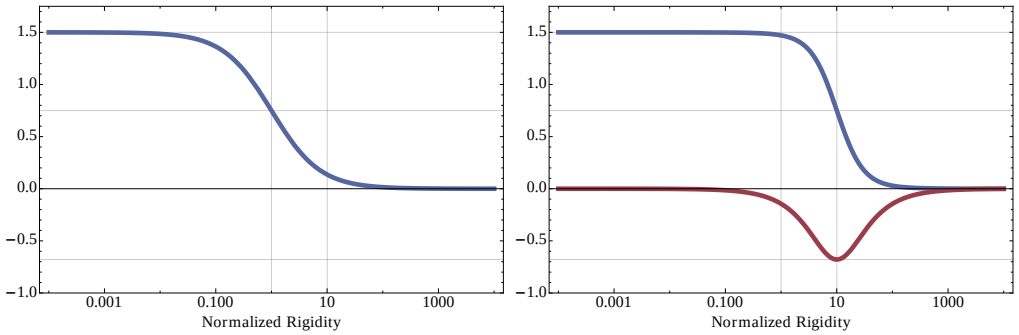

Figure 2.4: The elastic (left) and viscoelastic (right) k Love number as a function of normalized rigidity. The viscoelastic parameter Δ_ω is set to 10 to allow this model's material the time to relax, producing a large imaginary component.

to determine tidal heating rates. In a viscoelastic model, the rigidity is considered a complex value (see Sec. 2.2.4). The Maxwell model is the simplest and often employed (for example [29]) and so we use it for our purpose too. Really, the choice of rheology is best saved for the final step, implemented after the elastic Love number is found for a particular structure. In the case for this homogeneous Maxwell body we rewrite the rigidity as the viscoelastic rigidity given by $\mu_N \to \frac{\mu_N}{1 - \mathrm{i}\ \Delta_\omega}$. With this substitution the complex one layer Love number is

$$k_1 = \frac{k_f \left(\Delta_\omega^2 + 1 + \mu_N\right) + k_r\ \mu_N \left(1 + \mu_N\right)}{\left(\Delta_\omega^2 + \left(1 + \mu_N\right)^2\right)} - \mathrm{i}\frac{\left(k_f - k_r\right) \Delta_\omega\ \mu_N}{\left(\Delta_\omega^2 + \left(1 + \mu_N\right)^2\right)}. \tag{2.55}$$

The right panel of Fig. 2.4 shows the real (blue) and imaginary (red) components of k_1 as a function of μ_N again. Here we have set $\Delta_\omega = 10$, which would correspond to a system forced with a period ten time greater than the typical response time of the material. This material has some time to flow to fit its forcing and in doing so dissipates some energy, and so we find a significant imaginary component.

Using this general strategy, of examining the simpler fluid result and then the simpler rigid result and using the form in Eq. 2.54 we can build more complicated models. Next we

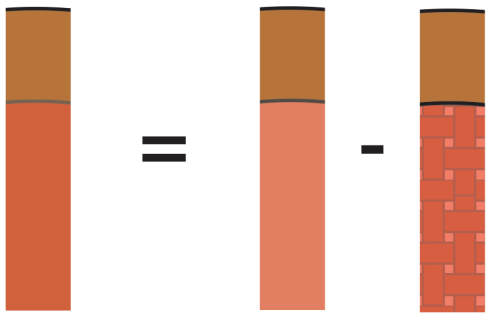

Figure 2.5: Structure cartoon for Io. The two layer elastic Love number is found by taking the difference of its fluid interior and rigid interior limits.

show how the two layer Love number can be built in a similar way, and we apply it to Io.

2.5.1 Io k

Io is modeled as a two layer body, with specifical material parameter values as described in Sec. 4.1.1. We could use the deformation model in Sec. 2.2 to explicitly calculate the Love number, however, the analytic functions become quite complicated with this method, and it is hard to make sense of. Furthermore, then taking only the imaginary component of that, so that one can apply to tidal heating models (Sec. 3) starts to push the tolerance of (or my ability with) programs like Mathematica. Instead we more intuitively build a completely analytic function out of simpler models, essentially superposed, to reconstruct the exact Love number in a more simple representation.

Our model of Io is a generic two layer body, which has a surface density and rigidity given by ρ_R and μ_R and an inner layer with a variable rigidity μ_c (which ultimately depends on the temperature of this layer). For now we set the body homogeneous in density so $\rho_c = \rho_R$. The boundary between the two layers is located at $r_I = d\ R$. We start by writing the two layer Love number we will use for Io's as

$$k_I = \frac{k_f - k_r}{\left(1 + \frac{\mu_c}{\mu_{s_c}}\right)} + k_r. \tag{2.56}$$

With $\mu_N = \mu_{N_c} = \frac{\mu_c}{\mu_{s_c}}$ normalized rigidity for the core layer.

First we find this expression's fluid limit. For this purpose, Io's fluid limit would be a model with a fluid core and an elastic lid on top. We represent this limit Love number

as $k_f = k_{fe}$. Similarly, the rigid limit has an elastic lid over the rigid core and $k_r = k_{re}$. It is convenient to introduce another simple limiting structure at this point, k_h, which is a two layer body homogeneous in rigidity but with possible density stratification. If there is no density stratification, as will be the case with our Io, then $k_h = k_1$ represents the homogeneous Love number. Now, in Eq. 2.56, if we say the inner rigidity is equal to that of the surface then $\mu_c = \mu_R$ and $k_I = k_h$. Explicitly,

$$k_h = \frac{k_{fe} - k_{re}}{\left(1 + \frac{\mu_R}{\mu_{s_c}}\right)} + k_{re}, \tag{2.57}$$

which we can invert to find that the scale rigidity in the core layer is related to the limits and the homogeneous Love number with $\mu_{s_c} = \left(\frac{k_h - k_{re}}{k_{fe} - k_h}\right)\mu_R$. Now we rewrite Io's Love number as

$$k_I = \frac{k_{fe} - k_{re}}{\left(1 + \left(\frac{k_{fe} - k_h}{k_h - k_{re}}\right)\frac{\mu_c}{\mu_R}\right)} + k_{re}. \tag{2.58}$$

Now we see that when we write Io's Love number in this form, what we need to know now are the forms for the fluid and rigid limits as well as the homogeneous rigidity structure, which we show next. First we remind ourselves, that because we are treating Io as homogeneous in density that

$$k_h = \frac{\frac{3}{2} - 0}{\left(1 + \frac{\mu_R}{\mu_s}\right)} + 0 \tag{2.59}$$

which has a value in our model of $k_h \approx 0.027$. Here the rigidity to scale rigidity ratio for Io is $\frac{\mu_R}{\mu_s} = \frac{57\mu_R}{8\pi G R^2 \rho_R^2} \approx 54.5$, so pretty rigid ($\mu_s \approx 1.2 \times 10^9 Pa$). To get the fluid and rigid limits we could again recursively set another layer (the surface) fluid and then rigid and break these down into another set of simpler models to superpose, however that is overkill in our Io where the density is constant. At this point we can just use the deformation model (Sec. 2.2) to just get these easy limits. When we look at Europa, we will need to make use of superposed models recursively. For now we report that,

$$\begin{aligned} k_{fe} &= \frac{3/2}{\left(1 + \left(\frac{24(1-d)(19d^8+38d^7+57d^6+d^5-55d^4+d^3+57d^2+38d+19)}{19(19d^9+19d^8+19d^7+64d^6+64d^5+64d^4+64d^3+24d^2+24d+24)}\right)\frac{\mu_R}{\mu_s}\right)} \\ k_{re} &= \frac{3/2}{\left(1 + \left(\frac{((8(6d^5+25d^2-42)d^2+225)d^3+38)}{19(-2d^{10}+5d^7-5d^3+2)}\right)\frac{\mu_R}{\mu_s}\right)}. \end{aligned} \tag{2.60}$$

These two functions are slightly simplified versions of general fe and re expressions, because we are not looking at the density stratification yet. If we were (and we will when we look at Europa) we would see that beside the polynomials in d we find an additional factor which depends on the density contrast. For now though, it is helpful to understand these simplified forms and, in particular, familiarize ourselves with the d polynomials. These polynomials will show up again and again, for more complicated models, at every internal interface in a structure model. So for now we will label these interface transfer functions as

$$df_1(d) = \frac{24(1-d)\left(19d^8+38d^7+57d^6+d^5-55d^4+d^3+57d^2+38d+19\right)}{19\left(19d^9+19d^8+19d^7+64d^6+64d^5+64d^4+64d^3+24d^2+24d+24\right)}$$

$$df_2(d) = \frac{\left(\left(8\left(6d^5+25d^2-42\right)d^2+225\right)d^3+38\right)}{19\left(-2d^{10}+5d^7-5d^3+2\right)}, \tag{2.61}$$

for easy reference later.

This is all we need to write out Io's full elastic Love number as

$$k_I = \frac{\frac{3/2}{(1+54.5\ df_1(d))} - \frac{3/2}{(1+54.5\ df_2(d))}}{1+\left(\frac{1-df_2(d)}{df_1(d)-1}\right)\left(\frac{1+54.5\ df_1(d)}{1+54.5\ df_2(d)}\right)\frac{\mu_C}{65\times10^9 Pa}} - \frac{3/2}{(1+54.5\ df_2(d))}. \tag{2.62}$$

In this model of Io, only the inner rigidity is viscoelastic, so to translate this Love number into viscoelastic we write $\mu_{N_c} = \left[\left(\frac{1-df_2(d)}{df_1(d)-1}\right)\left(\frac{1+54.5\ df_1(d)}{1+54.5\ df_2(d)}\right)\frac{\mu_C}{65\times10^9 Pa}\right] \rightarrow \frac{\mu_{N_c}}{1-\mathrm{i}\ \Delta_\omega}$ and

$$k_I = \frac{k_{fe}\left(\Delta_\omega^2+1+\mu_{N_c}\right)+k_{re}\ \mu_{N_c}\left(1+\mu_{N_c}\right)}{\left(\Delta_\omega^2+\left(1+\mu_{N_c}\right)^2\right)} - \mathrm{i}\frac{\left(k_{fe}-k_{re}\right)\Delta_\omega\ \mu_{N_c}}{\left(\Delta_\omega^2+\left(1+\mu_{N_c}\right)^2\right)}. \tag{2.63}$$

We convert the viscoelastic parameter Δ_ω into the viscosity η_I by $\Delta_\omega = \frac{\mu_I}{\eta_I \omega_I}$. The forcing frequency $\omega_I = n_I$ is chosen to be the orbital mean motion, because it should be the most significant frequency in Io's tide (see Sec. 3.4.1). After Hussmann and Spohn (2004) [9], we employ a power law for the viscosity such that $\eta = \eta_m \left(\frac{T}{T_m}\right)^{-27}$. The melting temperature and viscosity of that melt are for now chosen to be $T_m = 1800\ K$ and $\eta_m = 10^{13} Pa\ s$. The melting temperature of 1800 K also comes from [9], however may be on the high end of others predictions [14]. The actual chosen melting temperature only causes a horizontal (in temperature) shift of the Love number solutions (as viewed from Fig. 2.6).

In Fig. 2.6 we show the real (blue) and imaginary (red) components of Io's k Love number as a function of the dissipative region's temperature for a variety of normalized

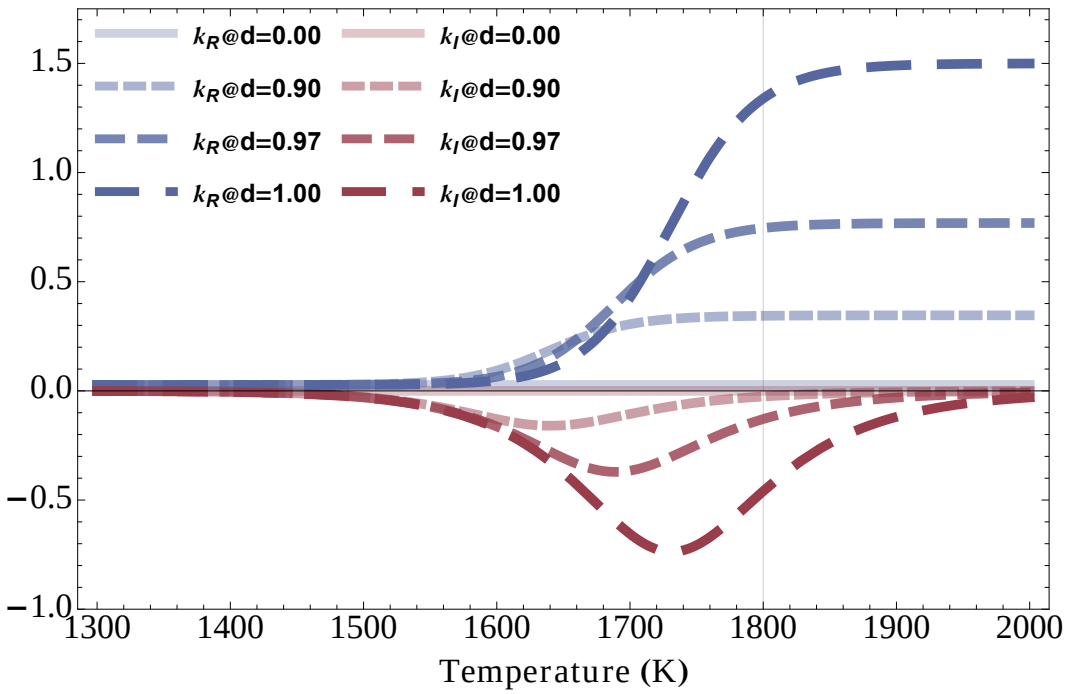

Figure 2.6: Io's k Love number for a two layer model as a function of the temperature of the viscoelastic interior. A vertical grid-line marks the prescribed melting temperature. Various d values, the normalized interface position between the inner layer and the elastic lid, are presented.

interface radii (d). Here we have chosen the forcing frequency to match Io's current mean motion ($\omega = n = 4.1 \times 10^{-5}\ s^{-1}$), however in a dynamical model, the mean motion expected to evolve with the orbit [9] [19]. Here we see that as the thickness of the convecting region increases, so does the relative magnitude of the Love number. This happens as a result of the increasing volume of material which can dissipate. Furthermore, for thicker interiors the peak of the imaginary component tends toward higher temperatures. This function for Io's k Love number will be used in the tidal heating model, when implemented into the heat balance in Sec. 4.3.

2.5.2 Europa *k*

To find Europa's Love number, we can repeatedly employ the same trick that we did for Io above. Here we will need a different set of auxiliary models (depicted in Fig. 2.7), however, the procedure is parallel. Europa is modeled as a four layer body, as described in Sec. 4.1.2. This model for Europa has constant material properties in the surface ice layer, the internal fluid ocean layer, and the silicate core. The lower ice layer, in contact with the ocean, is allowed to dissipate and therefore has a variable rigidity μ_2 (which depends on the temperature of this layer). Both the ice ocean interface, located at $r_{E1} = d_1\ R_E$, and the boundary between the ice layers, located at $r_{E2} = d_2\ R_E$, are also variable.

As we did with Io, we show a way to calculate Europa's Love number as

$$k_E = \frac{k_f - k_r}{(1 + \mu_N)} + k_r. \tag{2.64}$$

In this circumstance, if the viscoelastic ice was said to be fluid, $k_f = k_{efe}$ is a three layer model with and elastic core and surface ice, having an ice ocean interface at r_{E2}. For $k_r = k_{efr}$, we find we can use a three layer model with a rigid surface overlaying the fluid ocean. We find the normalized and scale rigidity in that layer ($\mu_N = \frac{\mu_2}{\mu_{s2}}$) by noting that if the rigidity of the viscous layer were equal to that of the surface and treated as elastic ($\mu_2 = \mu_W$), then the structure is the same as for k_{efe} but with an ice ocean interface at r_{E1}

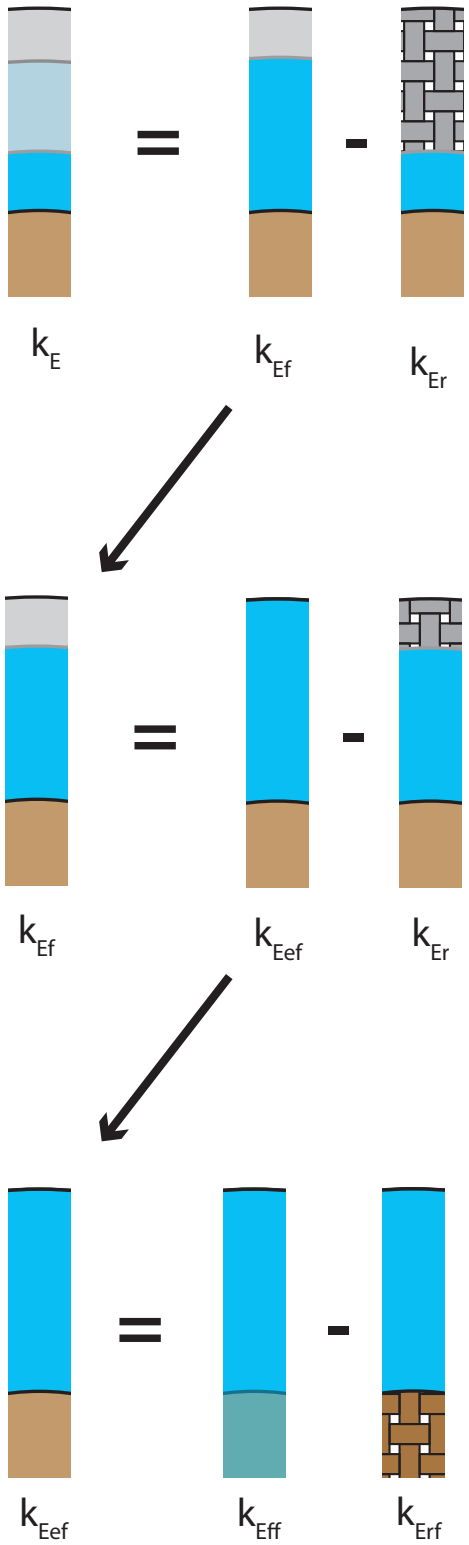

Figure 2.7: Structure cartoon for Europa. A four layer Love number is found by recursively applying the fluid-rigid difference algorithm. Layers contributions are essentially pealed off to isolate their influence and stitched back together using simpler functions.

instead. With this we find that the scale rigidity is written,

$$\mu_{s2} = \frac{(k_{efe}(d_1) - k_{efr})}{(k_{efe}(d_2) - k_{efe}(d_1))}\mu_W. \tag{2.65}$$

In order to compute Europa's Love number, all we need is the two limit functions. We start with k_{efr}, because it is the simplest of the two. This lower limit for Europa's Love number is found by putting a rigid envelope on top of the ocean. This is an interesting function because, as we shall see, it does not depend on the thickness of the rigid layer. This layer does not deform and remains completely spherical. This also means that the h and l Love numbers, when this technique is applied for them, end up zero valued. k remains positive, though, because the interior can deform and this perturbs the gravity field (for a two layer body with a rigid lid, the core can not deform as it does here). While using the deformation method in Sec. 2.2 would be hard to interpret, for the complete Europa model, it is manageable for the rigid lid model. We label the core radius and density as multiples of the surface values with $r_c = d_c\ R$ and $\rho_c = p\ \rho_W$. The deformation model then gives,

$$k_{efr} = \frac{3\ d_c^7(p-1)^2}{d_c^2\,(2p^2+p-3) + 2\frac{\mu_c}{\mu_s}}. \tag{2.66}$$

where $\mu_s = \frac{8\pi G R^2 \rho_W^2}{57}$. The rigid lower limit for Europa's Love number is a function of only the core to surface material parameter ratios, which are not variable in our case. This means that this "function" is actually single valued. Applying all of the structural parameters for Europa (see Sec. 4.1.2) we see that $\frac{\mu_c}{\mu_s} \approx 48.8$ and $k_{efr} = 0.00591$.

Getting k_{efe} is a little bit more complicated, but in finding it we will see that we can employ the same limit algorithm recursively to again use simpler models which formulate the model function we actually want. Here we are trying to construct the form of the Love number for a structure model having an elastic core and surface shell, separated by a fluid ocean. We assume that some complicated k_{efe} can be written in terms of less complicated structures (see Fig. 2.7), mainly that

$$k_{efe} = \frac{k_{ef} - k_{efr}}{(1+\mu_{Nefe})} + k_{efr}. \tag{2.67}$$

One should notice that k_{efr} is the same in both this expression and in Eq. 2.64, as a result of k_{efr} being independent of rigid shell thickness. For k_{ef} when we treat the shell as fluid,

the ocean extends to the surface. There are no structural parameters which will vary in k_{ef}, so it is a constant. We will exercise the recursion one more time, however, for clarity and to display analytic results. We will return to the form of μ_{Nefe} after constructing k_{ef}.

Here we reconstruct k_{ef} by treating the core as both fluid and then rigid. Performing the same procedure we write,

$$k_{ef} = \frac{k_{ff} - k_{rf}}{(1 + \mu_{Nef})} + k_{rf}. \tag{2.68}$$

k_{ff} and k_{rf} are two more simple models for which using the deformation model (Sec. 2.2) produces easy analytic results. Explicitly, we find that the Love numbers for these two limiting structures are

$$\begin{aligned} k_{ff} &= -\frac{3\left(d_c^5(p-1)\left(5d_c^3(p-1)+8\right)+2p+3\right)}{d_c^3(p-1)\left(9d_c^2-5(2p+3)\right)-4p-6} \\ k_{rf} &= \frac{3}{5d_c^3(p-1)+2}, \end{aligned} \tag{2.69}$$

and that the normalized core rigidity in this model is

$$\mu_{Nef} = \left(\frac{2\left(5d_c^3(p-1)+2\right)}{d_c^2(p-1)\left(4p+6-d_c^3(p-1)\left(9d_c^2-5(2p+3)\right)\right)}\right)\frac{\mu_c}{\mu_s}. \tag{2.70}$$

These functions of core parameters take on constant values, with the structure in Sec. 4.1.2 applied, and are $k_{ff} = 1.045$, and $k_{rf} = 0.249$. For Io's normalized rigidity function we have $\mu_{Nef} = 85.32$. At a value of almost 100, we see that the core is considered to be quite rigid, relatively speaking, and so we expect that $k_{ef} \approx k_{rf}$. Sure enough, when numerically evaluated we see that this is the case and that $k_{ef} = 0.258$.

Now we return to k_{efe}. We know that both of its limits are constants, and that the only parameter that can vary is the radius of the ocean ice interface which is contained within μ_{Nefe}. Organizing the function this way, we can use the deformation model once again to solve for the normalized rigidity in the ice as a function of some arbitrary depth d and find,

$$\begin{aligned} \mu_{Nefe}(d) = df_1(d)\times \\ \left(\frac{2\left(d_c^2\left(2p^2+p-3\right)+2\frac{\mu_c}{\mu_s}\right)}{d_c^2(p-1)\left(-9d_c^5(p-1)+5d_c^3\left(2p^2+p-3\right)+10d_c\frac{\mu_c}{\mu_s}+4p+6\right)+4\frac{\mu_c}{\mu_s}}\right)\frac{\mu_W}{\mu_s}. \end{aligned} \tag{2.71}$$

Notice that we see at the ice ocean interface (a fluid below an elastic type interface) the same function ($df_1(d)$) as we found when we were exploring Io's fluid interior limit. This transition function will always appear in the normalized rigidity any time the layer below is fluid. It can, in effect, be used for any general planetary model for which there is a shell over an ocean. This is a particularly useful tool for determining Love numbers for outer solar system satellites with subsurface oceans and ice shells. The other factor depends only on core and surface ice parameters which again do not vary, and so this factor is just a constant with a value of 8.11. Finally, we write the fluid limit for the Europa model, k_{efe}, as a function of arbitrary ice ocean interface radius as

$$k_{efe}(d) = \frac{0.258 - 0.00591}{(1 + 8.11\ df_1(d))} + 0.00591. \tag{2.72}$$

Now we have the tools needed to write out the actual Love number for Europa. We repeat Eq. 2.64 with the normalized rigidity for the viscoelastic region replaced using Eq. 2.65 and our simple versions for the limits (and the limits of limits, and so on). Explicitly, our prediction for the k Love number for a four layer Europa is written by

$$k_E = \frac{\frac{0.258-0.00591}{(1+8.11\ df_1(d_2))}}{\left(1 + \left(\frac{(1+8.11\ df_1(d_1))}{(1+8.11\ df_1(d_2))} - 1\right)\frac{\mu_2}{3.5\times10^9 Pa}\right)} + 0.00591. \tag{2.73}$$

The lower ice is considered viscoelastic, so, just as we did with Io, we convert the elastic Love number into the viscoelastic form (see Sec. 2.2.4) by $\mu_{N_2} = \left[\left(\frac{(1+8.11\ df_1(d_1))}{(1+8.11\ df_1(d_2))} - 1\right)\frac{\mu_2}{3.5\times10^9 Pa}\right] \rightarrow \frac{\mu_{N_2}}{1-\mathrm{i}\ \Delta_\omega}$ and we obtain the complex Love number result,

$$k_E = \frac{k_{efe}(d_2)\,(\Delta_\omega^2 + 1 + \mu_{N_2}) + k_{efr}\ \mu_{N_2}\,(1 + \mu_{N_2})}{\left(\Delta_\omega^2 + (1 + \mu_{N_2})^2\right)} - \mathrm{i}\frac{(k_{efe}(d_2) - k_{efr})\,\Delta_\omega\ \mu_{N_2}}{\left(\Delta_\omega^2 + (1 + \mu_{N_2})^2\right)}. \tag{2.74}$$

We again convert the viscoelastic parameter Δ_ω into the viscosity η_E with $\Delta_\omega = \frac{\mu_2}{\eta_E \omega_E}$, where the forcing frequency will be Europa's mean motion ($\omega_E = n_E$). Just as before, we use the same power law for the viscosity with $\eta = \eta_m \left(\frac{T}{T_m}\right)^{-27}$. For Europa, we are choosing the melting temperature for water and melt viscosity to be $T_m = 273\ K$ and $\eta_m = 10^{13} Pa\ s$.

We present the four layer Europan Love number in Fig. 2.8. Each panel shows a different ice ocean boundary location, and various ice ice interface locations. In general the pattern we find is that for thicker dissipative regions, the imaginary component of the Love number has

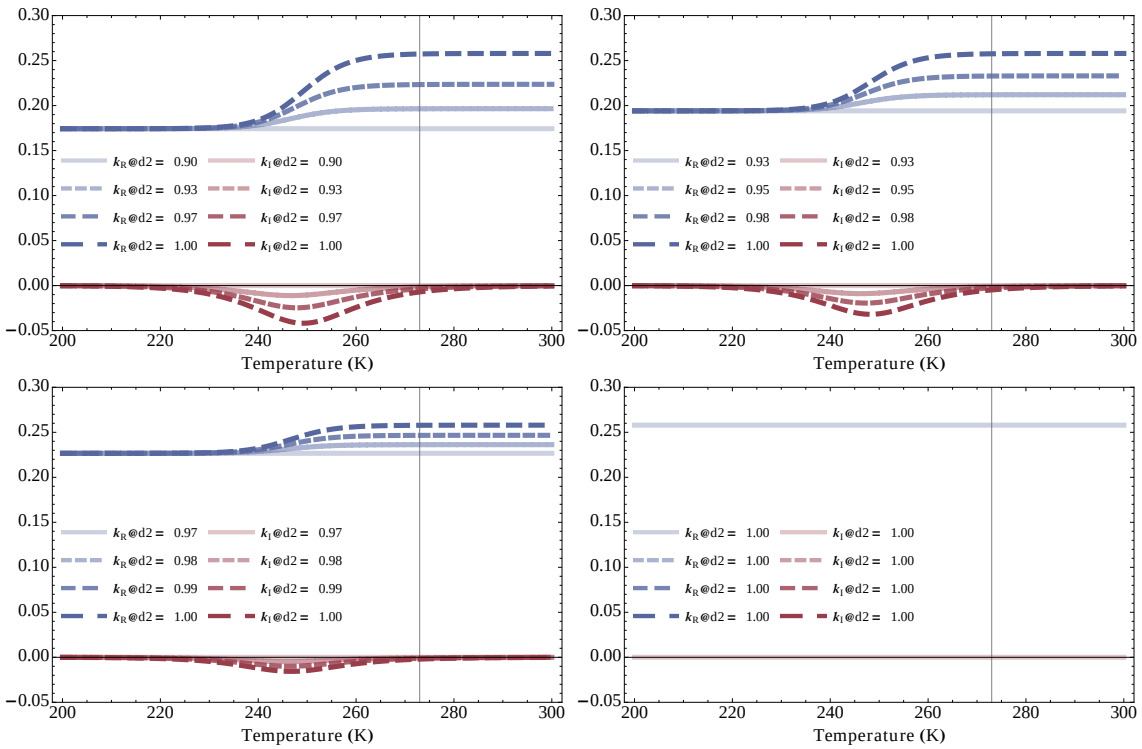

Figure 2.8: Europa's k Love number as a function of the viscoelastic ice temperature. The vertical grid-line marks the ice melting temperature. Each panel represents individual ice ocean boundary locations. Starting left to right top to bottom, the panels give $d_1 = 0.9$, 0.93, 0.97, and 1.00. The distinct dashed curves represent different internal ice-ice boundary locations.

greater magnitudes. This makes sense, because tidal heating should be related to the volume of the region which can dissipate energy. For the real components, generally d_1 controls the magnitude of rigid shell limit for Europa k_{efr}, and d_2 controls fluid limit k_{efe} value.

Conclusion

We have presented a new method for calculating the k Love number for any multi-layered planetary body, in accompaniment of a general discussion of planetary deformation and geodesy, and the parameters that measure it. In doing so, we have shown how a classic assumption concerning bulk stress relaxation has resulted in a factor of $\frac{5}{3}$ difference in the known value of the l Shida number at the homogeneous fluid limit versus in a true fluid. This discrepancy results from taking only $\mu = 0$ in the fluid limit, which only drives the elastic shear terms to zero, and neglects the dissipation which should occur in bulk terms as well. Carrying out Love number theory with true fluid equations of motion predicts an actual degree two fluid Shida number of $l = \frac{5}{4}$ (see Eq. 2.46). The fluid equations of motion also allowed us to determine a new relationship between the l and k Love numbers directly analogous to the "tilt factor" described in current literature (Eq. 2.51). In demonstrating our unique superposition technique, we calculate k for Io (Eq. 2.62) and Europa (Eq. 2.73). The analytic results for these increasingly complicated internal structures are surprisingly simple.

CHAPTER 3

Tidal Heating

Introduction

Tidal heating is a significant source of internal energy for a variety of bodies in the solar system. In addition to its influence on the evolution of planetary interiors, this energy is drawn from the planet's orbit and is the cause of orbital evolution as well. A common conclusion of tidal heating models is that the dissipation rate is linearly proportional to the imaginary component of the k Love number. We present an alternative model of tidal heating based in elastic deformation, and find that tidal heating depends on the mixed products of displacements. We show how our solutions in displacement can collapse into the classical formulation which uses the gravity Love number. This provides an integral representation for k. Furthermore, our model is spatially resolved in three dimensions, allowing analysis of tidal heating distributions within a planet. Our model also allows for examinations of dissipation at every frequency in the spectrum of an orbit, while the classic formulation has underlying assumptions about orbital configuration and frequencies, which are often unpublished and unappreciated. Especially when obliquity is large or if the body does not rotate synchronously, we find that dissipation at these frequencies can deposit more energy than what would be described be classic formulations. We do recover the classic description of tidal heating, however, only under the strict assumptions that and obliquity and eccentricity are small enough to linearize and all but the orbital frequency can be ignored.

As any body orbits its parent, a time variable gravity field causes tidal deformation of the body. This can happen for three major reasons; an eccentric orbit, an oblique spin pole, and rotation which is not synchronous to the orbit. An eccentric orbit causes the distance from

the parent to vary, as well as a libration in longitude of the sub-primary point. Any obliquity of the spin axis will also cause the sub-primary location to bounce back and forth in latitude across the equator. Finally, if the spin rate is not yet synchronized to the mean motion of the orbit, the gravity field will be even more complicated as the sub-primary point will circulate around the body in addition to the latitudinal and longitudinal variations resultant from eccentricity and obliquity. The only example of a static gravity field would be for the perfectly circular orbit of a non-oblique synchronous rotator. As a result of these orbital and rotational influences, the gravity raises a periodic tidal bulge which globally flexes the body. As the body distorts, frictional effects in the material dissipate some gravitational energy. This reduces some of the tidal motions in exchange for frictional heat and is called tidal heating.

Tidal heating can deposit a considerable amount of energy into a body, especially significant in smaller bodies which may have already lost most of their primordial heat. Tidal models are used to envision the thermal evolution and history of planetary bodies (e.g. Peale (1978) [20]) as well as the evolution of their orbits (e.g. Kaula (1964)[13]). In fact, models suggest a tidal origin for the observed volcanism on Io [21] [19]. More modern studies, such as Beuthe (2013) [5] and Tobie (2005) [28], give detailed techniques to arrive at the radially resolved heating solutions, applicable in multilayered bodies. A concise examination of the influence of spin pole obliquity is provided by Wisdom (2008) [30]. A result of these studies is that the globally integrated tidal heating rate will reduce to become linear in the imaginary component of the Love number, k_I, and can be written

$$\dot{Q} = -\frac{3}{2}\frac{n^5 R^5}{G} k_I \left(7e^2 + \sin^2 o\right). \tag{3.1}$$

Here e and o are the orbital eccentricity and spin obliquity respectively. R gives the radius of the body, and n its mean motion. Finally, G is the gravitational constant. Wisdom very correctly points out that this formulation is only valid at small eccentricity and obliquity, and mentions that the body must be homogeneous [30]. These are important points, and often overlooked. We will demonstrate the eccentricity and obliquity assumptions and further argue that this expression only holds for the component of the tide acting at the orbital

frequency, or mean motion n. This is limiting as tidal dissipation will intrinsically operate at the wide variety of frequencies present in the tide, which we explore. We will also explore the claim that homogeneity is required to arrive at this solution. In essence, the aim of this paper is to assemble the various formulations into a complete and general description and to identify the scenarios in which our model diverges from classic descriptions (Eq. 3.1).

The remainder of this document is divided into a variety of sections. First in Sec. 3.1, we derive the functional form for elastic energy density, and isolate the restorative and dissipation terms. In Sec. 3.2, we go through a method to determine the complete tidal potential spectrum for a general body, and then present the spherical harmonic degree $\ell = 2$ results. When we apply the tidal spectrum to the elastic energy density, we get the spatially resolved tidal heating rate at each distinct frequency in the tide. Then in Sec. 3.3 we integrate this over the volume of a body to get its global tidal heating rate. Finally, we present a few case studies in Sec. 3.4. First we explore synchronous rotators, comparing our result to classic theory, in order to identify the assumptions and limitations of classic tidal heating. Then we explore a large obliquity scenario, in Venus, followed by an example of spin-orbit resonance in Mercury. We conclude with a summary of our model and general inferences and results.

3.1 Strain Energy Density

Our method of determining the tidal dissipation within a body comes from a continuum mechanics perspective. This is similar to the "micro approach" discussed by Beuthe (2013) [5] and the technique of Tobie (2005) [28]. From this perspective we can examine how the tidally induced strain within a body stores and dissipates energy. In a strained body, a unit of mass sees a volumetric strain energy density, Ξ, given by

$$\Xi = \frac{\sigma_{ij}\varepsilon_{ij}}{2}, \tag{3.2}$$

where the deviatoric stress and strain tensor elements are given by σ_{ij} and ε_{ij} respectively and summation over the indicies i and j is implied. Taking a time derivative produces

$$\dot{\Xi} = \frac{1}{2}\left(\sigma_{ij}\dot{\varepsilon}_{ij} + \dot{\sigma}_{ij}\varepsilon_{ij}\right). \tag{3.3}$$

It is not necessary to do so in order to determine the tidal heating rate, however, assuming an incompressible medium simplifies the analytic expressions. For ease of reading and to build intuition, the remainder of this document focuses on an incompressible body, though we want to convey that a similar analysis can be carried out for compressible bodies as well. Using the Lamé parameters λ and μ (where μ is the material rigidity) stress can be written in terms of strain with $\sigma_{ij} = \lambda\delta_{ij}\varepsilon_{kk} + 2\mu\varepsilon_{ij}$. To conserve mass in an incompressible body, the strain matrix is zero ($\delta_{ij}\varepsilon_{ij} = 0$), and strain energy density becomes

$$\Xi_{inc} = \mu\varepsilon_{ij}\varepsilon_{ij}. \tag{3.4}$$

Then, taking the time derivative we see,

$$\dot{\Xi}_{inc} = 2\mu\varepsilon_{ij}\dot{\varepsilon}_{ij}. \tag{3.5}$$

Because the strain is time dependent and oscillates in magnitude at the many frequencies in a body's orbit and rotation, the strain tensor can be represented by a Fourier series in frequency, ω by the transformation

$$\varepsilon_{ij} = \sum_{\omega} \widetilde{\varepsilon}_{ij}\, e^{\mathrm{i}\omega t}, \tag{3.6}$$

where the sum is over all frequencies in whatever forces the strain (in our case the tidal potential, which we will momentarily describe), $\mathrm{i} = \sqrt{-1}$ is the imaginary number, and $\widetilde{\varepsilon}_{ij}$ can be complex and frequency dependent. If we consider the strain energy rate one frequency contribution, ω, at a time, we find

$$\dot{\Xi}_{inc} = \mathrm{i}\ 2\ \omega\ \mu\ \varepsilon_{ij}\varepsilon^{*}_{ij} = \mathrm{i}\ 2\ \omega\ \mu\ \widetilde{\varepsilon}_{ij}\widetilde{\varepsilon}^{*}_{ij}\ . \tag{3.7}$$

Therefore, if we know the strain tensor and we can write it as a Fourier series, as in Eq. 3.6, then we know the strain energy density is given by Eq. 3.7.

3.1.1 Viscoelastic Models

Planetary bodies are typically subject to forcing at a variety of frequencies, and should behave viscoelastically rather than purely elastically. Peltier (1974) [22] describes how the correspondence principle can be used to turn the elastic parameters into viscoelastic ones through a Fourier or Laplace transform. There are many plausible viscoelastic models for planetary bodies, however the Maxwell model is the simplest and most employed [29] [28]. In such Maxwell descriptions, the viscosity η enters in as a modification of the Lamé parameters λ and μ by,

$$\widetilde{\mu} = \mu \left(\frac{1}{1 - \mathrm{i}\Delta_\omega} \right) \qquad \widetilde{\lambda} = \lambda \left(\frac{1 - \mathrm{i}\left(\frac{K}{\lambda}\right)\Delta}{1 - \mathrm{i}\Delta_\omega} \right), \tag{3.8}$$

where the bulk modulus is $K = \lambda + \frac{2\mu}{3}$ and $\Delta_\omega = \frac{\tau_M}{\omega} = \frac{\mu}{\eta\omega}$ describes the ratio of the forcing frequency, ω, to the intrinsic response frequency of the material "The Maxwell Time", τ_M. Here, η gives the viscosity of the medium. A material with $\Delta_\omega \ll 1$ (for relatively "fast" forcing) will have Lamé parameters which are essentially real and it behave elastically, while when $\Delta_\omega \gg 1$ (for relatively "slow" forcing), the parameters are zero and the material is said to be "fluid". When $\Delta_\omega \approx 1$ the real and imaginary components are comparable and is called viscoelastic. These materials exhibit both dissipative (related to the imaginary components) and restorative qualities (related to real components). The complex Lamé parameters are simply substituted into any deformation expression to turn an elastic medium into viscoelastic.

Looking at Eq. 3.7 we can see that, because $\widetilde{\varepsilon}_{ij}\widetilde{\varepsilon}^*_{ij} = Abs[\widetilde{\varepsilon}_{ij}]^2$ is surely real, the only complex factor is $\mu \rightarrow \widetilde{\mu}$ and

$$\dot{\Xi}_{inc} = -2\ \omega\ Im[\widetilde{\mu}]\ Abs[\widetilde{\varepsilon}_{ij}]^2 + \mathrm{i}\ 2\ \omega\ Re[\widetilde{\mu}]\ Abs[\widetilde{\varepsilon}_{ij}]^2, \tag{3.9}$$

where "*Abs*", "*Re*", and "*Im*" respectively give the absolute value, real, and imaginary components of their argument. Notice that the imaginary component, $Im[\dot{\Xi}_{inc}]$, represents the recoverable elastic energy stored by deformation (in a completely elastic scenario, where $\widetilde{\mu}$ is real, it is the only term present), while the real component, $Re[\dot{\Xi}_{inc}]$, gives the strain energy dissipated as heat due to viscous frictional effects. With this we isolate the restorative

and dissipative terms and write

$$\dot{\Xi}_{inc,rest} = 2\ \omega\ Re[\widetilde{\mu}]\ Abs[\widetilde{\varepsilon}_{ij}]^2$$
$$\dot{\Xi}_{inc,diss} = -2\ \omega\ Im[\widetilde{\mu}]\ Abs[\widetilde{\varepsilon}_{ij}]^2. \tag{3.10}$$

3.1.2 Displacement, Strain, and Stress

In order to arrive at the viscoelastic heating rate we need to first examine the strain tensor (and the stress tensor if one wishes to consider a compressible medium). We use the method of solving for displacements, stress, and potential given in Sabadini and Vermeersen (2004) [23]. They give a concise treatment for solving for the basis functions which describe a body's spheroidal deformation by employing normal mode theory. They further show how the propagation matrix technique extends these solutions to consider multi-layered bodies. Additionally, Jara-Orue (2011) [11] gives a technique to include fluid layers in the structure. In particular, they show how the deformation solution's can be written in terms of radial factors (the "y-functions") which account for the radial stratification of a multilayered body. With the y-functions and the imposed potential (evaluated at the surface), Ψ, they give displacements (u_r, u_θ), stress (σ_{rr}, $\sigma_{r\theta}$), as well as potential and "potential stress" (Φ, Υ) as

$$\begin{aligned} u_r &= y_1(r)\ \Psi(\theta,\phi,t) & u_\theta &= y_2(r)\ \partial_\theta\Psi(\theta,\phi,t) \\ \sigma_{rr} &= y_3(r)\ \Psi(\theta,\phi,t) & \sigma_{r\theta} &= y_4(r)\ \partial_\theta\Psi(\theta,\phi,t) \\ \Phi &= y_5(r)\ \Psi(\theta,\phi,t) & \Upsilon &= y_6(r)\ \Psi(\theta,\phi,t). \end{aligned} \tag{3.11}$$

Here, r, θ, and ϕ are the radius and cartographic co-latitude and longitude for an arbitrary point in the body and t is the time coordinate. The specific solutions to y_1 through y_6 are determined by demanding the solutions are finite at the core, that surface be void of radial traction (free stress boundary condition), and by requiring continuity of displacements, stress, and potential across any internal material interface. These boundary conditions are sufficient to determine the deformation solutions in all three spatial dimensions throughout the entire body (see Sec. 2.2.3).

Using the "y-functions" and a deforming potential (Ψ) for any multi-layered body we

can now write out the displacement vector as

$$\boldsymbol{u} = (u_r, u_\theta, u_\phi) = \left(y_1 \ \Psi, y_2 \ \partial_\theta \Psi, y_2 \ \frac{\partial_\phi \Psi}{\sin\theta} \right). \tag{3.12}$$

with which we use to determine the strain tensor with

$$\boldsymbol{\varepsilon} = \frac{1}{2} \left(\nabla \boldsymbol{u} + (\nabla \boldsymbol{u})^T \right), \tag{3.13}$$

where T superscript indicates transpose. When the derivatives are carried out the strain tensor becomes

$$\boldsymbol{\varepsilon} = \begin{pmatrix} \partial_r y_1 \Psi & \frac{(y_1 - y_2 + r\partial_r y_2)\partial_\theta \Psi}{2r} & \frac{(y_1 - y_2 + r\partial_r y_2)\csc(\theta)\partial_\phi \Psi}{2r} \\ \frac{(y_1 - y_2 + r\partial_r y_2)\partial_\theta \Psi}{2r} & \frac{y_1 \Psi + y_2 \partial_{\theta,\theta} \Psi}{r} & \frac{y_2 \left(\partial_{\theta,\phi} \Psi - \cot(\theta)\partial_\phi \Psi \right) \csc(\theta)}{r} \\ \frac{(y_1 - y_2 + r\partial_r y_2)\csc(\theta)\partial_\phi \Psi}{2r} & \frac{y_2 \left(\partial_{\theta,\phi} \Psi - \cot(\theta)\partial_\phi \Psi \right) \csc(\theta)}{r} & \frac{y_1 \Psi - y_2 \left(\ell(\ell+1)\Psi + \partial_{\theta,\theta} \Psi \right)}{r} \end{pmatrix}, \tag{3.14}$$

where we have used the spherical harmonic differential equation (which our potential must satisfy, and introduces the degree of the potential, ℓ, into the expression) to eliminate $\partial_{\phi,\phi}\Psi$. Notice here that every element of the strain tensor is linear in Ψ and its spatial derivatives. This means that if the potential can be written in a Fourier series as $\Psi = \widetilde{\Psi}\, e^{\mathrm{i}\omega t}$, then so can the strain tensor as Eq. 3.6 and we are able to express the complex strain energy density with Eq. 3.9.

Next, we map from strain to stress using,

$$\boldsymbol{\sigma} = \boldsymbol{I} \left(y_3 - 2\mu \partial_r y_1 \right) \Psi + 2\mu \boldsymbol{\varepsilon}, \tag{3.15}$$

where $\boldsymbol{I}$ represents the 3x3 identity matrix. This produces a stress tensor of the form

$$\boldsymbol{\sigma} = \begin{pmatrix} y_3 \Psi & y_4 \partial_\theta \Psi & y_4 \csc(\theta) \partial_\phi \Psi \\ y_4 \partial_\theta \Psi & \frac{(r y_3 + 2\mu(y_1 - r\partial_r y_1))\Psi + 2\mu y_2 \partial_{\theta,\theta} \Psi}{r} & \frac{2\mu y_2 \left(\partial_{\theta,\phi} \Psi - \cot(\theta)\partial_\phi \Psi \right) \csc(\theta)}{r} \\ y_4 \csc(\theta) \partial_\phi \Psi & \frac{2\mu y_2 \left(\partial_{\theta,\phi} \Psi - \cot(\theta)\partial_\phi \Psi \right) \csc(\theta)}{r} & \frac{\Psi(r y_3 + 2\mu(y_1 - \ell(\ell+1) y_2 - r\partial_r y_1)) - 2\mu y_2 \partial_{\theta,\theta} \Psi}{r} \end{pmatrix}, \tag{3.16}$$

where we have used the relationship $\partial_r y_2 = \frac{y_4}{\mu} + \frac{y_2}{r} - \frac{y_1}{r}$ (coming from the definition of shear stress) to simplify the $\sigma_{r\theta}$ and $\sigma_{r\phi}$ terms. This tensor is also linear in Ψ and its spatial derivatives, and so it can (similarly to the strain tensor) be written as a Fourier series.

3.1.2.1 Surface Stress

Surface stresses are often considered in a geologic context as a plausible source of surface features on bodies like Europa, for example [29]. For completeness we present the surface stress tensor as well. Here at the surface, the "y"-functions reduce to the Love numbers, by definition $y_1(R) = \frac{h}{R}$ and $y_2(R) = \frac{l}{g_R}$. Also, the surface sees no radial traction so $y_3(R) = 0$ and $y_4(R) = 0$. If the surface is incompressible then also $\partial_r y_1 = \frac{\ell(\ell+1)y_2}{r} - \frac{2y_1}{r}$. This reduces the stress tensor to

$$\boldsymbol{\sigma}_{R} = \frac{2\mu_{R}}{Rg_{R}} \begin{pmatrix} 0 & 0 & 0 \\ 0 & (3h + \ell(\ell+1)l)\Psi + l\partial_{\theta,\theta}\Psi & l(\partial_{\theta,\phi}\Psi - \cot(\theta)\partial_{\phi}\Psi)\csc(\theta) \\ 0 & l(\partial_{\theta,\phi}\Psi - \cot(\theta)\partial_{\phi}\Psi)\csc(\theta) & (3h + 2\ell(\ell+1)l)\Psi - l\partial_{\theta,\theta}\Psi \end{pmatrix}. \quad (3.17)$$

In this simple form, any body's surface stress tensor can be determined from the external forcing potential (Ψ), the surface rigidity (μ_{R}), and the body's Love numbers (h and l).

3.1.3 A Convenient Factorization

Squaring the absolute value of each element in the strain tensor and then summing them all, produces quite a mess that is hard to draw any intuition from. It is helpful to decompose $\varepsilon_{ij}\varepsilon^*_{ij}$ into radially and angularly dependent factors. Contracting the strain tensor (Eq. 3.14) with its conjugate involves many terms, however, when organized appropriately becomes

manageable. If we define

$$
\begin{aligned}
pf_1 &= Abs[\,\Psi\,]^2 \\
pf_2 &= \frac{Abs[\,\partial_\theta \Psi\,]^2 + \csc^2(\theta) Abs[\,\partial_\phi \Psi\,]^2}{2} \\
pf_3 &= 2Abs[\,\partial_{\theta,\theta}\Psi\,]^2 + 2\csc^2(\theta) Abs[\,(\partial_{\theta,\phi}\Psi - \cot(\theta)\partial_\phi \Psi)\,]^2 \\
&\qquad + \ell\,(\ell+1)\,(\Psi \partial_{\theta,\theta}\Psi^* + \Psi^* \partial_{\theta,\theta}\Psi)
\end{aligned}
\tag{3.18}
$$

and

$$
\begin{aligned}
rf_1 &= \frac{Abs[\,y_1\,]^2 + Abs[\,r\partial_r y_1\,]^2 + Abs[\,y_1 + r\partial_r y_1\,]^2}{r^2} \\
rf_2 &= \frac{Abs[\,y_1 - y_2 + r\partial_r y_2\,]^2}{r^2} \\
rf_3 &= \frac{Abs[\,y_2\,]^2}{r^2}
\end{aligned}
\tag{3.19}
$$

then we can write

$$
\varepsilon_{ij}\varepsilon_{ij}^* = pf_1 rf_1 + pf_2 rf_2 + pf_3 rf_3. \tag{3.20}
$$

This factorization separates the radial terms (which carry the planetary body's structural information) from the potentially dependent terms (which carry the temporal and lateral terms). We will see, in Sec. 3.3, how arranging the terms this way simplifies the volume integrals one must use to find the global energy rate. For now, we implement these rf and pf functions explicitly into our energy density expression to say

$$
\begin{aligned}
\dot{\Xi}_{inc,rest} &= 2\ \omega\ Re[\widetilde{\mu}]\ \ (pf_1 rf_1 + pf_2 rf_2 + pf_3 rf_3) \\
\dot{\Xi}_{inc,diss} &= -2\ \omega\ Im[\widetilde{\mu}]\ \ (pf_1 rf_1 + pf_2 rf_2 + pf_3 rf_3)\,.
\end{aligned}
\tag{3.21}
$$

3.2 Tidal Potential

We need some type of deforming potential as an input for Ψ in the strain energy density we found in Sec. 3.1. The major requirements of this potential are that it can be written in terms of spherical harmonics and that it can be represented with a Fourier series as $\Psi = \widetilde{\Psi}\ e^{\mathrm{i}\omega t}$. A forcing potential could, for example, be the centrifugal potential which causes rotational flattening. For our purpose, we examine the tidal potential.

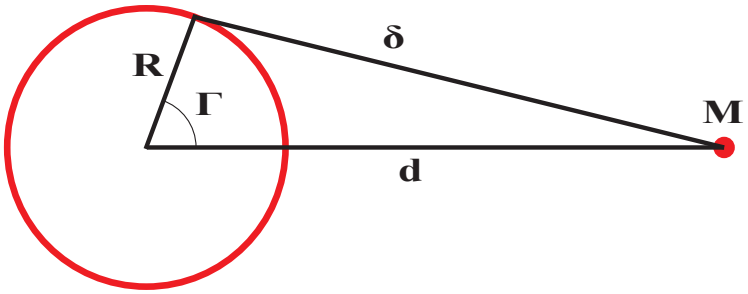

Figure 3.1: Tidal geometry in an arbitrary system. The gravitational potential at the surface of a body with radius, R, due to the point point mass, M, which is δ distance units away is given by $\frac{GM}{\delta}$.

With tides, the gravity environment at any planetary body can be quite complicated, especially when multiple perturbers are considered and/or perturbers are treated as oblate masses. Even when only the gravity of a single point mass is considered, the tidal environment at the body of interest will be quite complicated and include many frequencies. This will mean that the strain, stress, and Love numbers from Sec. 3.1 and Sec. 2 can be determined at every individual frequency. Knowing this, then planetary mission data, for example the commonly measured k Love number, can then be interpreted at each particular frequency in the full spectrum of the tide to further constrain the interior structural prediction for the body. The frequency dependence is particularly important when including dissipative behavior in the body (Sec. 3.1.1). This section describes a unique and simple way to identify and isolate the specific terms associated with any particular frequency in the tidal spectrum. We will find specifically how the eccentricity, obliquity, mean motion, and the spin rate control the tide, and we will also see which frequencies they introduce.

In the most general form, the gravitational tidal potential due to a point source mass, M, a distance, δ, away is given by $\frac{GM}{\delta}$, where G is the gravitational constant. We require the potential's value at the body surface, R, and show the basic geometry for this in Fig. 3.1. The body center is located a distance d away from the source mass, and the angle between R and d is Γ. Using the cosine rule, we say that $\delta^2 = R^2 + d^2 - 2Rd\cos\Gamma$. This produces

$$\Psi = \frac{GM}{d}\left(1 + \left(\frac{R}{d}\right)^2 - 2\left(\frac{R}{d}\right)\cos\Gamma\right)^{-\frac{1}{2}}. \tag{3.22}$$

The bracketed term is the generating function for Legendre Polynomials. If $\frac{R}{d}$ is greater than

1, and it will be for planetary bodies in orbit, a series expansion about it shows that

$$\Psi = \sum_{\ell=0}^{\infty} \frac{GM}{d} \left(\frac{R}{d}\right)^{\ell} P_{\ell}\left(\cos\Gamma\right), \tag{3.23}$$

where P_ℓ represents the Legendre polynomial of degree ℓ. The gradient of this potential causes gravitational accelerations. At $\ell = 0$ the gradient produces no acceleration while at $\ell = 1$ the gradient produces the accelerations responsible for orbital motion, and so we drop these terms. The terms coming from $\ell \geq 2$ are the tidal deformation terms we are interested in.

We can use the dot product for the unit vectors for test location $\vec{R} = (1, \theta, \phi)$ and source location $\vec{d} = (1, \theta_s, \phi_s)$, to note that $\vec{R} \cdot \vec{d} = \cos\Gamma = \cos\theta\cos\theta_s + \sin\theta\sin\theta_s\cos(\phi - \phi_s)$. Now we convert Legendre polynomials into spherical harmonics and write

$$\Psi = \sum_{\ell=2}^{\infty} \sum_{m=-\ell}^{m=\ell} \frac{GM}{d} \left(\frac{R}{d}\right)^{\ell} \frac{4\pi}{2\ell+1} Y_{\ell,m}\left(\theta,\phi\right) Y^{*}_{\ell,m}\left(\theta_s,\phi_s\right). \tag{3.24}$$

At this point we have gotten the potential into the spherical harmonic form we need, and now we need to show that this can be written in a Fourier series as well. The only variables in this expression which can vary in time will be the orbital distance (d) as well as the source mass position (Γ or (θ_s, ϕ_s)). Next we show how a simple series of rotations provides us with the functions that describe the time dependence.

3.2.1 Time Variability

First we examine the time dependence of the orbital distance, d, because the geometry is simple. For this we just use the equation for an ellipse and say

$$d = \frac{a(1-e^2)}{1 + e\cos f} \tag{3.25}$$

where a and e are the orbital semi-major axis and eccentricity. The true anomaly f measures the orbital angular position from periapse. True anomaly is itself a function of time however it is complicated to solve, and must be treated with some type of iterative method. In particular we use Newton's method on Kepler's equation, which we will discuss in greater

detain in Sec. 3.2.1.1. For now, to reduce complication in finding the source mass position, we leave the true anomaly as f and will convert that into the time variable later.

In order to find the source mass position we will use a series of rotations about and translations of Cartesian coordinate axes. Once the position is identified in Cartesian, we then transform into spherical coordinates. In an attempt to keep this understandable, we present these rotations as an itemized list of operations. For a generic rotation matrix, $\forall_w(\xi)$, we would say we are rotating by an angle ξ about the w axis. We must make clear an important point. In many cases we rotate the coordinate system (and not the vector to the primary). If it is the coordinate system rotated, the rotation takes place in a negative sense relative to a convectional vector rotation.

Step 1: Satellite Position Relative to Primary

We start with the source mass at the origin, and align the path of the orbit to the xy-plane with periapse at true anomaly $f = 0$. The Cartesian position of the satellite in primary coordinates is

$\vec{x_1} = d\,[\cos f, \sin f, 0]$.

Step 2: Translate Coordinate System to Satellite

Without any rotation yet, we translate the coordinate system origin from the source to the center of the receiver body. In this body coordinate system, the primary can be found at

$\vec{x_2} = \vec{0} - \vec{x_1} = -d\,[\cos f, \sin f, 0]$.

Step 3: Rotate Coordinate System to Face Primary

Now we rotate the coordinate system about the vertical z-axis by 180° so that the x-axis points at the primary. In our case we say

$\vec{x_3} = \forall_z(-\pi)\vec{x_2} = d\,[\cos f, \sin f, 0]$.

Step 4: Add in Spin Obliquity

First we identify what we are calling the "longitude of obliquity" or perhaps the "obliquity phase" in the orbital plane. This ends up being more like the ascending node for the equator plane relative to the orbit plane. This node has some angular position ς, and we identify in Cartesian the unit vector associated with its location with $\zeta = [\cos\varsigma, \sin\varsigma, 0]$. We then rotate the coordinate system about the ζ axis by the obliquity, o. Notice that in this configuration, if $\zeta = 90^\circ$ exactly, then the northern hemisphere and the spin pole will point toward the primary. One can then imagine how a variable ς describes the precession of the spin axis about the orbit normal. A convenient aspect of this configuration, is that the average position of the source mass sits on the prime meridian and equator, regardless of obliquity phase. For this obliquity rotation we write

$$\begin{aligned}\vec{x_4} = \forall_\zeta(-o)\vec{x_3} = d\,[&\cos(f-\varsigma)\cos\varsigma - \cos o\sin(f-\varsigma)\sin\varsigma,\\ &\cos(f-\varsigma)\sin\varsigma + \cos o\sin(f-\varsigma)\cos\varsigma,\\ &-\sin o\sin(f-\varsigma)]\,.\end{aligned}$$

Step 5: Let the Body Spin

Now we need to let the coordinate system fixed to the body rotate in time t, at angular spin rate Ω about the z-axis. This is

$$\begin{aligned}\vec{x_5} = \forall_z(-\Omega t)\vec{x_4} = d\,[&\cos o\sin(f-\varsigma)\sin(\Omega t-\varsigma) + \cos(f-\varsigma)\cos(\Omega t-\varsigma),\\ &\cos o\sin(f-\varsigma)\cos(\Omega t-\varsigma) - \cos(f-\varsigma)\sin(\Omega t-\varsigma),\\ &-\sin o\sin(f-\varsigma)]\,.\end{aligned}$$

Step 6: Coordinate System Transform

Finally we convert into a spherical coordinate system. And with this transform we find

$$\begin{aligned}\vec{x_6} = (d,\theta_s,\phi_s) = \Big[\, &d,\\ &\cos^{-1}\left(-\sin o\sin(f-\varsigma)\right),\\ &\tan^{-1}\left(\frac{\cos o\sin(f-\varsigma)\cos(\Omega t-\varsigma) - \cos(f-\varsigma)\sin(\Omega t-\varsigma)}{\cos o\sin(f-\varsigma)\sin(\Omega t-\varsigma) + \cos(f-\varsigma)\cos(\Omega t-\varsigma)}\right)\Big]\,.\end{aligned} \tag{3.26}$$

We can then use the spherical position to find that the angle between the position and

primary vectors Γ can be written

$$\begin{aligned}\cos\Gamma &= \cos\theta\cos\theta_s + \sin\theta\sin\theta_s\cos(\phi-\phi_s)\\ &= -\cos(\theta)\sin(o)\sin(f-\varsigma)\\ &\quad + \sin(\theta)\sin^2\left(\frac{o}{2}\right)\cos(f+t\Omega+\phi-2\varsigma) + \sin(\theta)\cos^2\left(\frac{o}{2}\right)\cos(f-t\Omega-\phi). \quad (3.27)\end{aligned}$$

3.2.1.1 True Anomaly

The final bit to consider is the true anomaly, which is a function of time but not one that we can solve for analytically. We can use geometry, however, to relate the true anomaly to the eccentric anomaly, E, with

$$\tan\frac{f}{2} = \sqrt{\frac{1+e}{1-e}}\tan\frac{E}{2}. \quad (3.28)$$

So we can find f, if we know E. We can relate the eccentric anomaly to the mean anomaly (and time with $M = nt$ has zero defined at periapse) by noting Kepler's law finds an orbit sweeps out equal areas in equal time. Comparing the area swept out in the elliptical orbit and the area swept by an imaginary circular orbit we find Kepler's equation,

$$M = E - e\ sinE \quad (3.29)$$

It is Kepler's equation which does not have analytic solutions though. So for this we need to use a numerical method, in particular Newton's method, which we can use to find the root for $h(E) = E - e\ sinE - nt$. Newton's method gives successively better approximations for the E that is the root of h with each iteration of $E_{n+1} = E_n - \frac{h(E_n)}{h'(E_n)}$. If e is small, we can say $E_0 = M = nt$ as a pretty good guess to approximately satisfy $h = 0$. In general, only two or three iterations are necessary for the orbits we will consider. As it turns out, the true anomaly is a complicated function of time and eccentricity that we don't want to really display on the page, but the expression is manageable with a series expansion in eccentricity. We will end up using a series expansion in e as a final step, however, so for now and for redundancy we always take two more iterations in E_n than the order of the expansion in e.

3.2.2 Potential Spectrum

We now have expressions to track the position of the primary in the geographic coordinate system attached to the deforming body (Eqs. 3.25 and 3.26). We apply these into the potential expression in Eq. 3.24. Finally, we take this expression and perform a series expansion in eccentricity on it. Once expanded, the potential then takes a general form

$$\Psi = \sum_{\omega} \Upsilon \ \Theta_{\omega} Y_{\ell,m}(\theta, \phi) \ e^{\mathrm{i}\omega t}, \tag{3.30}$$

where Υ is some factor common to all the terms, which depends on the degree of the potential and the order of the eccentricity expansion and the sum is over every frequency present. Which frequencies are present is determined, in part, by 1) the degree (ℓ) of the potential , 2) The order ($\mathcal{O}_e$) to which the expansion in eccentricity is carried out, 3) the difference in orbit and spin rates, and 4) the presence of spin obliquity. In general, assuming asynchronous rotation and an oblique spin pole, the maximum number of frequencies we find goes as $(2\ell + 1)(2\ell + 1 + 2\mathcal{O}_e)$ for any specific degree. Many of these frequencies see a zero valued Θ_{ω} coefficient if the spin pole is non oblique (we will see this specifically in a moment), and so in this case many of the frequencies collapse away. In addition, for some integer ratios of spin and orbit rates (describing particular spin-orbit resonances) we see further collapse of the frequencies. The frequencies always take the form of $\omega = pn - m\Omega$, where m is the same as the order of the spherical harmonic and p is an integer coefficient in the range $-(\ell + \mathcal{O}_e)$ to $(\ell + \mathcal{O}_e)$. For frequency containing odd p, the frequency coefficients Θ_{ω} will contain terms with odd powers of eccentricity only $(e, e^3, e^5, ...)$, while the even p terms have the even eccentricity powers $(e^0, e^2, e^4, ...)$. This does mean that for vanishing eccentricity all of the terms for frequencies with odd p go to zero. In addition, we recognize that this expansion contains both the positive and negative frequencies we expect from any Fourier representation. As a result if we select a term at a particular frequency, say $\Psi(\omega)$, we note that $\Psi(-\omega) = \Psi^*(\omega)$. We end up taking the absolute value of each term to determine the elastic energy density (see Sec. 3.1), and the absolute value of any function is, of course, the absolute value of its conjugate.

We next re-write the expanded potential as an explicit sum. We drop the summation in

ℓ in our notation, as we will be selecting one term at a time, and therefore one ℓ at a time. We write,

$$\Psi = \sum_{m=-\ell}^{\ell} \sum_{p=-(\ell+\mathcal{O}_e)}^{(\ell+\mathcal{O}_e)} \Upsilon \; \Theta_{(pn-m\Omega)} Y_{\ell,m}\left(\theta,\phi\right) \; e^{\mathrm{i}(pn-m\Omega)t}, \tag{3.31}$$

For degree $\ell = 2$ and $\mathcal{O}_e = 1$, we find that $\Upsilon = \frac{GMR^2}{a^3}\sqrt{\frac{3\pi}{10}}$. We also present here, for $\ell = 2$ and $\mathcal{O}_e = 1$, the complete set of Θ_ω coefficient for all thirty-five tidal frequencies found in a generic orbit. One will notice the close similarity between a frequency's coefficient and that of its negative's frequency. In effect the difference here is just that any term in which ς is present switches signs with the frequency. Also, for every term belonging to a frequency with $\pm 3n$ is exactly $\frac{7}{2}e$ times the term for the $\pm 2n$ frequency. All of this leads us to believe that these coefficients had be further consolidated somehow with the p and m indexes. However, for now and for completeness we present the coefficients explicitly.

$$\begin{aligned}
\Theta_{-3n-2\Omega} &= \frac{7}{2}e \; \mathrm{e}^{4\mathrm{i}\varsigma} \sin^4\left(\frac{o}{2}\right), \\
\Theta_{-2n-2\Omega} &= \mathrm{e}^{4\mathrm{i}\varsigma} \sin^4\left(\frac{o}{2}\right), \\
\Theta_{-n-2\Omega} &= \frac{1}{4}e \; \mathrm{e}^{2\mathrm{i}\varsigma} \sin^2\left(\frac{o}{2}\right)\left(6(\cos(o)+1) + \mathrm{e}^{2\mathrm{i}\varsigma}(\cos(o)-1)\right), \\
\Theta_{0n-2\Omega} &= \frac{1}{2}\mathrm{e}^{2\mathrm{i}\varsigma} \sin^2(o), \\
\Theta_{n-2\Omega} &= \frac{1}{4}e\left(-2\cos^4\left(\frac{o}{2}\right) + 3\mathrm{e}^{2\mathrm{i}\varsigma}\sin^2(o)\right), \\
\Theta_{2n-2\Omega} &= \cos^4\left(\frac{o}{2}\right), \\
\Theta_{3n-2\Omega} &= \frac{7}{2}e\cos^4\left(\frac{o}{2}\right)
\end{aligned} \tag{3.32}$$

$$
\begin{aligned}
\Theta_{-3n-\Omega} &= -\frac{7}{2}\mathrm{i}e\ \mathrm{e}^{3\mathrm{i}\varsigma}\sin^2\left(\frac{o}{2}\right)\sin(o),\\
\Theta_{-2n-\Omega} &= -\mathrm{i}\ \mathrm{e}^{3\mathrm{i}\varsigma}\sin^2\left(\frac{o}{2}\right)\sin(o),\\
\Theta_{-n-\Omega} &= -\frac{1}{4}\mathrm{i}e\ \mathrm{e}^{\mathrm{i}\varsigma}\sin(o)\left(6\cos(o)+\mathrm{e}^{2\mathrm{i}\varsigma}(\cos(o)-1)\right),\\
\Theta_{0n-\Omega} &= -\mathrm{i}\ \mathrm{e}^{i\varsigma}\sin(o)\cos(o),\\
\Theta_{n-\Omega} &= \frac{1}{4}e\sin(o)((5\cos(o)-1)\sin(\varsigma)-\mathrm{i}(7\cos(o)+1)\cos(\varsigma)),\\
\Theta_{2n-\Omega} &= 2\mathrm{i}\ \mathrm{e}^{-i\varsigma}\sin\left(\frac{o}{2}\right)\cos^3\left(\frac{o}{2}\right),\\
\Theta_{3n-\Omega} &= 7\mathrm{i}e\ \mathrm{e}^{-i\varsigma}e\sin\left(\frac{o}{2}\right)\cos^3\left(\frac{o}{2}\right)
\end{aligned}
\tag{3.33}
$$

$$
\begin{aligned}
\Theta_{-3n} &= \frac{1}{4}(-7)\sqrt{\frac{3}{2}}e\ \mathrm{e}^{2\mathrm{i}\varsigma}\sin^2(o),\\
\Theta_{-2n} &= -\frac{1}{2}\sqrt{\frac{3}{2}}\ \mathrm{e}^{2\mathrm{i}\varsigma}\sin^2(o),\\
\Theta_{-n} &= \frac{1}{4}\sqrt{\frac{3}{2}}e\left(\ \mathrm{e}^{2\mathrm{i}\varsigma}\sin^2(o)-3\cos(2o)-1\right),\\
\Theta_{0n} &= -\frac{3\cos(2o)+1}{2\sqrt{6}},\\
\Theta_{n} &= \frac{1}{4}\sqrt{\frac{3}{2}}e\left(\ \mathrm{e}^{-2\mathrm{i}\varsigma}\sin^2(o)-3\cos(2o)-1\right),\\
\Theta_{2n} &= -\frac{1}{2}\sqrt{\frac{3}{2}}\ \mathrm{e}^{-2\mathrm{i}\varsigma}\sin^2(o),\\
\Theta_{3n} &= \frac{1}{4}(-7)\sqrt{\frac{3}{2}}e\ \mathrm{e}^{-2\mathrm{i}\varsigma}\sin^2(o)
\end{aligned}
\tag{3.34}
$$

$$
\begin{aligned}
\Theta_{-3n+\Omega} &= 7\mathrm{i}e\ \mathrm{e}^{i\varsigma}e\sin\left(\frac{o}{2}\right)\cos^3\left(\frac{o}{2}\right),\\
\Theta_{-2n+\Omega} &= 2\mathrm{i}\ \mathrm{e}^{i\varsigma}\sin\left(\frac{o}{2}\right)\cos^3\left(\frac{o}{2}\right),\\
\Theta_{-n+\Omega} &= \frac{1}{4}e\sin(o)(-(5\cos(o)-1)\sin(\varsigma)-\mathrm{i}(7\cos(o)+1)\cos(\varsigma)),\\
\Theta_{0n+\Omega} &= -\mathrm{i}\ \mathrm{e}^{-i\varsigma}\sin(o)\cos(o),\\
\Theta_{n+\Omega} &= -\frac{1}{4}\mathrm{i}e\ \mathrm{e}^{-\mathrm{i}\varsigma}\sin(o)\left(6\cos(o)+\mathrm{e}^{-2\mathrm{i}\varsigma}(\cos(o)-1)\right),\\
\Theta_{2n+\Omega} &= -\mathrm{i}\ \mathrm{e}^{-3\mathrm{i}\varsigma}\sin^2\left(\frac{o}{2}\right)\sin(o),\\
\Theta_{3n+\Omega} &= -\frac{7}{2}\mathrm{i}e\ \mathrm{e}^{-3\mathrm{i}\varsigma}\sin^2\left(\frac{o}{2}\right)\sin(o)
\end{aligned}
\tag{3.35}
$$

$$
\begin{aligned}
\Theta_{-3n+2\Omega} &= \frac{7}{2}e\cos^4\left(\frac{o}{2}\right), \\
\Theta_{-2n+2\Omega} &= \cos^4\left(\frac{o}{2}\right), \\
\Theta_{-n+2\Omega} &= \frac{1}{4}e\left(-2\cos^4\left(\frac{o}{2}\right) + 3\mathrm{e}^{-2\mathrm{i}\varsigma}\sin^2(o)\right), \\
\Theta_{0n+2\Omega} &= \frac{1}{2}\mathrm{e}^{-2\mathrm{i}\varsigma}\sin^2(o), \\
\Theta_{n+2\Omega} &= \frac{1}{4}e\ \mathrm{e}^{-2\mathrm{i}\varsigma}\sin^2\left(\frac{o}{2}\right)\left(6(\cos(o)+1) + \mathrm{e}^{-2\mathrm{i}\varsigma}(\cos(o)-1)\right), \\
\Theta_{2n+2\Omega} &= \mathrm{e}^{-4\mathrm{i}\varsigma}\sin^4\left(\frac{o}{2}\right), \\
\Theta_{3n+2\Omega} &= \frac{7}{2}e\ \mathrm{e}^{-4\mathrm{i}\varsigma}\sin^4\left(\frac{o}{2}\right)
\end{aligned}
\tag{3.36}
$$

3.3 Volume Integrals

If one is interested in the full three dimensional spatially resolved energy density within a body, selecting the potential of Sec. 3.2.2 at a particular frequency and applying this potential into the energy expression in Eq. 3.21 will produce the analytic expressions for this. Often, however, a study will require the total heat generated within some body. Generally, when someone wants this they will use the classic expression for tidal eating that we gave in Eq. 3.1. In this section we compare the classic expression to ours. Here we will show what assumptions must be made in order to recover the classic expression. In doing so, we will describe the scenarios for which extra tidal heat is predicted with our model. In particular we find extra heat at a variety of frequencies for bodies that rotate not-synchronously and or bodies with significant obliquity. To start, we integrate Eq. 3.21 in volume to find the tidal heating rate (in watts). Each term in the integration is separable into radial and angular

integrals such that

$$\begin{aligned}
\dot{Q}_{tide} &= \int \dot{\Xi}_{inc,diss}\, dV \\
&= -2\omega \int Im[\widetilde{\mu}]\,(pf_1 rf_1 + pf_2 rf_2 + pf_3 rf_3)\, dV \\
&= -2\omega \left[\int pf_1 \sin(\theta) d\theta d\phi \int Im[\widetilde{\mu}]\; rf_1\; r^2 dr \right. \\
&\qquad + \int pf_2 \sin(\theta) d\theta d\phi \int Im[\widetilde{\mu}]\; rf_2\; r^2 dr \\
&\qquad \left. + \int pf_3 \sin(\theta) d\theta d\phi \int Im[\widetilde{\mu}]\; rf_3\; r^2 dr \right].
\end{aligned} \tag{3.37}$$

Notice that $Im[\widetilde{\mu}]$ sits inside the radial integrals because multi-layered bodies should see it vary with radius. The integrals for rf will depend only on the structure of the body, and the integrals for pf will depend on the tide. We start with the pf integrals as they are more general and can be applied for any planetary object, where the rf integrals should require some imposed structure.

3.3.1 pf Integrals

In this section the angular integral for each pf function in Eq. 3.18 is given. Because of the orthogonality of spherical harmonics the integrals are actually quick to do. The first, pf_1, is just the absolute value squared for the potential. Even when an arbitrary potential at some frequency is compromised of various degrees and orders of spherical harmonics, orthogonality of these functions assures us that $\int Y_{\ell,m} Y^*_{\ell_2,m_2} \sin(\theta) d\theta d\phi = 1$ only when $\ell = \ell_2$ and $m = m_2$, and zero otherwise. Because of this we can say that for whatever frequency ω_i,

$$\int pf_1 \sin(\theta) d\theta d\phi = \int \Psi_{\omega_i} \Psi^*_{\omega_i} \sin(\theta) d\theta d\phi = \Upsilon^2\; \Theta_{\omega_i} \Theta^*_{\omega_i}. \tag{3.38}$$

While we have not been able to prove it yet, we can also say that for (at least, but probably all) degree $\ell = 3$ and under we are confident that

$$\begin{aligned}\int pf_2 \sin(\theta) d\theta d\phi &= \frac{\ell(\ell+1)}{2} \int pf_1 \sin(\theta) d\theta d\phi \\ &= \frac{\ell(\ell+1)}{2} \Upsilon^2 \ \Theta_{\omega_i} \Theta^*_{\omega_i}\end{aligned}$$

$$\begin{aligned}\int pf_3 \sin(\theta) d\theta d\phi &= -\ell(\ell+1) \int pf_1 \sin(\theta) d\theta d\phi \\ &= -\ell(\ell+1) \Upsilon^2 \ \Theta_{\omega_i} \Theta^*_{\omega_i}. \end{aligned} \tag{3.39}$$

This indicates that we are probably missing some type of simplification which can reduce the pf functions even further to produce a more elegant expression. For now, we simply acknowledge this and leave it for the future.

Recall that the number of frequencies found depends on the degree of the potential and of the eccentricity expansion. In Sec. 3.2.2 we presented the coefficients for the thirty-five frequencies found for $\ell = 2$ and $\mathcal{O}_e = 1$. Now, when the square of absolute value of each of these coefficients is considered, they are surely real and we can examine the relative magnitudes of the coefficients as a function of obliquity. For ease on the eyes it is helpful to eliminate the duplicate negative frequencies (we will be sure to include their contribution in calculating heat - but there is no need to repeat them on paper). We note that $\Upsilon^2 = \frac{3\pi G^2 M^2 R^4}{10 a^6}$ for our chosen orders and we plot the remaining 18 distinct coefficients which correspond to the particular frequencies.

One can see from Fig. 3.2 that the simple $\sin^2 o$ dependence (also included as in the figure in the dotted curve) that the typical tidal heating result can not capture all of the potential heat generated at every frequency. Of course, many of these curves will superpose under specific orbital and rotational conditions as the frequencies collapse, for synchronous rotation for example. Even with this, however, the simple picture of tidal heating is just not sufficient in a general context.

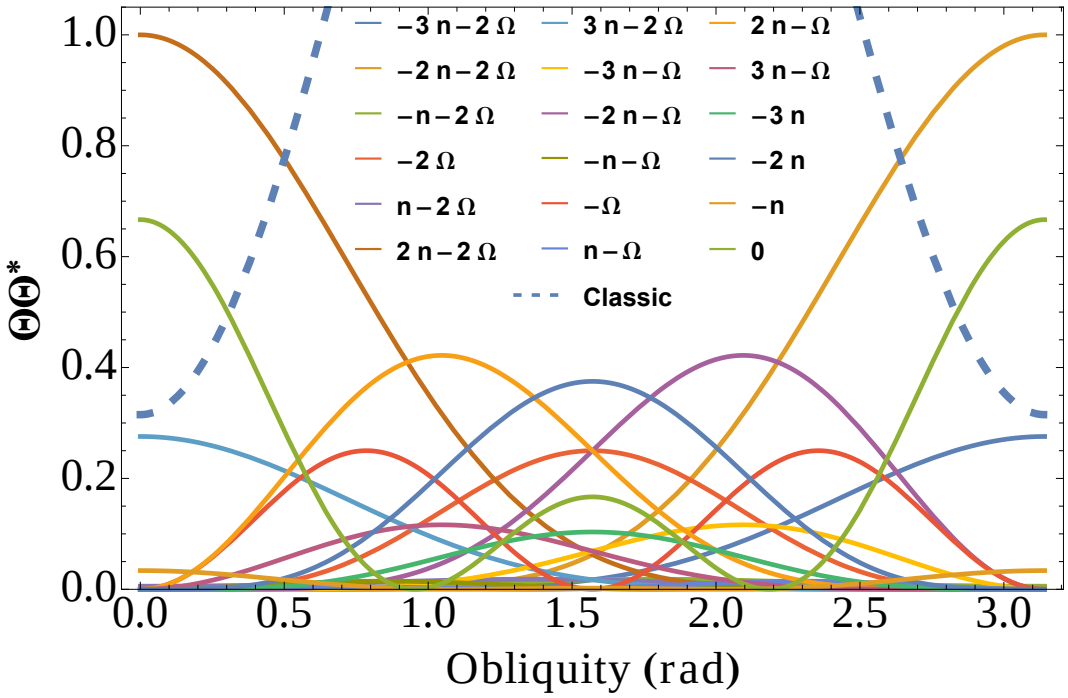

Figure 3.2: The value of all the $\Theta_{\omega_i}\Theta^*_{\omega_i}$ coefficients as a function of obliquity. Here arbitrary values of $e = 0.15$ and $\varsigma = \pi/2$ have been selected to give those terms relatively significant values. Each curve represents the influence from a distinct tidal frequency. The dashed curve shows the conventional prediction.

3.3.2 rf Integrals

Once we've completed the pf integrals, the three integrals in radius collapse into one and we have

$$\begin{aligned}\dot{Q}_{tide} &= -2\omega \int Im[\widetilde{\mu}]\,(pf_1 rf_1 + pf_2 rf_2 + pf_3 rf_3)\,dV \\ &= -2\omega\ \Upsilon^2\ \Theta_{\omega_i}\Theta^*_{\omega_i} \int Im[\widetilde{\mu}]\left(rf_1 + \frac{\ell(\ell+1)}{2} rf_2 - \ell(\ell+1) rf_3\right) r^2 dr. \end{aligned} \tag{3.40}$$

Every single factor in this expression, including the integrand, is frequency dependent. The integrand, in particular, is a body specific function which depends on the internal structure. Until we begin examining cases we can't really say much more here. As a teaser, however, we will hypothesize here that there is a relationship between this integrand and the imaginary part of the k Love number given by

$$\int Im[\widetilde{\mu}]\left(rf_1 + \frac{\ell(\ell+1)}{2} rf_2 - \ell(\ell+1) rf_3\right) r^2 dr = \frac{5R}{8\pi G} k_I. \tag{3.41}$$

We expect that there is some type of way to prove this using the definitions of the y-functions and possibly integration by parts. After great effort we still have not found it, and leave this for the future. We can confirm analytically that for, at least, homogeneous bodies the expression is valid. Using numerical evaluations for complicated multi-layered models, we have also determined this equality, however an analytic proof would be more satisfying. If Eq. 3.41 is satisfied, in general, then our tidal heating rate becomes,

$$\dot{Q}_{tide} = -2\omega \ \Upsilon^2 \ \Theta_\omega \Theta^*_\omega \frac{5R}{8\pi G} k_{I_\omega}. \tag{3.42}$$

In following section we will the circumstances for which our tidal heating treatment and the classic tidal heating equation (Eq. 3.1) are equivalent, and those where our results diverge.

3.4 Case Studies

In this section we choose a set of specific bodies, or body types, to highlight a particular component of this tidal heating model. First, we examine the case of a general synchronous rotator. This allows us to see how in even a very common solar system body type, the various frequencies are important to consider. We compare this to the classic tidal heating expression, and infer a relationship between the k Love number and the radial integrand of rf functions. Then we consider the example of Venus, to look at an interesting obliquity case. Finally we consider Mercury, for which a $3:2$ spin-orbit resonance produces a unique array of heating frequencies.

3.4.1 Synchronous Rotators

Gravitational torques on a rapidly rotating body's tidal bulge tend to slow the spin of that body. Because of this, the natural dynamical outcome sees a body's spin rate synchronize to its mean orbital rate. And because of this we see synchronous rotation in most of the satellites in our solar system, and even our own moon, for example. When we set the spin rate equal to the mean motion ($\Omega = n$), the frequencies in the tidal spectrum collapse to multiples of n. In particular the frequencies we find are $\omega = n,\ 2n,\ 3n,\ 4n$, and $5n$ plus the

negative frequencies as well as the zero frequency. We see relative magnitudes of these five frequencies in Fig. 3.3, for zero eccentricity (left panel) and for the very high eccentricity of $e = 0.15$ (right panel). In both cases we also show in the dotted line, what the classic tidal heating theory would predict for $\Theta\Theta^*$ (we also explain, below, how we determined this). The main point of these plots is to show that for a synchronous body with almost any obliquity, the higher frequencies must be analyzed to capture the behavior. At very low obliquity, however, the $\omega = n$ frequency accurately describes the complete tidal contribution. This give us confidence that for use in our Galilean heating models (see Sec. 4), where we assume no obliquity at all, the classic approach will be sufficient to track all of the tidal heat.

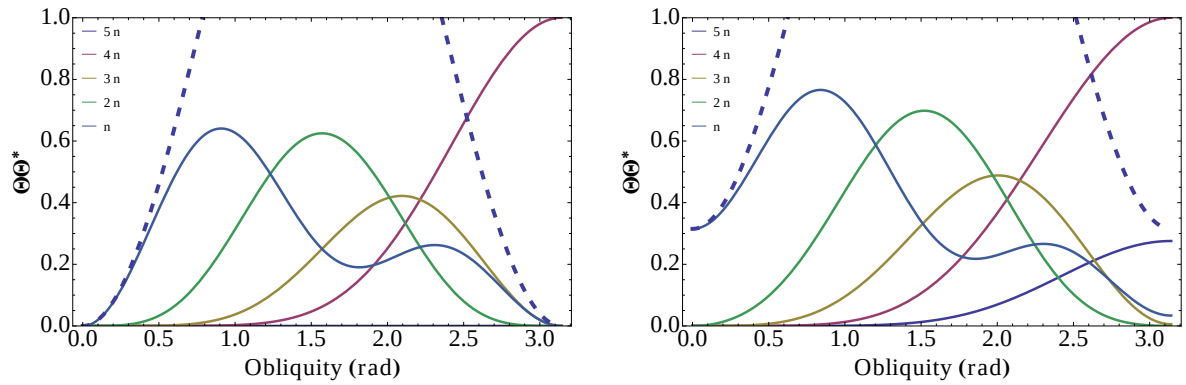

Figure 3.3: The $\Theta\Theta^*$ tidal heating coefficients for synchronous rotators. Each curve shows one of the five distinct frequencies in this tide, showing the relative magnitudes of the different frequencies at various obliquity values. The dashed curve gives the classic result. The left panel gives the zero eccentricity scenario, and the right panel shows an arbitrary eccentricity of $e = 0.15$.

3.4.1.1 Compared to Classic

We briefly return to the classic tidal heating form given by Eq. 3.1. First we notice that the terms in e^2 and in $\sin^2 o$ are separate, and there are no cross terms. We take the $\Theta\Theta^*$ coefficients for the five frequencies we found for a synchronous rotator, and we set the obliquity equal to zero. This isolates the eccentricity only terms, which it turns out there is only one of and it is at the mean motion frequency $\omega = n$. In this case of synchronous with no obliquity we find $\Theta\Theta^*_n = 14e^2$. Similarly, we take the same five coefficients and instead set

the eccentricity to zero, to isolate the obliquity only terms. To emulate the classic expressions small angle dependence we take a series expansion in $\sin o$ on the coefficients. Here we find that again only the $\omega = n$ coefficient is non zero valued and is $\Theta\Theta^*_n = 2\sin^2 o$. We sum these and call it the classic coefficient, and note that this coefficient implicitly assumes synchronous rotation, small e and $\sin o \approx o$, and that $\omega = n$. It is,

$$\Theta\Theta^*_{classic} = 2(7e^2 + \sin^2 o). \tag{3.43}$$

We use this coefficient and $\Upsilon^2 = \frac{3\pi G^2 M^2 R^4}{10a^6}$ in Eq. 3.40 and we come to

$$\dot{Q}_{tide} = -2n \ \frac{3\pi G^2 M^2 R^4}{10a^6} \ 4(7e^2 + \sin^2 o) \ \int Im[\widetilde{\mu}] \left(r f_1 + \frac{\ell(\ell+1)}{2} r f_2 - \ell(\ell+1) r f_3 \right) r^2 dr. \tag{3.44}$$

Where it is extremely important to highlight that we have doubled the coefficient $2\Theta\Theta^*_{classic} = 4(7e^2 + \sin^2 o)$, because we need to account for the negative frequency for which the contribution is exactly equivalent. We employ $\frac{GM}{a^3} = n^2$, and equate to Eq. 3.1 and have

$$- \ \frac{12\pi n^5 R^4}{5} \ (7e^2 + \sin^2 o) \ \int Im[\widetilde{\mu}] \left(r f_1 + \frac{\ell(\ell+1)}{2} r f_2 - \ell(\ell+1) r f_3 \right) r^2 dr = \tag{3.45}$$

$$- \frac{3}{2} \frac{n^5 R^5}{G} k_I \left(7e^2 + \sin^2 o\right). \tag{3.46}$$

We solve this for the integral, and get

$$\int Im[\widetilde{\mu}] \left(r f_1 + \frac{\ell(\ell+1)}{2} r f_2 - \ell(\ell+1) r f_3 \right) r^2 dr = \frac{5R}{8\pi G} k_I, \tag{3.47}$$

which we hinted at in Sec. 3.3.2. In fact, the only factors in this containing imaginary terms are μ and k, and so this should be valid for the complete complex values as well, not just the imaginary piece as the equation above indicate. We have confirmed this analytically for homogeneous bodies, for which k, y_1, and y_2 are simple functions (see Sec. 2.3), however have yet to do so analytically in a general way. We have, however, calculated the Love numbers for complicated and specific structures and compared it with the integral expression above. For the random general numeric cases we chose, every time the equivalence approximately held. We expect any difference is just numerical round off error, and the expression can be analytically proven for a general structure. Assuming this relationship is valid, we now

write the complete tidal heating expression for a synchronous rotator as a sum of all of the contributions from the five frequencies in its tide. This is,

$$\dot{Q}_{tide} = -\frac{3n^5R^5}{4G}\ \left(\Theta\Theta^*_n k_{I_n} + 2\Theta\Theta^*_{2n} k_{I_{2n}} + 3\Theta\Theta^*_{3n} k_{I_{3n}} + 4\Theta\Theta^*_{4n} k_{I_{4n}} + 5\Theta\Theta^*_{5n} k_{I_{5n}}\right), \quad (3.48)$$

where we have already multiplied by two, to take care of the negative frequencies.

3.4.2 Venus

We use Venus as a dramatic example of where our model will diverge from the classic tidal heating model. Venus is in an awkward spin state for two reasons. First, the body spins in a retrograde sense, with an obliquity of 177.36° relative to its orbit normal about our star (It is important to note that we consider spin rates positive always. A retrograde rotator will just have obliquity $o > 90°$). The other reason Venus has an interesting spin is because its rotational period ($T_\Omega = \frac{2\pi}{\Omega} \approx 243\ days$) is longer than its orbital period ($T_n = \frac{2\pi}{n} \approx 224.7\ days$). Generally, the gravitational torque on a rapidly rotating body's tidal bulge will tend to draw that bulge (which leads the planet-satellite line due to inertia) back into alignment with the sub-primary point. This torque will spin down the planet until the body reaches the synchronous spin state, at where the average torque over an orbit vanishes leaving only librational behavior in the spin. On Venus, the atmosphere is heated from solar radiation causing a thermal expansion. It has been hypothesized that the thick atmosphere heated as such causes pressure variations at the surface that can produce an additional atmospheric torque, which balances the gravitational torque and resulted in Venus spinning down to the slower than synchronous rate observed (for example Ingersol and Dobrovolskis (1978) [10]). Regardless of how Venus got its weird spin, the configuration presents us with an interesting example.

In order to consider Venus, we are using the parameters for eccentricity, semi-major axis, and mean radius to be $e = 0.0068$, $a = 1.08 \times 10^{11}\ m$, and $R = 6.05 \times 10^6\ m$ respectively. We use $G = 6.67 \times 10^{-11}\ m^3\ kg^{-1}\ s^{-2}$ and the solar mass $M = 1.99 \times 10^{30}\ kg$. Returning to Fig. 3.2, we see that for close to $o = \pi$, where we find Venus's obliquity, there are two frequencies which produce relatively large tidal responses. It is hard to tell by eye, perhaps,

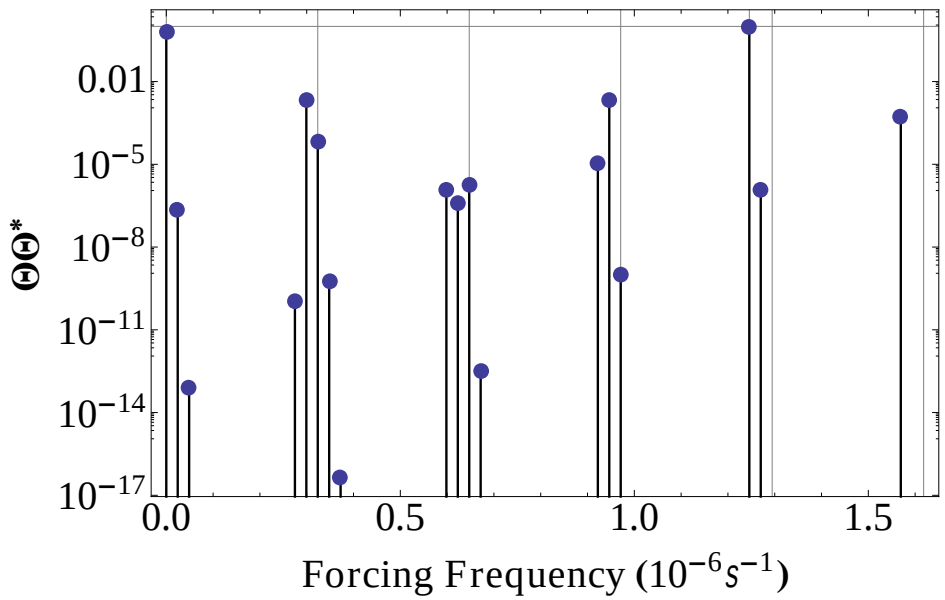

Figure 3.4: Tidal heating coefficient spectrum for Venus. Vertical grid lines designate integer multiples of the mean motion. The maximum tidal response occurs at the frequency $\pm 2(n + \Omega)$.

but the green curve here is the $\omega = 0$ frequency contribution, and so it produces no tidal heating. The orange curve, of an even greater magnitude describes the $\omega = \pm 2(n + \Omega)$ frequency. From this alone we expect that we will find the most tidal heating in Venus at that frequency.

In Fig. 3.4 we show the full spectrum of tidal heating in Venus. Vertical grid lines show integer multiples of the Venusian mean motion. Had Venus been a synchronous rotator, all of the tidal components would be found at specifically these frequency values. We find spectral splitting at these lines, due to Venus's not-synchronous rotation. The gaps between adjacent spectral lines are exactly a frequency distance of $n - \Omega$ away, because in Venus's case that difference is small. For greater values of this difference, alternate sets of split lines can sometimes merge and cross, and so assuming "gaps between adjacent spectral lines are exactly a frequency distance of $n - \Omega$" in a general way can be dangerous. In any event, we see the two greatest magnitude influences at zero frequency and also, as expected, at $4n - 2(n - \Omega) = 2n + 2\Omega$. In looking at the spectral figures, like Fig. 3.4, it is important to remember that the tidal heating expression in Eq. 3.42 contains a factor of ω. This

completely eliminates the zero frequency contribution (consistent with the notion that the time variable tidal flexing is what causes the heating), leaving $2n+2\Omega$ remaining as the next most significant, while every other spectral magnitude is at least three orders of magnitude less. Another point of caution is that we must also recognize that the Love number k_I is strongly frequency dependent. It is quite possible that the Love number at one frequency be orders of magnitude smaller at another. A detailed structure model would be required to determine Venus's Love number, and we do not want to get into that for this work. Sec. 2.2 provides a detailed description of how a Love number depends on frequency in general. We will, however, compare the classic tidal heating, evaluated at Venus, to our model of tidal heating. In doing so we find that $\dot{Q}_{classic} = -1.58 \times 10^9 \ k_I(n) \ W$ and our $\dot{Q}_{tide} = -1.24 \times 10^{12} \ k_I(2n + 2\Omega) \ W$. This difference of roughly three orders of magnitude will surely be modified when the Love numbers are applied, however this example does a good job of showing how to consider tidal heating at every frequency, and why one might want to.

3.4.3 Mercury

We look at Mercury, with the idea that Fig. 3.2 suggests that bodies with low obliquity and high eccentricity should see their largest magnitude tidal heating in the $\omega = \pm(2n - 2\Omega)$, $\pm(3n - 2\Omega)$, and 0 frequencies. Mercury is in a unique (to our solar system) spin-orbit resonance in which for every two orbits, Mercury will rotate about its spin axis three times, that is $\Omega = \frac{3}{2}n$. Because of this, the frequencies we expect peaks at collapse with $\omega = \pm(2n - 2\Omega) = \pm n$ and $\omega = \pm(3n - 2\Omega) = 0$. Notice that this eliminates the tidal heating contribution from the only frequency out of the three we predicted to be important that strongly depends on eccentricity! This is an important point as tidal heating tends to pull energy out of a system while maintaining angular momentum. In a simple two body problem this dynamical end state sees vanishing eccentricity, which drives eccentric tidal heating to zero. It may be the case that we have stumbled on to an analogous scenario, where a spin-orbit resonance allows for a non-zero eccentricity which produces a static tide and an eccentric tidal heating of zero. This is another interesting task we reserve for future

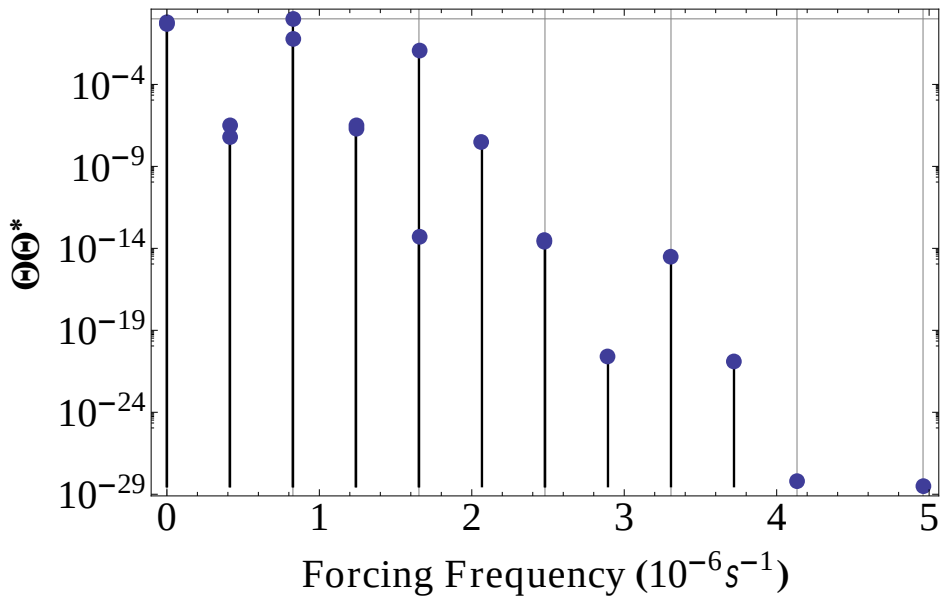

Figure 3.5: Tidal heating coefficient spectrum for Mercury. Vertical grid lines designate integer multiples of the mean motion. The maximum tidal response occurs at the frequency $\pm n$ with significant response at $\pm 2n$.

exploration. We also must point out that Mercury has a very large eccentricity of $e = 0.205$. It is likely the case that our series expansion in e, only out to first order, is not sufficient to accurately describe the motion of Mercury. At this point, we have not tabulated the tidal heating coefficients that a second order eccentricity expansion would produce. In the future a more rigorous study of the Mercurian tide should be conducted, however, we use the linear expansion in this work purely to demonstrate the spectral behavior in a spin-orbit resonance.

For Mercury, the remaining parameters we need are $o = 0.034°$, $n = \frac{2\pi}{87.97\ days}$, $a = 5.79 \times 10^{10}\ m$, and $R = 2.44 \times 10^{6}\ m$. This produces the tidal spectrum in Fig. 3.5. Again, vertical grid lines mark the integer multiples of the mean motion. Because of the spin-orbit resonance, all of the present frequencies in the spectrum are half integer multiples of n. As expected we find the most significant contribution from the $\omega = \pm(2n - 2\Omega) = \pm n$ frequency, demonstrating that Mercury's tidal heating is dominated by terms that are independent of eccentricity (even at the very large eccentricity). An unexpected result is that two additional frequencies show significance, though are reduced by one or two orders of magnitude. They

are the true $\omega = \pm n$ frequency and also the $\omega = \pm 2n$ frequency. Both are eccentricity dependent, and can be seen as the next two greatest magnitude frequencies in Fig. 3.2 though a log plot might make them easier to spot. We use the frequency dependent Love number to write our prediction for Mercury's tidal heating rate as $\dot{Q}_{tide} = -3.99 \times 10^{11}\ k_I(n)\ W - 7.93 \times 10^{9}\ k_I(2n)\ W$, where we have already associated the two terms found at $\pm n$. Which of these two terms is most significant will surely depend on k_I. The classic result would find $\dot{Q}_{classic} = -2.22 \times 10^{11}\ k_I(n)\ W$, which in all structural scenarios is less than our prediction by about a factor of two. This difference seems relatively small, and possibly insignificant at first glance, but our model is predicting that most of the heat is generated in obliquity tides, while the classic model predicts the heat was generated from the large eccentricity tide. The near equivalence is merely a coincidence.

Conclusion

We have presented a new model for tidal heating that considers every frequency in the tidal spectrum. We show how the classically described tidal heating model predicts heating only for synchronous rotators in low eccentricity and obliquity states, and only that heat which is delivered in the orbital/rotational frequency term of the tide. We bridge the two models to show how our model collapses to the classic model under these assumptions.

With our more general model, we show the relative tidal heating coefficients for all eighteen distinct frequencies in the degree two tide (linearized in eccentricity) of any body. For bodies with finite obliquity, as we show with Venus, the orbital frequency potentially contains orders of magnitude less energy than higher frequencies. Ultimately, this will depend on the internal structure of Venus and its k Love number. In examining the tidal heating in consideration of the $3:2$ spin orbit resonance at Mercury, we have identified an interesting scenario in which, even though Mercury's eccentricity is quite high, the magnitude of heat delivered from eccentricity tides is much less than the heat delivered from obliquity tides.

The examples in Venus and Mercury highlight how that by just considering the only two planets closer to the Sun than Earth, that our model predicts much different heating

rates and sources than conventional tidal heating models might. A particularly interesting application for our type of tidal heating model could be in exoplanetary systems, where all sorts of tightly packed and resonant systems are observed (the TRAPPIST-1 system for example [8]). All of these findings are interesting however tangential to our main purpose, which is determining tidal heating in Io and in Europa. As it turns out, being synchronous rotators with low obliquity, the classic tidal heating model is sufficient for the Galilean satellite's purpose. Nevertheless, we thought it was important to share our findings about how tidal heating works in a more general way.

CHAPTER 4

Heat Transfer

Introduction

A variable gravity environment, due to an eccentric orbit or an oblique or not-synchronous spin, causes tidal heat generation in a planetary body. In the case of the Galilean satellites, adjacent bodies are synchronized to two sets of 2 : 1 mean motion resonances which force the eccentricities of the orbits, pumping them up in opposition to tidal dissipation's reductive influence. This causes maintained and oscillatory tidal heating inputs which affect a satellite's heat budget and can cause internal evolution of structure. For example, if more heat is generated within Io than can escape to space, then Io's internal temperature will increase. This drives the convective heat flux of the interior up, and Io's conductive lid must thin to increase its heat flux to space. This tends to move the heat balance toward equilibrium. Dissipated tidal heat should pull energy out of Io's orbit, however, causing decreased tidal heat production and a thickening lithosphere. A similar mechanism likely operates at Europa, thinning and thickening Europa's ice shell. In addition to the orbital and rotational influences on tidal heating (Sec. 3), a body's internal structure will affect its heat production, quantified in the Love number k. We discussed, in Sec. 2, how the Love numbers for Io and Europa are generated for the specific structure models we consider for these bodies.

In this chapter we examine the heat budget for each layer within both Io and Europa, and explore how the equilibrium conditions change with an evolving orbit and structure. For a simple two layer Io, we find that there are no stable solutions which can carry more heat out of the body than is generated and the body should undergo some degree of melting, even

at its current eccentricity. On Europa, we find that thick shell models (where all or most of the water is ice rather than ocean) are unstable and will also melt until the shell thins enough that a heat balance is possible. First in Sec. 4.1, we describe the layering of Io and Europa, and quantify the material parameters in each layer. Sec. 4.2 describes the specific general functions we will use to describe tidal, convection, conduction, sensible, and latent heats. Then in Sec. 4.3 and Sec. 4.4 we apply these tools to Io and Europa and examine the resultant equilibrium conditions and their stability.

4.1 Structure Models and Their Love Numbers

In order to reduce the free parameters in the overall model, we will use very simplified structure models. Fig. 4.1 gives a visual guide into the prescribed density and rigidity layering (not to scale) for Io and for Europa. In this section we will describe the material parameters of each body, and report the imaginary component (that which is related to heating) of the k Love number that such a structure produces.

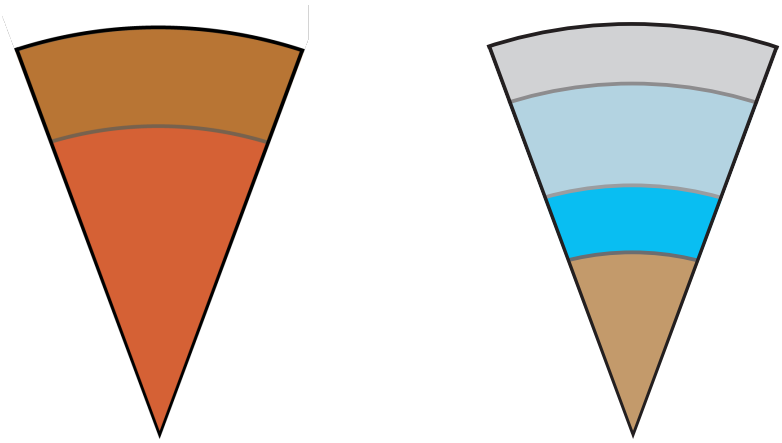

Figure 4.1: Schematics for the two Layer Io (left) and the four layer Europa (right). Io's viscoelastic interior is capped by an elastic lid. Europa's silicate core is surrounded by a water envelope. The water is treated as a fluid ocean overlain by two ice regions. The lower ice is viscoelastic, and the surface ice is elastic

4.1.1 Io

Io is modeled as a two layer body of radius $R_I = 1821\ km$. We assume the inner layer is completely convecting, and that the upper layer is a conductive lid. We label the variable radius of this interface as $r_I = d_I R_I$. We set the density of the two layers equal and to Io's mean density, ρ_I, to simplify the calculation for tidal heating slightly. Except for the addition of the conductive lid, this is a similar structure to that chosen in Ojakangas and Stevenson [19], which treats the body as homogeneous, and so we use the mean density of Io, $\rho_I = 3.531 \times 10^3\ kg\ m^{-3}$. This Io model is some type of silicate rock, although in reality it is unlikely that Io is completely homogeneous in density like this. In fact, studies using the Galileo mission's gravity measurements suggest a mean moment of roughly 0.38 [4]. To achieve this constraint we could add a slightly more dense interior to Io, in the manner of Hussmann and Spohn [9]. This, however, introduces the unknown rigidity of the core to the problem. For simplicity, we will neglect the core and just use the mean density in both layers. We will see in Sec. 4.3 that more complicated structures, possibly including melt layers, might be necessary to accurately model Io.

We also need the rigidity through the body, which we set to a value of $\mu_I = 6.5 \times 10^{10}\ Pa\ s$ in rough comparison to references [7] and [19]. This Io would be homogeneous, but instead we treat the inner layer as viscoelastic while the upper layer remains purely elastic. The viscosity of the inner layer, $\eta_I = \eta_m \left(\frac{T}{T_m}\right)^{-27}$, is a function of temperature (T) with the melting temperature (T_m) and viscosity of that melt (η_m). Hussmann and Spohn [9] detail a pressure dependent melt temperature with values upward of 1800 K for Io, which we use as T_m. For this viscosity at this value we will take a range of values from $\eta_m = 10^{13} - 10^{17}$.

Finally we will need thermal parameters for the silicate material. In particular we need the thermal expansion coefficient, specific heat, and thermal conductivity. Respectively they are $\alpha_T = 3.5 \times 10^{-5}\ K^{-1}$, $C_p = 800\ J\ kg^{-1}\ K^{-1}$, and $k = 4\ W\ m^{-1}\ K^{-1}$.

4.1.1.1 Io k

In Sec. 2 we demonstrate a technique to arrive at simple analytic solutions for the Love numbers of any multi-layered body that has piece-wise continuous density and rigidity radial profiles. For the Io structure that we just presented, we can write the imaginary part of its k Love number as a function of its dissipating layer's temperature T, and the interface position d_I with

$$k_I = -\frac{(k_{fe} - k_{re})\,\Delta_\omega\;\mu_{N_c}}{\left(\Delta_\omega^2 + [1+\mu_{N_c}]^2\right)}$$

$$= -\frac{\left(\frac{3/2}{\left(1+\frac{\mu_I}{\mu_s}\;df_1(d_I)\right)} - \frac{3/2}{\left(1+\frac{\mu_I}{\mu_s}\;df_2(d_I)\right)}\right)\left(\frac{\mu_c\left(\frac{T}{T_m}\right)^{27}}{n_I\eta_m}\right)\;\left(\frac{1-df_2(d_I)}{df_1(d_I)-1}\right)\left(\frac{1+\frac{\mu_I}{\mu_s}\;df_1(d_I)}{1+\frac{\mu_I}{\mu_s}\;df_2(d_I)}\right)}{\left(\left(\frac{\mu_c\left(\frac{T}{T_m}\right)^{27}}{n_I\eta_m}\right)^2 + \left[1+\left(\frac{1-df_2(d_I)}{df_1(d_I)-1}\right)\left(\frac{1+\frac{\mu_I}{\mu_s}\;df_1(d_I)}{1+\frac{\mu_I}{\mu_s}\;df_2(d_I)}\right)\right]^2\right)} \tag{4.1}$$

with

$$\frac{\mu_I}{\mu_s} = \frac{57\mu_I}{8\pi G R_I^2 \rho_I^2} \approx 54.5$$

$$df_1(d) = \frac{24(1-d)\left(19d^8+38d^7+57d^6+d^5-55d^4+d^3+57d^2+38d+19\right)}{19\left(19d^9+19d^8+19d^7+64d^6+64d^5+64d^4+64d^3+24d^2+24d+24\right)}$$

$$df_2(d) = \frac{\left(\left(8\left(6d^5+25d^2-42\right)d^2+225\right)d^3+38\right)}{19\left(-2d^{10}+5d^7-5d^3+2\right)}. \tag{4.2}$$

there would be about

4.1.2 Europa

We model Europa as an inner silicate region, surrounded by a relatively thin layer of water. This water is broken up into three regions; a fluid ocean, a convecting ice layer, and a conductive surface ice. In effect, the silicate region of Europa is a sort of mini-Io which has an ocean on top. We give the water a density of 1000 $kg\ m^{-3}$. The frozen upper regions of this ice should, in fact, be slightly lower in density (940 $kg\ m^{-3}$ is used in Wahr (2009)

[29]). As we expect that latent heat will melt and freeze the water at the ice ocean interface, a density difference would actually result in a change in the entire radius of Europa. If we imagine a slab ice shell, a meter change in the surface height would correspond to a ten meter migration of the lower boundary with phase changes. This is interesting, in and of itself, but in this study is an over complication. We fix Europa's radius to $R_E = 1561\ km$ and give the entire water layer (ocean plus ice shell) a density of $\rho_W = 1000\ kg\ m^{-3}$. Measurements of Europa's mass and mean moment are reported to be $4.8 \times 10^{22}\ kg$ and 0.346 respectively [3]. This lets us determine the radius and density of Europa's silicate interior to be $r_S = 1395\ km$ and $\rho_S = 3820\ kg\ m^{-3}$. We assign the silicates the same rigidity value as for Io, $\mu_s = \mu_I = 6.5 \times 10^{10}\ Pa\ s$. We treat the ocean as a fluid, and so there is no elastic behavior in this region to track. To dramatically simplify the ocean dynamics and neglect any heat generation in this region. In glossing over the ocean, we will treat it as isothermal at the melting temperature ($T_m = 273\ K$). The base of the ice shell is at a variable radius $r_1 = d_1 R_E$. The entire water ice shell is given a rigidity of $\mu_W = 3.5 \times 10^9\ Pa\ s$ from Wahr (2009)[29]. In the ice, again we see a conductive lid overlying a viscoelastic convecting region of viscosity $\eta_W = \eta_m \left(\frac{T}{T_m}\right)^{-27}$. The radius of this interface is found at $r_2 = d_2 R_E$. The thermal parameters we use for the Europan ice are $\alpha_T = 5 \times 10^{-5}\ K^{-1}$, $C_p = 2000\ J\ kg^{-1}\ K^{-1}$, and $k = 3.5\ W\ m^{-1}\ K^{-1}$ for the thermal expansion coefficient, specific heat, and thermal conductivity.

4.1.2.1 Europa *k*

For Europa's Love number, we use Sec. 2 to write the imaginary component of Europa's Love number, as a function of the temperature of the dissipating region (T) and that region's bounding radii ($r_1 = d_1\ R_E$ and $r_2 = d_2\ R_E$) by

$$k_E = -\frac{\left(\frac{0.258-0.00591}{(1+8.11\ df_1(d_2))}\right)\left(\frac{\mu_I\left(\frac{T}{T_m}\right)^{27}}{n_E\eta_m}\right)\ \left(\frac{(1+8.11\ df_1(d_1))}{(1+8.11\ df_1(d_2))}-1\right)}{\left(\left(\frac{\mu_I\left(\frac{T}{T_m}\right)^{27}}{n_I\eta_m}\right)^2+\left[1+\left(\frac{(1+8.11\ df_1(d_1))}{(1+8.11\ df_1(d_2))}-1\right)\right]^2\right)} \tag{4.3}$$

with (repeated from Eq. 4.2)

$$df_1(d) = \frac{24(1-d)\left(19d^8+38d^7+57d^6+d^5-55d^4+d^3+57d^2+38d+19\right)}{19\left(19d^9+19d^8+19d^7+64d^6+64d^5+64d^4+64d^3+24d^2+24d+24\right)}. \quad (4.4)$$

The three values 0.258, 0.00591, and 8.11 are the evaluated functions of the limiting structure models for Europa, all presented in Sec. 2 with the superposition technique we used to determine them.

4.2 Heat Functions

The various layers within Io and Europa will transfer heat in different ways, depending on their thermal and material designations. Viscoelastic layers have a tidal heating input and carry heat away through convection, while elastic layers are conductive. In this section we define the convective, conductive, and tidal heat flows as well as the specific and latent heats which control temperature and structural changes.

4.2.1 Conductive Heat Rate

Conductive heat flux is given by the product of the thermal conductivity, k, and the gradient of the temperature profile T. We assume temperature variations in conductive regions occur in only the vertical, or radial, direction (r). In some circumstances (in Europa's conductive ice for example) one might consider a conductivity which is inversely dependent on temperature $k = \frac{A}{T}$ [18]. We write the conductive heat flux (in $\frac{W}{m^2}$) as,

$$F_{duct} = -k \, \nabla \Big(T(r,t) \Big) . \quad (4.5)$$

If temperature decreases radially within the body (and it will), the negative sign ensures this heat flux is positive valued. In a dynamic model, $T(r,t)$ will be solved for using diffusion, which we look at when we describe sensible heat transfers. Next we introduce conductive equilibrium.

4.2.1.1 Conductive Equlibrium

In conductive equilibrium, $T = T_{eq}$ is such that the divergence of this heat flux is zero or $\nabla \cdot F_{duct} = 0$.

This differential equation has a simple solution which depends on the surface and base temperatures, $T(r = R) = T_s$ and $T(r = dR) = T_b$. The solution for the temperature profile, considering both the constant and temperature dependent conductivities, are

$$T_{eq}(r) = T_s + \frac{d(R-r)}{r(1-d)}(T_b - T_s) \qquad \text{or} \qquad T_{eq,A}(r) = T_s \left(\frac{T_b}{T_s}\right)^{\frac{d(R-r)}{r(1-d)}} . \tag{4.6}$$

Finally, using Eqs. 4.5 and 4.6, we calculate the conductive flux in equilibrium to be

$$F_{eq,duct} = \frac{k\ d\ R}{r^2(1-d)}(T_b - T_s) \qquad \text{or} \qquad F_{eq,duct,A} = \frac{A\ d\ R}{r^2(1-d)} \ln\left[\frac{Tb}{Ts}\right] . \tag{4.7}$$

Notice the inverse square radial dependence, which compensates for the increasing surface area ensuring a divergentless flux in equilibrium.

4.2.2 Convective Heat Rate

Convective heat flux (in $\frac{W}{m^2}$) can be written in terms of the temperature difference across the convection region, ΔT, by

$$F_{vect} = k\frac{\Delta T}{\beta}\left(\frac{Ra}{Ra_c}\right)^{\xi}, \tag{4.8}$$

where Ra is the Rayleigh Number and Ra_c is the critical Rayleigh number, below which convection will not occur [25]. Notice that if the ratio $\frac{Ra}{Ra_c} = 1$, the form of the convective flux mirrors that of conductive flux. That is to say, if the Rayleigh number ratio is less than 1 then $F_{vect} < F_{duct}$, and conductive heat transport is more efficient and it should take over. In reality we should write the flux as $F_{vect} = F_{duct}\left(\frac{Ra}{Ra_c}\right)^{\xi}$. The power ξ is a physical parameter, which can be experimentally determined. A variety of results all cited in (Scubert, Cassen, Peale 1979)[25] indicate we should choose something between $0.25 < \xi < 0.33$. Choosing $\frac{1}{3}$ has the advantage that the heat flow becomes independent of convective thickness (β, see below) and changes only with the temperature difference. This case, however, may only be valid at very high Rayleigh Number. We will choose it, for now, acknowledging this.

Now with α_T, ρ, g, C_p, and η equal to the thermal expansion coefficient, density, surface gravity, specific heat, and viscosity respectively, The Rayleigh Number is given by

$$Ra = \frac{\alpha_T \rho^2 g C_p (T_h - T_c)\beta^3}{k\eta}, \tag{4.9}$$

and essentially describes the ratio of buoyancy to thermal diffusivity in a mass. If the buoyancy forces are high, then the Rayleigh number is large and the mass would rather transport toward the cold region to move the heat, rather than have the heat diffuse out of the mass to move the heat. We use a temperature dependent viscosity, $\eta = \eta_m \left(\frac{T}{T_m}\right)^{-L}$, where η_m is the reference viscosity at the melting temperature, T_m, and L is an experimentally determined constant (we choose $L = 27$ after [9]). The thermal conductivity, k, can be used in either constant or temperature dependent forms, as we did in Sec. 4.2.1. Putting this all together we have,

$$F_{vect} = \left(\frac{\alpha_T \rho^2 g C_p}{k\ Ra_c\ \eta_m}\right)^{\frac{1}{3}} \left(k \left(\frac{T_C}{T_m}\right)^{\frac{27}{3}} (T_m - T_C)^{\frac{4}{3}}\right). \tag{4.10}$$

This function depends on temperature in two ways. For the part coming from viscosity, a colder material is more stiff and less free to flow and this inhibits convective heat transfer. The temperature difference term, alternately slows convection at temperatures closer to the melting temperature, because if everything is already isothermal there is no real drive to move heat convectively and conduction should take over.

4.2.3 Tidal Heat Rate

In Sec. 3 we describe a robust method for determining the spatially resolved tidal heating rate. This is very useful in locating specific lateral and radial points in which the frictional heat from tidal deformation peaks. For this global heat balance model, however, we use the globally integrated tidal heat production functions which depend on the imaginary part of the k Love number. We also find that for synchronously rotating bodies with no obliquity in their spin, the only frequency which delivers significant tidal energy to the body is n, the mean motion of the orbit. With this we find the global rate of tidal heat generation (in W),

is the classic expression

$$\dot{Q}_{tide} = -\frac{3}{2}\frac{n^5 R^5}{G} k_I \left(7e^2 + \sin^2 o\right). \tag{4.11}$$

We ignore the spin obliquity, o, for now so that the behavior depends entirely on eccentricity (e), the mean motion (n), and the imaginary part of the gravity Love number (k_I). This Love number will be negative valued (so the heat rate will be positive valued), and depend on the density and rigidity structure of the body. While we left the convective and conductive heats as flux expressions (F) in watts per unit meter, we are leaving the tidal heat as a rate ($\dot{Q}$) in watts.

4.2.4 Dynamic Heat Wells

If there are imbalances in heat inputs and outputs sensible heat is one form of dynamic heat transfer. A change in sensible heat translates into a change in either temperature or in mass. The total sensible heat in any given mass m at a temperature T is given by $Q_{sens} = mC_pT$. We differentiate in time to find the sensible heat rate (W)

$$\dot{Q}_{sens} = \dot{m}\ C_p\ T + m\ C_p\ \dot{T}. \tag{4.12}$$

If that mass change is a phase change (which we anticipate on Europa) then the latent heat rate (W) is,

$$\dot{Q}_{lat} = \dot{m}\ L. \tag{4.13}$$

4.3 Io's Heat Balance

In Io, the general picture is that tidal heat is input into the satellite's viscous region and must escape out to space. The tidally heated region undergoes convection and the heat moves upward and outward toward Io's conductive lid, where it ultimately conducts out into space. Any imbalances between the heat input into a region compared to heat carried out of a region lead to temperature changes as well as variations in the position of the two layers' interface. In this section we will describe these heat transfers in each layer, and track the temperatures and thicknesses where equilibrium occur. Once equilibrium states are found,

we assess the stability of the equilibrium point.

4.3.1 Differential Equations

The total tidal heat is produced in the viscoelastic inner region is $\dot{Q}_{tide}$. The total heat is carried out of this region by convection is $\dot{Q}_{vect} = 4\pi r_I^2 \; F_{vect}$, where we have multiplied the heat flux by the surface area of the region. If there is an imbalance in these heats in and out, then the temperature of the convection region changes from sensible heating $\dot{Q}_{sens}$, where we have substituted the mass of the convecting region. We write,

$$\begin{aligned} \dot{Q}_{sens} &= \dot{Q}_{tide} - \dot{Q}_{vect} \\ \frac{4}{3}\pi\rho \; r_I^3 \; C_p \; \dot{T_C} &= \left(-\frac{21}{2}\frac{n_I^5 R_I^5}{G} k_I \; e^2 \right) - 4\pi r_I^2 \left(\frac{\alpha_T \rho^2 g C_p}{k \; Ra_c \; \eta_m} \right)^{\frac{1}{3}} \left(k \left(\frac{T_C}{T_m} \right)^{\frac{27}{3}} (T_m - T_C)^{\frac{4}{3}} \right), \end{aligned} \tag{4.14}$$

the differential equation in the temperature of Io's convecting interior, $T_c = T(r_I, t)$. It is tempting to want to put a latent component in the sensible heating term. The Love number that we built, in Sec. 4.1, is not built with this in mind, so if we were to do this we would need to reconstruct the Love number first. As we shall see in Sec. 4.3.2, this may be an interesting task for the future.

Throughout the conductive region the temperature profile will always adjust toward equilibrium, where the flux is divergent-less. If it is not in equlibrium, and needs to adjust, it does so through diffusion. The heat equation governs diffusion, written

$$\rho \; C_p \; \dot{T}(r,t) = \nabla \cdot \Big(-k \; \nabla \, T(r,t) \Big), \tag{4.15}$$

describes how the temperature profile changes in time, in the event the flux is in dis-equilibrium. We have some boundary conditions for $T(r,t)$. First, the surface temperature is fixed constant at, $T(R_I, t) = T_s \approx 100k$. The other boundary temperature is at the conductive lid base, where the temperature is determined by the heat balance in the convective layer. The boundary temperature should then be $T(r_I, t) = T_C$. It is worth noting that diffusion of heat through the conductive lid will probably end up as the rate limiting step.

The diffusion timescale goes as $\tau = \frac{L^2}{\alpha}$, where the thermal diffusivity of Io's lid is on the order of $\alpha = \frac{k}{\rho C_p} \approx 10^{-6}\ m^2\ s^{-1}$. For a lid of just 10 km, this translates to a roughly three million year timescale to diffuse heat across the lid.

Right at the boundary between the two interfaces, the temperature will be continuous however the heat flow may not be. The imbalance in heat flow, can not change the temperature (which is determined through the heat balance in the layer below), but sensible heats can still exchange if mass, already at the temperature of convection, is transferred between the layers. That is, if conduction can carry more heat away than convection can deliver, then the surface layer will increase in thickness, at the expense of the mantle's volume. Conversely, extra convection heat will thin the lithosphere. We express the heat balance with,

$$\begin{aligned} F_{sens} &= F_{vect} - F_{duct}(r = r_I) \\ \rho\ C_p\ T_C\ \dot{r_I} &= \left(\frac{\alpha_T \rho^2 g C_p}{k\ Ra_c\ \eta_m}\right)^{\frac{1}{3}} \left(k \left(\frac{T_C}{T_m}\right)^{\frac{27}{3}} (T_m - T_C)^{\frac{4}{3}}\right) - \left(-k\ \nabla\ T(r,t)\Big|_{r=r_I}\right). \end{aligned} \tag{4.16}$$

4.3.2 Equilibrium Conditions and Stability

In this section we examine the differential equations for Io's heat balance in the equilibrium condition. We set all time derivatives in the temperature and the interface location to zero. At any equilibrium in the (T, d_I) space we have that all three heats (tidal, convection, and conduction) will be equal. Specifically,

$$\dot{Q}_{tide} = \dot{Q}_{vect} = \dot{Q}_{eq,duct}, \tag{4.17}$$

where $\dot{Q}_{eq,duct} = 4\pi r_I^2 F_{eq,duct}$. For Io, we see that there are two regimes of equilibrium; A "cold convection" scenario, where most of the body is convecting at a relatively low temperature capped by a thin lid, and a "warm convection" scenario, where the inner region is small but has convection at a higher temperature (close to the melting point).

In Fig. 4.2 we plot the total tidal heat (yellow) in watts, the total convective heat transferred to the lithosphere interface (pink), and the total heat conducted through the lithosphere (blue). When these lines intersect, the body is in thermal equilibrium. Each column

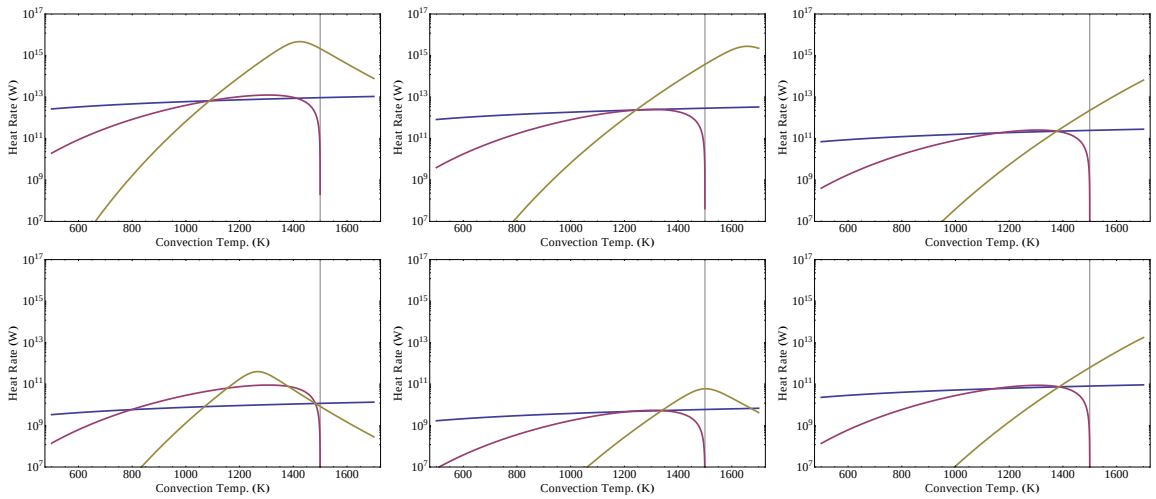

Figure 4.2: Magnitudes of heat flow (in watts) for tidal (yellow), convection (red), and conduction (blue). Intersections of all three curves identify equilibrium conditions in (T,d,η_m) space. Each column of plots represents, left to right, $\eta_m = 10^{13}$, 10^{15}, and 10^{17} $Pa\ s$. The top row is for solutions with high d and low T, called "cold convection", while the bottom row describes the opposite in "warm convection".

represents a silicate melt viscosity, η_m (10^{13} $Pa\ s$, 10^{15} $Pa\ s$, and 10^{17} $Pa\ s$ from left to right). The top row shows the "cold convection" equilibrium, and the bottom row shows the case for "warm convection". We see that increasing the melt viscosity causes the warm and cold solutions to merge, with the critical limiting melt viscosity just slightly greater than about 10^{17} $Pa\ s$, above which no equilibrium solutions are found. Past this critical limit, the high viscosity yields low heat production and inefficient transport through convection, and conduction becomes the preferred heat transfer mechanism, essentially freezing out the body. For the tidal heating curve, its magnitude is modulated by a factor $n^5\ e^2$. In general, an increase in this factor (higher eccentricity and/or mean motion increase tidal heat production) drives the equilibrium toward colder solutions with a thinner conductive lid.

Now that we know that equilibrium solutions with reasonable parameters exist for the Io model, we determine the stability of the hot and cold solutions. We begin with equilibrium at low melt viscosity $\eta_m = 10^{13}$ $Pa\ s$. In Fig. 4.3, first column simply repeats the heat rate plots for the cold and warm solutions from Fig. 4.2. The second and third columns plot the heat rate differences given by Eqs. 4.14 and 4.16 at either an equilibrium temperature or

radius as a function of the other. When both heat rate differences equal zero the system is in equilibrium. These heat rate differences should be interpreted as the time rate of change of convection temperature and interface position because $\left(\dot{Q}_{tide} - \dot{Q}_{vect}\right) \propto \dot{T}_C$ given in the blue curve and $\left(\dot{Q}_{vect} - \dot{Q}_{duct}\right) \propto \dot{d}_I$ shown in red. Plotting the functions as so allows us to assess the stability of an equilibrium point, in the event of a perturbation in the variables, by simply noting the slope of a heat balance when it is in equilibrium (and equals zero).

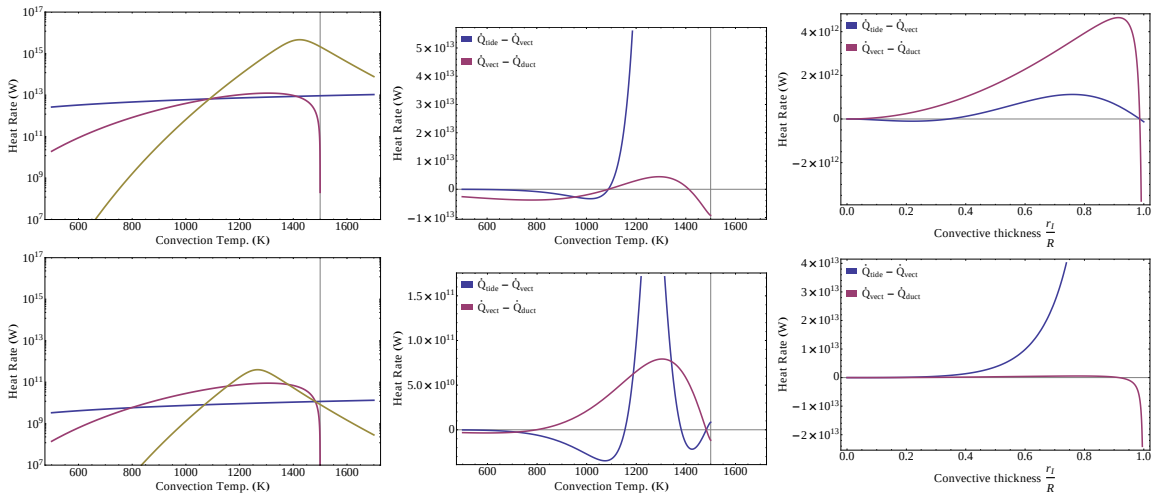

Figure 4.3: The left column gives the cold (top) and warm (bottom) convection solution heat flows for $\eta_m = 10^{13}\ Pa\ s$. The center column shows how the heat rate differences are functions of temperature, while the right column looks at those functions interface position dependence. In the center and right columns, the blue curve can be thought of as proportional to the temperature increase. The red curve is proportional to an interface position increase.

For the cold equilibrium at $T_C = 1088\ K$ and $d_I = 0.986$, shown in the top row, we see that a positive perturbation in temperature (center) from the equilibrium causes a further increase in temperature (blue curve is positive). Similarly, a negative perturbation causes additional cooling, however much decreased in magnitude and quick to shallow off, relative to the positive perturbation. This is to say that the temperature is unstable at this equilibrium, but with a tendency to increase in temperature more easily. The sharp negative slope of the red curve in the right panel, describing $\dot{d}_I$, shows that perturbations away from equilibrium tend to draw the interface back to the equilibrium radius. And so the radius is at a very stable equilibrium here. The stability in radius is notable, as the equilbrium point has a lid

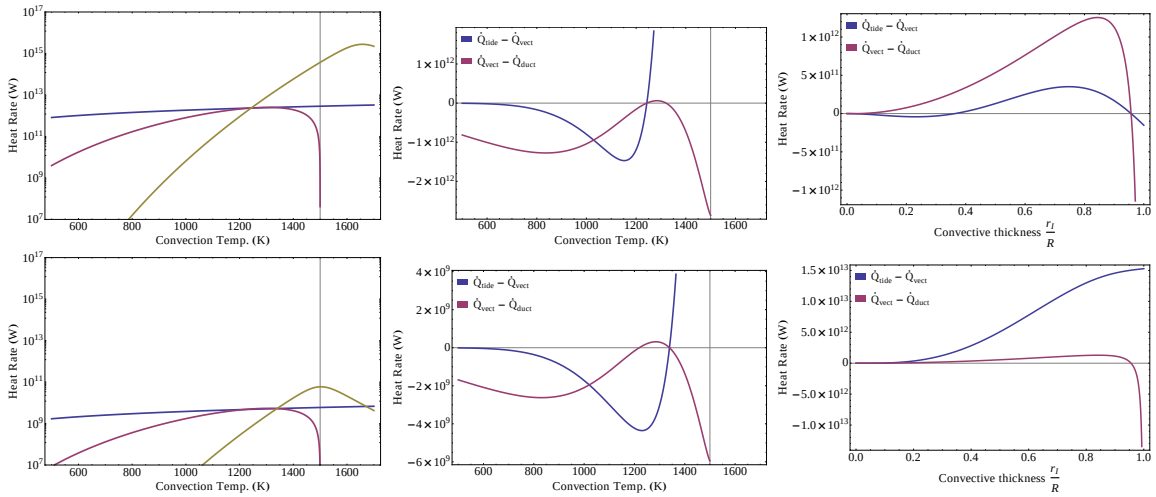

Figure 4.4: The left column gives the cold (top) and warm (bottom) convection solution heat flows for $\eta_m = 10^{15}\ Pa\ s$. The center column shows how the heat rate differences are functions of temperature, while the right column looks at those functions interface position dependence. In the center and right columns, the blue curve can be thought of as proportional to the temperature increase. The red curve is proportional to an interface position increase.

thickness with only 1% of the body radius. Such a thin shell could not get much more thin, and the instability sort of ensures that the body remains two layered with the conductive lid. All in all, for this cold convection, the equilibrium is a saddle point, very stable in radius, but unstable in temperature. In the event of a perturbation, the tendency would be to try to increase in temperature while retaining the radius of the internal interface.

For the warm solution in the bottom row, found at $T_C = 1482\ K$ and $d_I = 0.084$, one will notice that a perturbation from equilibrium in both temperature and in radius is associated with a positive $\dot{T}_C$ or $\dot{d}_I$ and unstable solutions (seeing that the values of the derivatives are positive valued at $d_I = 0.084$ in the bottom right plot is difficult...). The derivative on the negative side of thickness equilibrium approaches zero, while it increases quickly compared to the positive side. This means that the instability here should favor an increase in the convective regions thickness. This is reasonable, because the equilibrium radius is almost zero to start and getting any smaller pushes the body toward a one layer completely conductive body.

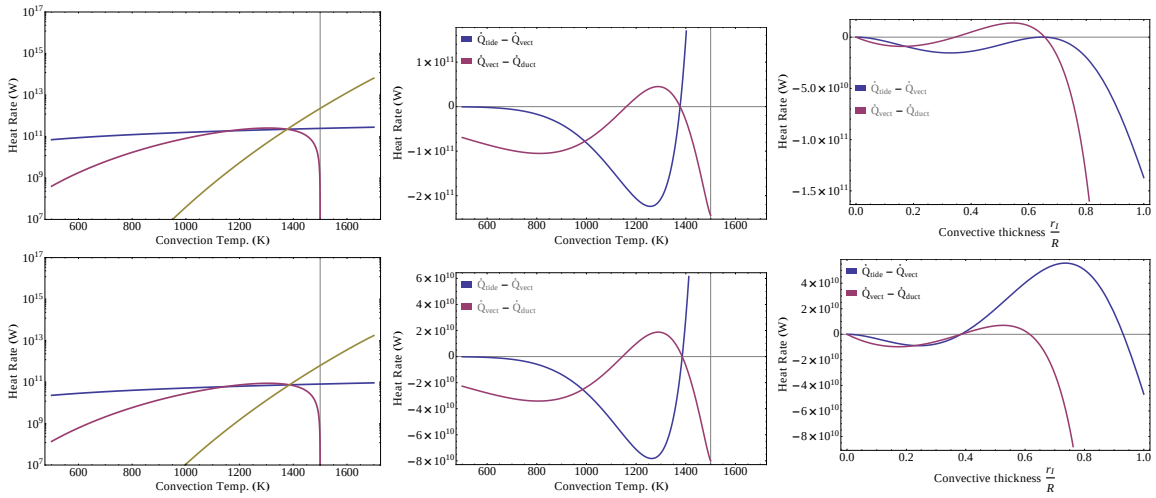

Figure 4.5: The left column gives the cold (top) and warm (bottom) convection solution heat flows for $\eta_m = 10^{17}\ Pa\ s$. The center column shows how the heat rate differences are functions of temperature, while the right column looks at those functions interface position dependence. In the center and right columns, the blue curve can be thought of as proportional to the temperature increase. The red curve is proportional to an interface position increase.

Increasing the melt viscosity to $\eta_m = 10^{15}\ Pa\ s$, we find that the two equilibrium points have moved to $(T_C = 1243\ K, d_I = 0.957)$ and $(T_C = 1339\ K, d_I = 0.044)$. The heat rates, and their differences are shown in In Fig. 4.4. In both the hot and cold equlibrium, we see the same general behavior as we did with the lower melt viscosity. That is, a cold solution unstable in temperature but stable in radius, and a warm solution unstable in temperature and radius.

When we look at $\eta_m = 10^{17}\ Pa\ s$ In Fig. 4.5 the solutions are at $(T_C = 1377\ K, d_I = 0.656)$ and $(T_C = 1386\ K, d_I = 0.384)$. These all have the same stability classifications as the other two lower melt viscosity scenarios we examined.

Our Io model, at the range of melt viscosity considered, appears unstable in temperature and should undergo runaway heating. Io would then melt in its interior to compensate and lock up some heat. This has the additional effect of reducing the volume of the dissipating region (the now fluid melt does not store or dissipate elastic energy), also helping to drive down the tidal heating term, which is causing the heating. When the lid is thin the convection

temperature is cool, and, in general, the body warms as the lid thickens. There is the potential for melting events to occur, due to a positive temperature perturbation at the warm equilibrium. Phase changes in the Io model were not originally considered, however, in the dynamic model if we see temperatures climb above the melting temperature, we might consider more complicated structure models for Io's interior which include a solid core with a fluid silicate melt layer below the viscous and elastic silicate regions. This would also help match our Io to estimates of Io's mean moment of inertia [4].

4.4 Europa's Heat Balance

The Europa picture is quite similar to that of Io, in terms of the heat pairs that must balance, except we adjust our parameters for ice instead of silicates. For now we neglect dissipation in the silicate interior as well as the ocean. We essentially treat the ocean as reservoir of latent heat at the ice ocean interface, that is at the melting temperature (273 K). We find that if viscoelastic cores are considered in Europa, in addition to in just the ice, the change in the Love number is insignificant. Becuase of this we treat the core as elastic and non-dissipative, however we readily admit that neglecting it probably does inhibit some of the dynamics of the ice ocean interface position. Perhaps even more realistic, would also be to consider turbulent motions in the fluid ocean as a source of heat, however is beyond the scope of this study. We are hopeful that future interpretations of this system can include such effects. This section will describe the relevant heat balance expressions for Europa, find equilibrium states, and assess their stability. These expressions will be almost exact mirrors that they were for Io, except for the geometry (the convective layer is a spherical shell here with an ocean below, where it was an ellipsoidal region in Io). One addition we consider with Europa, that we neglected on Io, is a migrating ice ocean boundary. We expect latent heat exchanges from the phase transfer of water as the boundary migrates.

4.4.1 Differential Equations

Once again, in the viscoelastic region we balance the total tidal heat generated in the layer with the total heat convected out through the layer's upper surface. Imbalance of heat causes the convection temperature to raise and we say,

$$\begin{aligned} \dot{Q}_{sens} &= \dot{Q}_{tide} - \dot{Q}_{vect} \\ \frac{4}{3}\pi\rho\left(r_2^3 - r_1^3\right)\ C_p\ \dot{T_C} + \rho\ L\ \dot{r_1} &= \left(-\frac{21}{2}\frac{n_E^5 R_E^5}{G} k_E\ e^2\right) \\ &\quad - 4\pi r_2^2 \left(\frac{\alpha_T \rho^2 g C_p}{k\ Ra_c\ \eta_m}\right)^{\frac{1}{3}} \left(k\left(\frac{T_C}{T_m}\right)^{\frac{27}{3}} (T_m - T_C)^{\frac{4}{3}}\right) \end{aligned} \tag{4.18}$$

For Europa, the k Love number we are using is characterized in such a way to include the effects of an ocean below. Because of this we can allow for a latent rate term in $\dot{Q}_{sens}$. If the temperature ever raises above the melting temperature, ice will melt off of the bottom of the shell. This stores excess energy as latent heat, and reduces the dissipating volume and therefore tidal heating.

Europa's conductive surface layer has a temperature profile guided by diffusion. Just as with Io, the expression for heat diffusion goes,

$$\rho\ C_p\ \dot{T}(r,t) = \nabla \cdot \left(-k\ \nabla\, T(r,t)\right). \tag{4.19}$$

We use the same surface boundary temperature of $T(R_E, t) = T_s \approx 100k$, and we say that the temperature at the lower boundary is $T(r_2, t) = T_C$. The thermal diffusivity for the ice is comparable to that for the silicates, in that we should expect diffusion through the ice to be a rate limiting process for Europa's heat escape as we did with Io.

At the boundary between the two ice layers, the temperature is continuous and determined by the heat balance in the convective layer below. In lieu of controlling temperature, an imbalance in the convective heat deposited into the boundary relative to that carried away through conduction changes the position of the ices' interface. For this we write,

$$F_{sens} = F_{vect} - F_{duct}(r = r_2)$$

$$\rho\ C_p\ T_C\ \dot{r_2} = \left(\frac{\alpha_T \rho^2 g C_p}{k\ Ra_c\ \eta_m}\right)^{\frac{1}{3}} \left(k \left(\frac{T_C}{T_m}\right)^{\frac{27}{3}} (T_m - T_C)^{\frac{4}{3}}\right) - \left(-k\ \nabla\ T(r,t)\Big|_{r=r_2}\right). \quad (4.20)$$

4.4.2 Equilibrium Conditions and Stability

In this section we explore the parameter space for which equilibrium solutions exist with our Europa heat model. Once identified, just as we did with Io, we will determine the stability at these points. Once again, in Fig. 4.6 we plot the tidal, convective, and conductive heat rates at the location of the internal ice-ice boundary (r_2) all as a function of the temperature of convection. This time, we are more confident of the viscosity of the ice at its melting temperature, $\eta_m = 10^{13}\ Pa\ s$, which seems a typical value found in similar studies (for example Hussmann and Spohn (2004) [9]). The true viscosity of this melt, of course, is probably modified from this due to the various salts and other chemical species which are likely present at (and probably participate in the dynamics of) the ice ocean interface. In our simplified structure, however, $10^{13}\ Pa\ s$ is sufficient. Here, instead of probing η_m space, the panels explore various values for r_1, and then an r_2 and T_C are identified for which an equilibrium exists.

Fig. 4.6 shows three choices for the position of the ice ocean interface, d_1 at 0.9, 0.933, and 0.967 represented in each column. These correspond to total ice shell thicknesses of about 156 km, 105 km, and 52 km respectively (for context, the entire H2O region of ocean and ice is roughly 166 km thick). Again we find cold and hot solutions, designated by row. As was with Io, the cold solutions accompany a thick convecting region, where the hot solutions have a thinner layer of convection (and dissipation). The cold solutions all tend to resemble what we saw in Io, in regard to the relative positions of the heat rate curves. The hot solutions, however, are quite different and more so resemble the warm Io solution we saw at low melt viscosity. In these warm solutions the equilibrium is found when the tidal heating curve is decreasing, and this can affect the stability of these points.

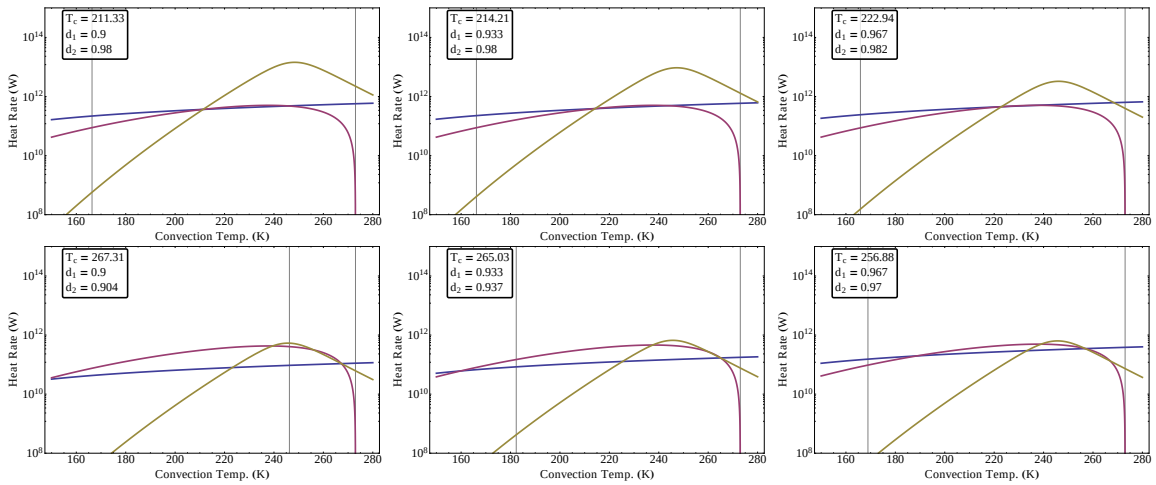

Figure 4.6: Magnitudes of heat flow (in watts) for tidal (yellow), convection (red), and conduction (blue). Intersections of all three curves identify equilibrium conditions in (T,d,η_m) space. Each column of plots represents, left to right, $d_1 = 0.90$, 0.93, and 0.96. The top row is for solutions with high d and low T, called "cold convection", while the bottom row describes the opposite in "warm convection".

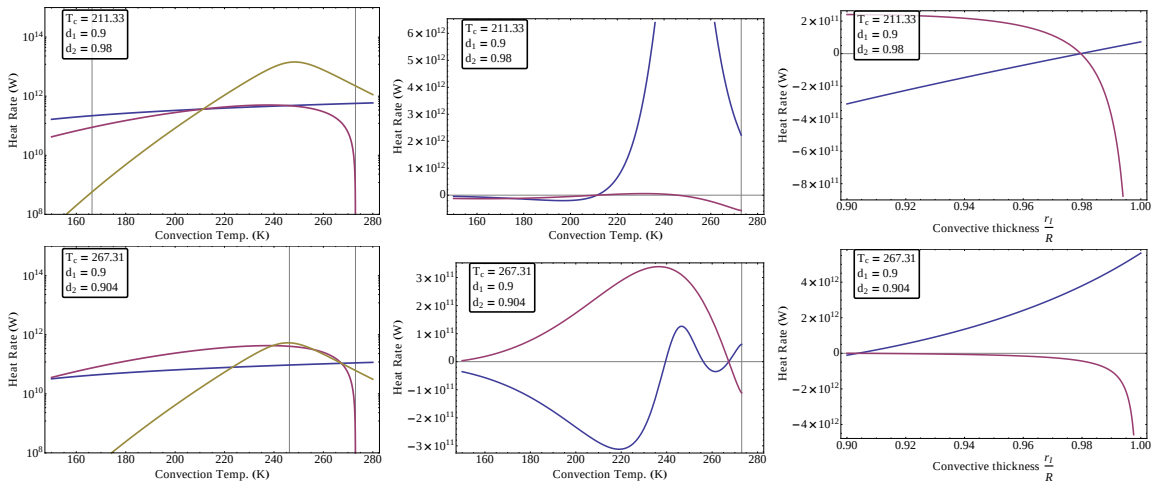

Figure 4.7: The left column gives the cold (top) and warm (bottom) convection solution heat flows for $d_1 = 0.90$. The center column shows how the heat rate differences are functions of temperature, while the right column looks at those functions interface position dependence. In the center and right columns, the blue curve can be thought of as proportional to the temperature increase. The red curve is proportional to an interface position increase.

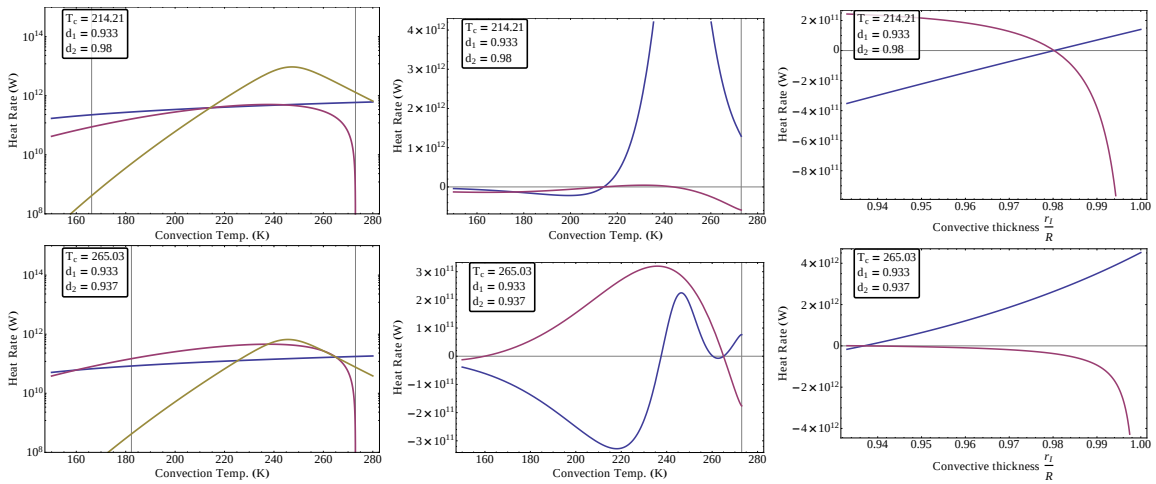

Figure 4.8: The left column gives the cold (top) and warm (bottom) convection solution heat flows for $d_1 = 0.93$. The center column shows how the heat rate differences are functions of temperature, while the right column looks at those functions interface position dependence. In the center and right columns, the blue curve can be thought of as proportional to the temperature increase. The red curve is proportional to an interface position increase.

The stability of the 156 km ice shell is explored in Fig. 4.7. In both the warm and cold solutions we see an unstable temperature with the tendency to increase. The interface depth is stable, however. It appears that this model could see Europa's lower ice Layer run-away in heating, just as was the case with Io.

The Europa Love number model is capable of inducing melting and so as melt occurs, the value of d_1 increases. In Fig. 4.8, we show this in the scenario for a thinner 105 km shell. The thinning of the shell has pulled the equilibrium temperature back under the melting point, however still here we find the same stability scenario of a stable interface but an unstable temperature. Apparently, not enough ice has melted.

Finally in Fig. 4.9, enough ice has melted so that the ice shell is now 52 km thick. Again, we find the stability with respect to interface position. Also familiarly, for the cold solution the temperature is unstable and likely to increase. At this shell thickness, however, we find an important difference in the warm solution. Here the temperature is also stable. That is to say, once the shell has melted and thinned enough, the dissipating region is low enough in volume that a stable equilibrium is found. It is important to note that the tidal

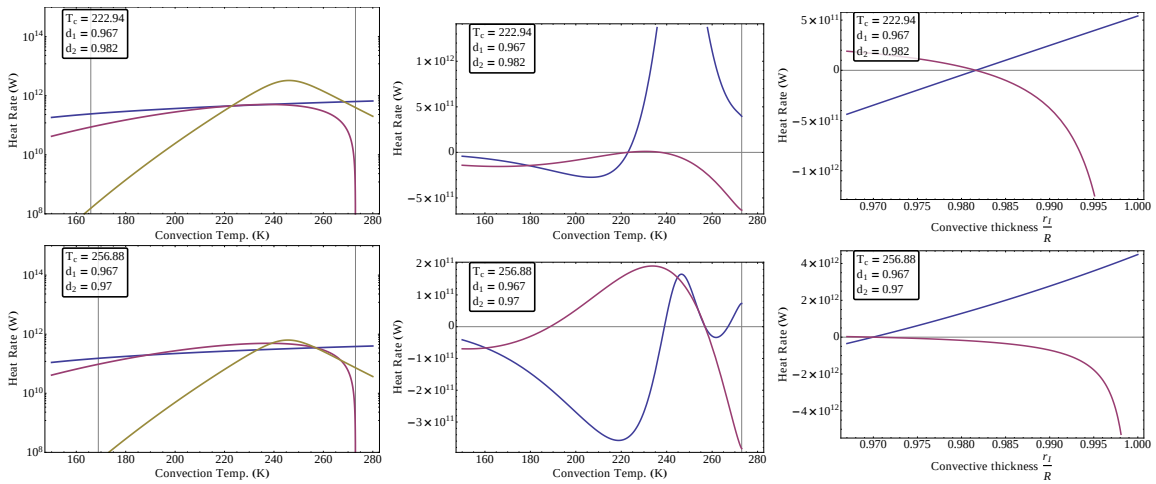

Figure 4.9: The left column gives the cold (top) and warm (bottom) convection solution heat flows for $d_1 = 0.96$. The center column shows how the heat rate differences are functions of temperature, while the right column looks at those functions interface position dependence. In the center and right columns, the blue curve can be thought of as proportional to the temperature increase. The red curve is proportional to an interface position increase.

input is expected to vary. This increases (or decreases) the shell thickness for which an equilibrium exists. This will mean that the equilibrium shell thickness found will vary in time with the orbital parameters. A detailed study of the orbital evolution is reserved for future examinations.

4.5 Conclusion

In this chapter we have presented a simple set of thermal models to determine the stability of the structure and temperature profiles in both Io and Europa. These bodies have a dissipating region which convects heat upwards and into a conducting lid. On Io the heat transfers all take place in silicate materials, while on Europa this takes place in ice. The Europa model considers a variable ice ocean interface as a lower boundary for the dissipating ice.

For Io, we find that if the viscosity of melted silicates is too high (over about 10^{17} $Pa\ s$) then there are no structural configurations which can support convection at the current

eccentricity and mean motion. As we explore reduced melt viscosity values we find a set of two equilibrium solutions. One we label "warm convection" and describes a less massive region convecting at a temperature relatively close to the melting temperature. The other "cold convection" has a cooler interior convecting almost all the way to the surface. Both of these equilibria are unstable in temperature, however, and have the potential for a runaway internal heating. This argues our structure models need to be updated to include more detailed layering. In the future Io models of this type should include a dense core and/or a fluid silicate melt region. Either of these structural scenarios will reduce the dissipating volume, possibly pulling the thermal model toward stable equilibrium solutions.

With the Europa model using thick ice shells we found similar circumstances as we did for Io, in that there are two solutions unstable in temperature. Here, instead of exploring the melt viscosity space, we fix that parameter and instead vary the shell thicknesses. We find that a shell can thin enough, and this can provide for stable equilibria. On Europa, with current orbital parameters we predict a stable shell of roughly $50km$.

CHAPTER 5

Conclusion

In order to understand how thermal processes can evolve the structure of a planet, we have constructed a set of coupled models and applied them to Io and Europa. First in Ch. 2, we looked at the Love number parameters which describe the displacements and potential perturbation from some applied forcing. We identify the theoretical fluid limits, and comment that the fluid l Love number, which is typically reported to be $\frac{3}{4}$, should in fact be $\frac{5}{4}$. The corrected value we provide allows bulk stress to dissipate, where the standard treatments do not. Furthermore, we find a theoretically measurable new "tilt factor" which relates the l and k Love numbers. In analogy to the classic tilt factor, which describes the difference between the deformed surface figure height and an equipotential height, our parameter describes the poleward deflection of mass under some deformation, relative to the flow to equilibrium. We close our discussion of Love numbers with explicit calculations for Io's and Europa's k values. In this we demonstrate our superposition technique, which isolates a layer at a time and differences the Love number's fluid and rigid limits. In this simple representation we can succinctly present the Love numbers for the bodies, written in terms of the temperature of their convecting interiors, as well as the variable interface positions within the body. As these interfaces migrate and the structure evolves, the thermal balance within the bodies adjust.

We explore the spectrum of tidal heating in Ch. 3. The tidal potential operates at a variety of frequencies related to the orbit and spin of a body, and so heating will also operate at all these frequencies. Tidal heating is linearly proportional to the k Love number, which is a strong function of forcing frequency. Typically, tidal heating is considered at the mean motion frequency only, but it is quite possible that k is reduced there. For complicated tides,

we find that multiple frequencies (typically sums and differences of mean motion and spin rate) have the potential to deliver more heat than the orbital frequency, especially if the Love number peaks at one of these other beats. To demonstrate examples where the frequency which delivers the majority of heat is not the mean motion, we consider tidal heating at Mercury and at Venus. We find that on Mercury, the spin orbit resonance eliminates the heating contribution from the strongest eccentricity tide completely. This seems counter intuitive, for the most eccentric planet it our Solar System. On Venus, the heating associated with the slower than synchronous retrograde spin finds three orders of magnitude more heat delivery at high frequencies than is found at the orbital frequency. For our intended targets, Io and Europa, which rotate synchronously and have very low spin obliquity, heat delivery is adequately determined through the simple and well described classical tidal heating equation.

In Ch. 4, we apply the Love numbers for Io and Europa that we generated to thermal heat balance models. We balance tidal heat input with heat escape out of the bodies, and identify parameter sets which produce equilibrium conditions. On Io, we find that equilibrium is possible, however, unstable. With our current Io structure models the satellite overheats and should melt. In the future, we might add a dense elastic core to our Io models and/or a fluid silicate melt layer. This will reduce the mean moment of inertia, in agreement to observation, and also reduce the volume of dissipating material. This will pull the tidal heating rate down and also allow heat to be stored, latently, in the silicate melt. We expect that this may result in stable equilibrium conditions. On Europa we allow phase transitions. We find that for thick ice shells, all equilibrium scenarios found deliver too much heat and cause melting. The ice shell then thins until an equilibrium thickness is found where stable conditions are recognized. For Europa's current orbital conditions, ice shells of roughly $50km$ provide the stable conditions.

Space missions to the Galilean satellite system are likely, with The Europa Clipper mission is expected there by roughly 2030. With radio science, this mission is expected to measure the k Love number. Ice penetrating radar is also proposed to be used to probe ice shell thickness. Our models predict relationships between the Love numbers, heat flow, and thickness. Therefore using mission data, along with the relationships we envision, we should

be able to further constrain the structural and rheological parameters of Europa's ice to aid in the interpretation of Europa's current state. Using the constrained models we can then more accurately predict the thermal and structural evolution histories and trajectories.

References

[1] D.C. Agnew. 3.06 - earth tides. In Gerald Schubert, editor, *Treatise on Geophysics*, pages 163 – 195. Elsevier, Amsterdam, 2007.

[2] Z. Alterman, H. Jarosch, and C. L. Pekeris. Oscillations of the Earth. *Royal Society of London Proceedings Series A*, 252:80–95, August 1959.

[3] J. D. Anderson, G. Schubert, R. A. Jacobson, E. L. Lau, W. B. Moore, and W. L. Sjogren. Europa's differentiated internal structure: Inferences from four galileo encounters. *Science*, 281(5385):2019–2022, 1998.

[4] J. D. Anderson, W. L. Sjogren, and G. Schubert. Galileo gravity results and the internal structure of io. *Science*, 272(5262):709–712, 1996.

[5] M. Beuthe. Spatial patterns of tidal heating. *Icarus*, 223:308–329, March 2013.

[6] C. F. Chyba and C. B. Phillips. Europa as an Abode of Life. *Origins of Life and Evolution of the Biosphere*, 32:47–67, February 2002.

[7] H.-J. Fischer and T. Spohn. Thermal-orbital histories of viscoelastic models of Io (J1). *Icarus*, 83:39–65, January 1990.

[8] M. Gillon, A. H. M. J. Triaud, B.-O. Demory, E. Jehin, E. Agol, K. M. Deck, S. M. Lederer, J. de Wit, A. Burdanov, J. G. Ingalls, E. Bolmont, J. Leconte, S. N. Raymond, F. Selsis, M. Turbet, K. Barkaoui, A. Burgasser, M. R. Burleigh, S. J. Carey, A. Chaushev, C. M. Copperwheat, L. Delrez, C. S. Fernandes, D. L. Holdsworth, E. J. Kotze, V. Van Grootel, Y. Almleaky, Z. Benkhaldoun, P. Magain, and D. Queloz. Seven temperate terrestrial planets around the nearby ultracool dwarf star TRAPPIST-1. *Nature*, 542:456–460, February 2017.

[9] H. Hussmann and T. Spohn. Thermal-orbital evolution of Io and Europa. *Icarus*, 171:391–410, October 2004.

[10] A. P. Ingersoll and A. R. Dobrovolskis. Venus' rotation and atmospheric tides. *Neture*, 275:37, September 1978.

[11] H. M. Jara-Orué and B. L. A. Vermeersen. Effects of low-viscous layers and a non-zero obliquity on surface stresses induced by diurnal tides and non-synchronous rotation: The case of Europa. *Icarus*, 215:417–438, September 2011.

[12] H. Jeffreys. *The Earth: Its Origin, History and Physical Constitution.* Cambridge University Press, 1970.

[13] W. M. Kaula. Tidal Dissipation by Solid Friction and the Resulting Orbital Evolution. *Reviews of Geophysics and Space Physics*, 2:661–685, 1964.

[14] Krishan K. Khurana, Xianzhe Jia, Margaret G. Kivelson, Francis Nimmo, Gerald Schubert, and Christopher T. Russell. Evidence of a global magma ocean in io's interior. *Science*, 332(6034):1186–1189, 2011.

[15] M. G. Kivelson, K. K. Khurana, C. T. Russell, M. Volwerk, R. J. Walker, and C. Zimmer. Galileo Magnetometer Measurements: A Stronger Case for a Subsurface Ocean at Europa. *Science*, 289:1340–1343, August 2000.

[16] AEH Love. The yielding of the earth to disturbing forces. *Proceedings of the Royal Society of London. Series A*, 82(551):73–88, 1909.

[17] W.H. Munk and G.J. MacDonald. *The Rotation of the Earth: A Geophysical Discussion*. Cambridge Monographs on Mechanics and Applied Mathematics. University Press, 1975.

[18] F. Nimmo and M. Manga. *Geodynamics of Europa's Icy Shell*, page 381. 2009.

[19] G. W. Ojakangas and D. J. Stevenson. Episodic volcanism of tidally heated satellites with application to Io. *Icarus*, 66:341–358, May 1986.

[20] S. J. Peale and P. Cassen. Contribution of tidal dissipation to lunar thermal history. *Icarus*, 36:245–269, November 1978.

[21] S. J. Peale, P. Cassen, and R. T. Reynolds. Melting of Io by tidal dissipation. *Science*, 203:892–894, March 1979.

[22] W. R. Peltier. The impulse response of a Maxwell earth. *Reviews of Geophysics and Space Physics*, 12:649–669, November 1974.

[23] R. Sabadini and B. Vermeersen. *Global Dynamics of the Earth: Applications of Normal Mode Relaxation Theory to Solid-Earth Geophysics*. Kluwer Academic Publishers, 2004.

[24] Masanori SAITO. Some problems of static deformation of the earth. *Journal of Physics of the Earth*, 22(1):123–140, 1974.

[25] G. Schubert, P. Cassen, and R. E. Young. Subsolidus convective cooling histories of terrestrial planets. *Icarus*, 38:192–211, May 1979.

[26] T SHIDA. A supplement to on the body tides of the earth.. *Tokyo Sugaku-Buturigakkwai Kizi Dai 2 Ki*, 6(18):273–275, 1912.

[27] B. A. Smith, L. A. Soderblom, R. Beebe, J. Boyce, G. Briggs, M. Carr, S. A. Collins, T. V. Johnson, A. F. Cook, II, G. E. Danielson, and D. Morrison. The Galilean satellites and Jupiter - Voyager 2 imaging science results. *Science*, 206:927–950, November 1979.

[28] G. Tobie, A. Mocquet, and C. Sotin. Tidal dissipation within large icy satellites: Applications to Europa and Titan. *Icarus*, 177:534–549, October 2005.

[29] J. Wahr, Z. A. Selvans, M. E. Mullen, A. C. Barr, G. C. Collins, M. M. Selvans, and R. T. Pappalardo. Modeling stresses on satellites due to nonsynchronous rotation and orbital eccentricity using gravitational potential theory. *Icarus*, 200:188–206, March 2009.

[30] J. Wisdom. Tidal dissipation at arbitrary eccentricity and obliquity. *Icarus*, 193:637–640, February 2008.